

10th IWPF I - Lung Imaging Together in Hannover

Abstract Book



TABLE OF CONTENTS

Session Asthma: Abstract No. 001	...	1
Session COPD: Abstracts No. 100 – 103	...	4
Session Infection and Inflammation: Abstracts No. 200 – 203	...	11
Session Interstitial Lung Disease: Abstracts No. 300 – 302	...	20
Session Lung Cancer: Abstracts No. 400 – 402	...	25
Session Paediatric Lung Disease: Abstracts No. 500 – 501	...	31
Session Pre-Clinical DZL Session: Abstracts No. 600 - 602	...	37
Session Pulmonary Vascular Disease: Abstracts No. 700 – 701	...	41
Session Technical Advances in Functional Lung Imaging: Abstracts No. 800 – 814	...	45
Session Other: Abstracts No. 900 – 903	...	77

Session: Asthma

Abstract No. 001

Abstract No. 001

129Xe Magnetic Resonance Spectroscopy: Abnormal Cardiogenic Oscillations in Severe Asthma

Alexander M Matheson^{1,2,*}, Marrison J McIntosh^{1,2}, Harkiran K Kooner^{1,2}, Cory Yamashita¹, Narinder Paul¹, and Grace Parraga^{1,2}

¹Western University

²Robarts Research Institute

*Presenting author

Overview: In patients with severe asthma, ¹²⁹Xe MR spectroscopy revealed cardiogenic oscillations in the alveolar-to-red-blood cell tissue barrier which was a novel finding not observed in healthy volunteers.

Introduction: Whilst asthma is well-recognized as an airways disease, vascular pruning in patients,¹ also suggests that abnormal remodeling of the pulmonary vascular tree may be occurring over time. Recently, dynamic ¹²⁹Xe MR spectroscopy revealed “cardiogenic oscillations” in the RBC signal,² which was proposed to be related to pulmonary capillary blood flow. A preliminary investigation in patients with asthma was inconclusive;³ cardiogenic oscillations have not yet been examined. Here, we performed dynamic ¹²⁹Xe MR spectroscopy in people with asthma to measure potential gas-exchange abnormalities.

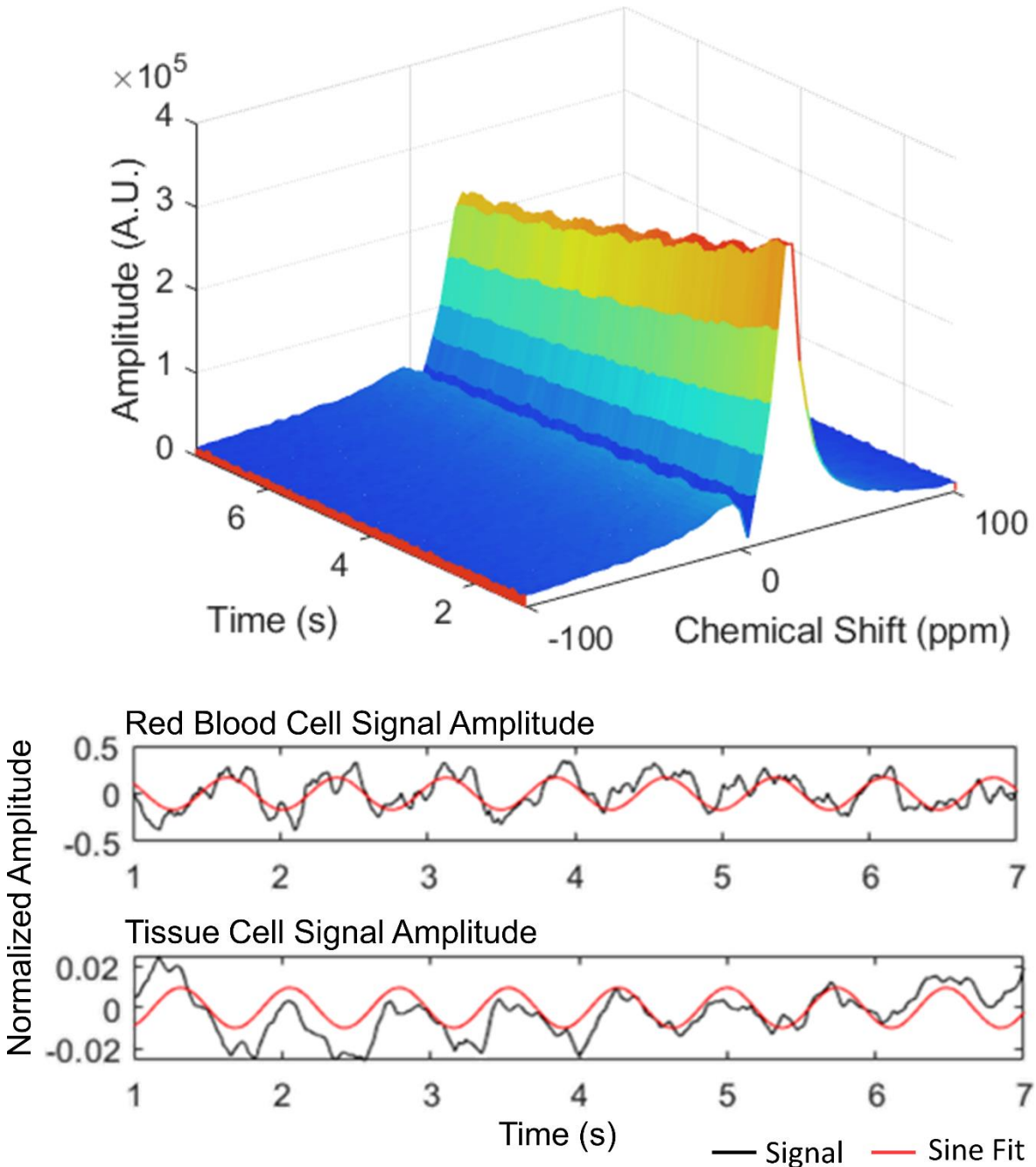
Methods: Healthy participants and those with severe asthma provided written, informed consent and underwent pulmonary function tests, thoracic CT and ¹²⁹Xe MR spectroscopy. Spectroscopy was performed on a 3.0T Discovery MR750 system (General Electric Healthcare, USA) with a spectroscopic acquisition (200-500 free-induction-decays, TR=15ms, TE=0.7ms, flip=40°, BW=31.25kHz, 600s 3-lobe Shinnar Le Roux pulse). Spectra were analyzed using a custom script (Matlab 2021a, Mathworks, USA) and fit according to a three-peak Lorentzian model. Dynamic Fourier induction decays were filtered using a spectral improvement by Fourier thresholding technique (SIFT) and a boxcar filter in the indirect time domain. Data from the first 1s of acquisition was discarded due to transport and RF effects; remaining spectra were de-trended according to a T₁ fit. Spectral parameters were fit to well-described sinusoidal models of cardiogenic oscillation.

Results: We evaluated 7 healthy participants (4 female, age=38±15) and 13 participants with severe asthma (11 female, age=60±16) 3 years after commencing continuous anti-IL5R therapy for severe eosinophilic asthma.⁴ The RBC:barrier ratio was significantly different (p=.03) between healthy (0.40±0.09) and asthma (0.30±0.08) participants. In three of 11 female participants with asthma, cardiogenic oscillations were observed in both the barrier and RBC compartments. RBC oscillation amplitude was 15±14%, normalized to the initial RBC amplitude whereas barrier oscillations were 1.5±0.5%. Oscillation frequency in both compartments matched pulse-oximeter measured heart rate. One participant had oscillations out-of-phase (phi=1.57) and two participants were in phase (phi=0.04, 0.15). In participants with barrier oscillations, VDP (1.8±0.2%) was significantly less than those without (4.0±2.6%, p=.03) and no other significant differences were observed. CT evidence of mild atelectasis was observed in all participants with barrier oscillations. CT vessel analysis measured blood volume in vessels with cross-sectional area <5mm² as 57±3%, with no difference between those with and without barrier oscillations.

Conclusions: RBC:barrier was significantly diminished in participants undergoing treatment for eosinophilic asthma compared to healthy volunteers alongside evidence of mild vascular pruning.¹ We also observed oscillations in barrier signal in three participants with asthma. Whether these tissue barrier oscillations are unique to asthma or simply more easily detected in these individuals requires further study.

Ash SY, Rahaghi FN, Come CE, et al. Pruning of the Pulmonary Vasculature in Asthma. *The Severe Asthma*

Research Program (SARP) Cohort. *Am J Respir Crit Care Med.* 2018;198(1):39-50.
 Bier EA, Robertson SH, Schrank GM, et al. A protocol for quantifying cardiogenic oscillations in dynamic (129) Xe gas exchange spectroscopy: The effects of idiopathic pulmonary fibrosis. *NMR Biomed.* 2019;32(1):e4029.
 Qing K, Mugler JP, 3rd, Altes TA, et al. Assessment of lung function in asthma and COPD using hyperpolarized 129Xe chemical shift saturation recovery spectroscopy and dissolved-phase MRI. *NMR Biomed.* 2014;27(12):1490-1501.
 McIntosh MJ, Kooner HK, Eddy RL, et al. Asthma control, Airway mucus and (129)Xe MRI ventilation after a single Benralizumab dose. *Chest.* 2022.



Session: COPD

Abstracts No. 100 - 103

Abstract No. 100

Towards improved disease prediction: modelling COPD as out-of-distribution from a normal population

Silvia Dias Almeida^{1, 2, *}, *Carsten Lueth*¹, *Tobias Norajitra*^{1, 2}, *Tassilo Wald*¹, *Taisiya Kopytova*¹, *Marco Nolden*^{1, 3}, *Paul F. Jaeger*¹, *Claus P. Heußel*^{4, 2}, *Jürgen Biederer*^{5, 6}, *Hans-Ulrich Kauczor*^{3, 2}, *Oliver Weinheimer*^{3, 2}, and *Klaus Maier-Hein*^{1, 3}

¹German Cancer Research Center (DKFZ)

²German Lung Research Center (DZL)

³University Hospital Heidelberg

⁴Thoraxklinik at University Hospital Heidelberg

⁵Translational Lung Research Center (TLRC), a member of the German Center for Lung Research

(DZL), Heidelberg, Germany

⁶University of Latvia

*Presenting author

Introduction:

Although having a high prevalence in the population, COPD remains largely underdiagnosed [1]. CT-derived features have taken part in disease diagnosis and prediction methods, providing insights into lung function. However, the same features proved to be highly heterogeneous, hindering the generalizability of the developed models. Previous work has shown these features deviate from normal-appearing lung regions, by training a contrastive pretext-task [2]. Following these findings, we hypothesize that a generative model can describe the distribution of healthy representations learned by the contrastive pretext-task and detect COPD as out-of-distribution from a healthy population.

Methods:

3D (50 mm³) non-overlapping patches were extracted from the lung parenchyma of inspiratory CT scans, from 496 and 424 consecutive participants of the COSYCONET cohort study (65 ± 9 y.o.) and of the COPDGene cohort (62 ± 9 y.o.), respectively. Healthy patients were defined by GOLD≤1 and COPD patients by GOLD>1. While there was no restriction for COPD patches, healthy patches used for training were limited to contain less than 1% emphysema, to assure purely non-diseased patches.

The developed pipeline consisted of: (1) learning a compact representation per patch with a contrastive pretext model (SimCLR [3]-VGG); (2) Training a set of generative models on the representations of a healthy population: a gaussian mixture model (GMM) with a variable number of components and an invertible-neural-network (INN) [4]; (4) Evaluating on all patches from a COPD-diseased and healthy set and aggregating the patch-scores per patient to predict COPD.

Results were compared to two baselines: (a) % of low attenuation areas under -950 HU (LAA-950%); (b) contrastive model combined with feature reconstruction [3]. Area under the receiver operating characteristic (AUROC) and area under the precision-recall curve (AUPRC) are reported individually as an evaluation metric per model on 123 and 106 subjects, per cohort.

Results:

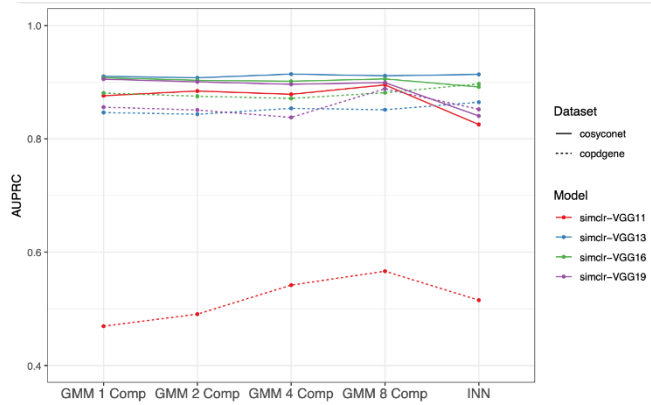
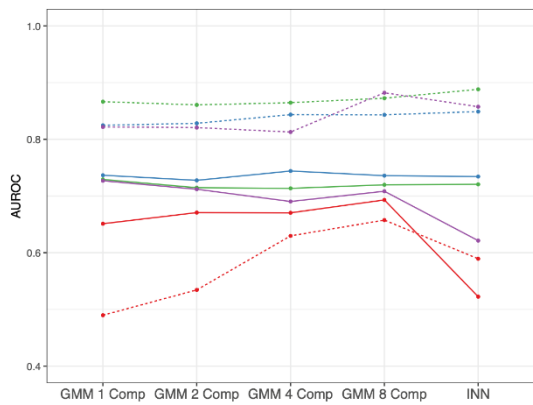
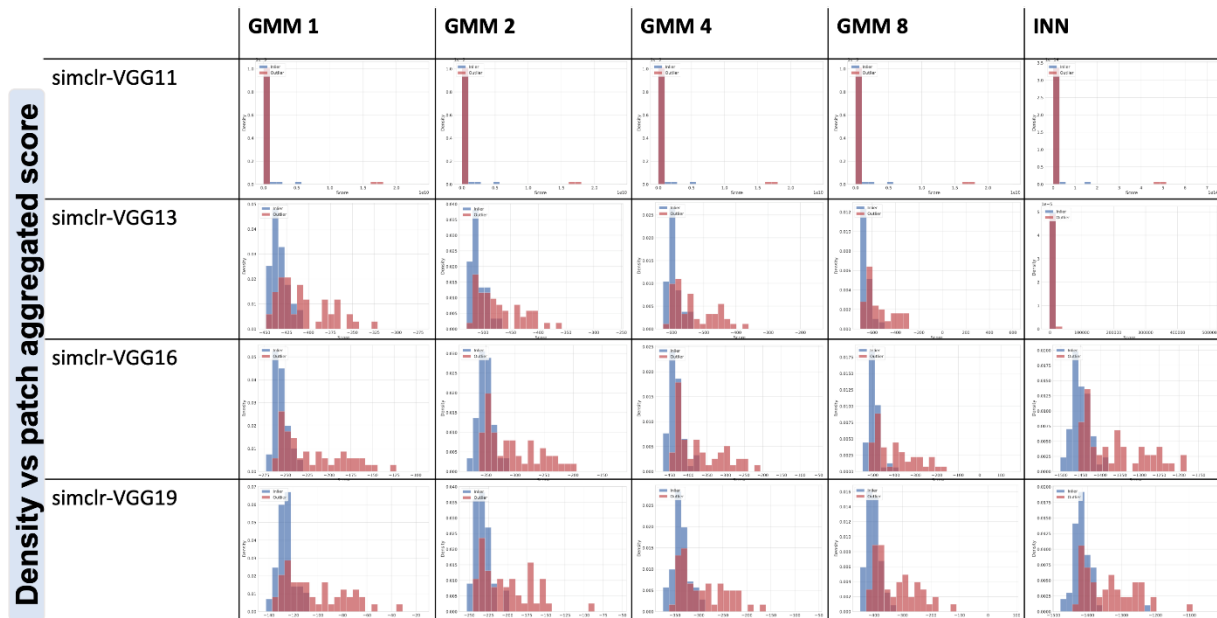
Baseline model (a) achieved AUROC/AUPRC of 0.70/0.60 and 0.81/0.78 while (b) achieved 0.67/0.63 and 0.87/0.73, for the COSYCONET and COPDGene cohorts, respectively. The developed pipeline results are depicted in figures 1 and 2. Figure 1 illustrates a separation between COPD and healthy aggregated patch-scores, for most models, concerning the COPDGene dataset. Figure 2 demonstrates that the best performance results are achieved for the COPDGene dataset, while the relevant information seems to be best encoded using a VGG-13/16/19. The number of components for the GMM does not seem to influence highperformance

settings (AUROC or AUPRC >0.8). Top performance for COSYCONET is achieved with VGG-13 and a 4 components GMM (AUROC: 0.74; AUPRC: 0.91), while VGG-16 and INN perform the best for COPDGene (AUROC: 0.89; AUPRC: 0.90).

Conclusion:

Adding the proposed generative model improves the overall performance of the COPD detection model, when compared to the baselines, by modeling the actual distribution of healthy and COPD data, captured by the pretext-task. Therefore, this approach shows to be relevant for COPD detection in a case-finding environment. Further investigation is warranted to investigate the influence of the patch level scores, their distribution and their relationship between intensity features, as well as to compare to more advanced parametric methods.

[1] Halpin DMG, et al. Global Initiative for the Diagnosis, Management, and Prevention of Chronic Obstructive Lung Disease. The 2020 GOLD Science Committee Report on COVID-19 and Chronic Obstructive Pulmonary Disease. Am J Respir Crit Care Med. 2021.
 [2] S. Dias Almeida, et al. Improved COPD detection on a chest CT-based contrastive learning approach, 10th DZL Annual Meeting, 6-7 July 2022, Abstract Book
 [3] Chen, T., Kornblith, S., Norouzi, M., & Hinton, G. , (2020), A simple framework for contrastive learning of visual representations, Proceedings of Machine Learning Research, International conference on machine learning
 [4] Ardizzone, L., Kruse, J., Rother, C., Köthe, U.: Analyzing inverse problems with invertible neural networks. In: Intl. Conf. on Learning Representations (2019)





Abstract No. 101

Opportunistic Lung Nodule Screening with MRI compared to Low-Dose CT in COPD: A Multicenter Trial

Qian Li^{1,*}, Lin Zhu¹, Mark Wielpütz², Oyunbileg von Stackelberg¹, Simon Triphan¹, Jürgen Biederer^{1,3}, Oliver Weinheimer¹, Monika Eichinger¹, Hans-Ulrich Kauczor^{4,5}, Claus Vogelmeier⁶, Rudolf Jörres⁷, and Bertram Jobst¹

¹Translational Lung Research Center (TLRC), a member of the German Center for Lung Research (DZL), Heidelberg, Germany

²Dept. of Diagnostic & Interventional Radiology, University Hospital Heidelberg; Translational Lung Research Center, a member of DZL, Heidelberg, Germany

³University of Latvia

⁴University Hospital Heidelberg

⁵German Center for Lung Research (DZL), Translational Lung Research Center (TLRC)

⁶Philipps-University of Marburg (UMR)

⁷University Hospital, Ludwig Maximilians University (LMU) Munich

*Presenting author

Purpose: To investigate the capability of morpho-functional chest MRI in a multicenter setting for the detection and management of incidental pulmonary nodules in patients with chronic obstructive pulmonary disease (COPD).

Materials and Methods: 567 patients (age 65.6±8.6y) underwent same-day contrast-enhanced MRI and non-enhanced low-dose computed tomography (LDCT) as part of a nationwide multicenter trial. Nodule dimensions, morphology and subsequent Lung CT Screening Reporting & Data System (Lung-RADS) category were assessed separately on MRI by two radiologists in a blinded fashion, and consensual LDCT results served as the standard of reference.

Results: A total of 525 nodules >3mm were detected on LDCT with a mean diameter of 7.2±6.1 (range 3.1-63.1mm). Sensitivity and positive predictive value of both readers using MRI were 63.0/84.8% and 60.2/83.9% for solid (n=495), 17.6/75.0% and 17.6/60.0% for part-solid (n=17), and 7.7/100% and 7.7/50.0% for ground-glass nodules (n=13), respectively. For nodules 6mm sensitivity/PPV were 78/92.8% and 75.7/93.2%, respectively. Readers underestimated the long-axis diameter on MRI by 0.5±1.7mm and 0.5±1.5mm compared to LDCT, respectively (p<0.001). For Lung-RADS categorization per nodule, MRI showed substantial to perfect inter-method agreement for MRI vs. LDCT (=0.70-1.00 and 0.69-1.00), as well as substantial to perfect inter-reader agreement for MRI (=0.75-1.00).

Conclusion: In a multicenter setting, morpho-functional MRI showed moderate sensitivity but excellent Lung-RADS categorization abilities for incidental pulmonary nodules in patients with COPD. Our data support the development of MRI into a screening tool for lung cancer.

Abstract No. 102

PREFUL-MRI evaluation of metronome-paced tachypnea induced dynamic hyperinflation in COPD patients

Robin Müller^{1, 2, *}, *Filip Klimeš*^{1, 2}, *Andreas Voskrebenev*^{1, 2}, *Lea Behrendt*^{1, 2}, *Till Kaireit*^{1, 2}, *Cristian Crisosto*^{1, 2}, *Maximilian Zubke*^{1, 2}, *Martin Prince*^{3, 4}, *Christopher Coopers*⁵, *Graham Barr*⁶, *Jens Hohlfeld*^{1, 7}, and *Jens Vogel-Claussen*^{1, 2}

¹Hannover Medical School, Hannover

²German Center for Lung Research (DZL)

³Weill Cornell Medical College, New York, NY

⁴Columbia College of Physicians and Surgeons, New York, NY

⁵David Geffen School of Medicine, UCLA, Los Angeles, California

⁶New York-Presbyterian/Columbia University Irving Medical Center, New York, NY, USA

⁷Fraunhofer Institute of Toxicology and Experimental Medicine, Hannover, Germany

*Presenting author

Introduction:

Hyperinflation in chronic obstructive pulmonary disease (COPD) patients worsens on exertion/exercise when their breathing frequency increases¹. Metronome-paced tachypnea (MPT) can be performed with 40 breaths per minute during MRI and has shown to induce dynamic hyperinflation in COPD patients². Conventionally, phase-resolved functional lung (PREFUL) MRI is used in order to assess regional ventilation dynamics during normal tidal breathing (NTB)³. Hereby, areas of lung parenchyma not adequately ventilated can be detected. This study aims to assess potential effects of MPT on pulmonary ventilation with PREFUL-MRI in comparison to NTB in COPD patients.

Methods:

Nineteen patients (12 males, 7 females; age range 40-77 years) with COPD and hyperinflation have been examined in an ongoing single center study. A 90-second-long time series of one coronal slice centered to the trachea was acquired for PREFUL-MRI at 1.5T under the following breathing maneuver:

60 seconds of NTB

30 seconds of MPT at 40 breaths / minute

As regional lung ventilation reaches a stable state in the second half of the MPT maneuver, the MPT part was divided into two sets of 15 seconds. Afterwards, regional ventilation derived ventilation defect percentages (VDPRVent) and flow volume loop cross correlation derived VDP (VDPFVL-CC)⁴ were calculated separately for NTP, MPT1 and MPT2. Body plethysmography was carried out at the same day.

A paired t-test with Bonferroni correction for multiple comparisons was used ($\alpha=0.025$).

Results:

The nineteen COPD patients showed a mean forced expiratory volume in 1 second of 45.9 \pm 14.1% of predicted normal, a forced vital capacity of 87.0 \pm 13.9% of predicted normal and a residual volume of 4.08 \pm 1.14 L.

VDPRVent increases from 38% (NTB) to 44% (MPT1) with $p=0.084$ and significantly from 38% (NTB) to 46% (MPT2) with $p=0.004$. The VDPFVL-CC increases significantly from 43% to 65% (MPT1) and 80% (MPT2) with $p=0.004$ and $p<0.001$, respectively (see Figure 1). Figure 2 shows an example of VDPRVent and VDPFVL-CC maps of a COPD patient during NTB and the 2nd half of MPT.

Discussion:

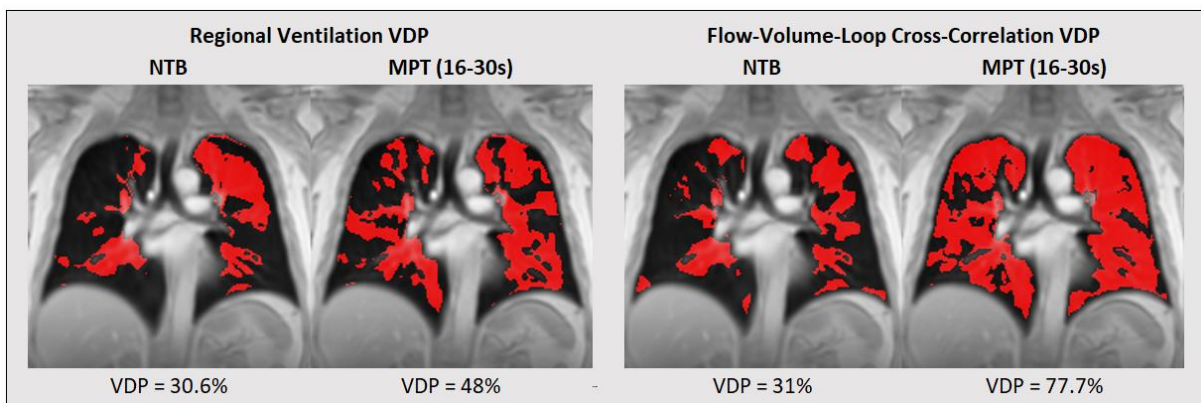
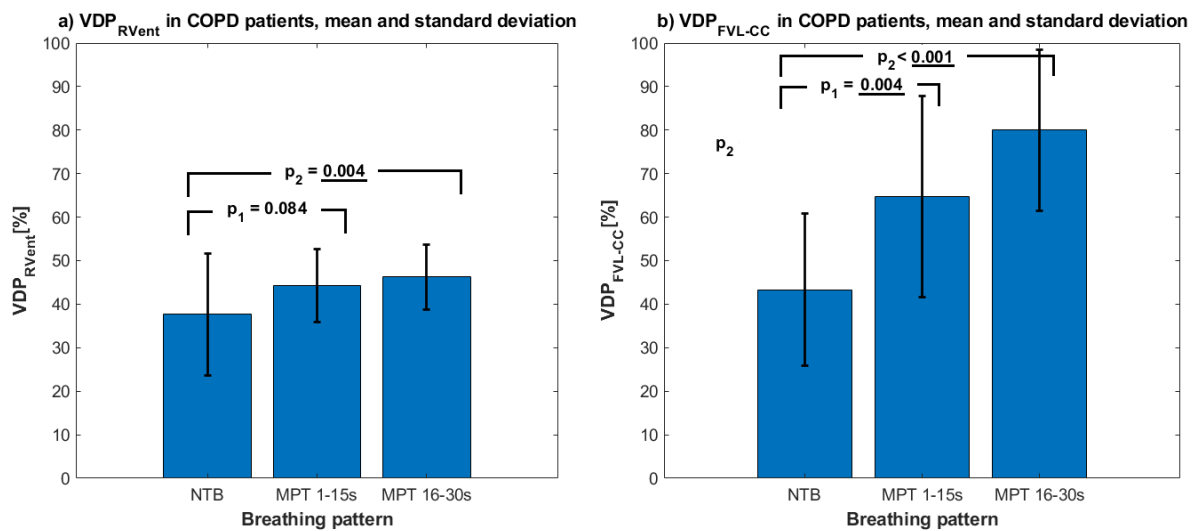
MPT induced dynamic hyperinflation can be assessed with PREFUL-MRI as demonstrated by significantly increased ventilation defect percentages. Hereby VDPFVL-CC has shown to be more sensitive compared to the "static" ventilation parameter VDPRVent as information of the complete breathing cycle is included. The decreased regional lung ventilation can be explained with temporarily increased hyperinflation as a consequence of a higher breathing

frequency in COPD patients. The studied method exhibits some limitations. Some patients did not perform the MPT correctly, probably due to difficulties hearing the metronome sound covered with loud scanning noise. Thus, verification of the breathing frequency is necessary. High variations of inspiratory volume and breathing position between NTB and MPT may have an impact on regional ventilation calculations. Moreover, the severity of the COPD affects the role of dynamic hyperinflation during MPT2. Further investigation in larger patient cohorts and comparison with healthy subjects is needed to show the robustness and clinical potential of PREFUL-MRI in combination with MPT.

O'donnell DE, Reville SM, Webb KA. Dynamic hyperinflation and exercise intolerance in chronic obstructive pulmonary disease. American journal of respiratory and critical care medicine. 2001 Sep 1;164(5):770-7
Weigt SS, Abrazado M, Kleerup EC, Tashkin DP, Cooper CB. Time course and degree of hyperinflation with metronome-paced tachypnea in COPD patients. COPD: Journal of Chronic Obstructive Pulmonary Disease. 2008 Jan 1;5(5):298-304

Voskresbenzev A et al. Feasibility of quantitative regional ventilation and perfusion mapping with phaseresolved functional lung (PREFUL) MRI in healthy volunteers and COPD, CTEPH, and CF patients. Magnetic resonance in medicine. 2018 Apr;79(4):2306-14

Kaireit TF, et al. Flow volume loop and regional ventilation assessment using phaseresolved functional lung (PREFUL) MRI: Comparison with 129xenon ventilation MRI and lung function testing. Journal of Magnetic Resonance Imaging. 2021 Apr;53(4):1092-105



Abstract No. 103

**+ ORAL
PRESENTATION**

The impact of hypoxia on the obese lung

Sophia Pankoke^{1,}, Christiane Pfarrer², Christian Mühlfeld¹, and Julia Schipke¹*

¹Hannover Medical School

²University of Veterinary Medicine Hannover

*Presenting author

Obesity is correlated with a higher risk for lung diseases; however, the underlying pathophysiological mechanisms are still unknown.

Here, C57BL/6N mice were fed either control diet (CD, 10% fat) or high fat diet (HFD, 60% fat). After 27 weeks, half of each diet-group was treated with hypoxia (-Hyp, 13% O₂) for 3 weeks. After 30 weeks, lung mechanics, ultrastructure and proteome were assessed.

In comparison to CD, HFD resulted in lower arterial pCO₂, thicker septal endothelium and interstitium, and an upregulation of proteins associated with lipid metabolism. Regardless of diet, hypoxia led to increased levels of hemoglobin and hematocrit, lower arterial pCO₂, and higher lung volumes. Compared to CD, CD-Hyp led to decreased elastance H and increased static lung compliance. Additionally, proteins regulating vascular cell surface interactions and extracellular matrix (ECM) organization were downregulated and the alveolar endothelium was thickened. Along with the changes in lung mechanics under CDHyp, hypoxia under HFD also caused lower hysteresis, pointing to surfactant alterations. While the interstitial thickness was decreased under HFD-Hyp, the fat-related thickening of the endothelium was not exacerbated. Also, proteomics implicated downregulation of platelet degranulation and adaptive immune system pathways.

Thus, both chronic hypoxia and high fat intake alone resulted in thicker alveolar endothelium and lower arterial pCO₂, indicating higher ventilation rates to achieve adequate oxygen saturation. Besides red blood cell adaptations and higher lung volumes, hypoxia altered the pulmonary elastic recoil. Analyses of the lung proteome suggested dietary variations in hypoxia adaptation, particularly cell-surface interactions/ECM organization under CD and platelet degranulation/adaptive immune system under HFD.

Session:
Infection and Inflammation
Abstracts No. 200 – 203

Abstract No. 200

Infrared Thoracoscope with Indocyanine Green Imaging in Surgery for Nontuberculosis Mycobacterium

Jun Atsumi^{1,}, Yuji Shiraishi¹, Miyako Hiramatsu¹, Kiyomi Shimoda¹, Toru Kawakami¹, and Takashi Arai¹*

¹Japan Anti-tuberculosis Association Fukujuji Hospital

*Presenting author

Introduction: The cavitary nodular bronchiectasis (C-NB) type is a refractory phenotype of pulmonary non tuberculosis mycobacterium (PNTM), consisting of multifocal lung destructive lesions such as bronchiectasis and cavity in multiple lobes.¹ For C-NB type PNTM, in addition to multidrug chemotherapy, complex anatomical lung resection in multiple lobes is frequently required to complete the removal of the destroyed lung, preserving non-affected functional lung.

However, complex anatomical lung resection such as combined complex segmentectomy is technically challenging because of the difficulties in determining the resection line. Therefore, imaging technology is necessary to identify the border between the destroyed lung and the functional lung. Here we present a novel intraoperative functional imaging technique using infrared thoracoscope with indocyanine green (IRT-ICG)^{2,3} for PNTM surgery.

Method:

1. Preoperative Lung perfusion scintigraphy

All patients underwent a preoperative work-up with high-resolution computed tomography (HRCT). On HRCT imaging, we identified destroyed lungs such as cavity and bronchiectasis of PNTM. Lung perfusion scintigraphy was performed after intravenous injection of 185 MBq of ^{99m}Tc-macro aggregated albumin. The imaging of lung perfusion scintigraphy was integrated with HRCT imaging by syngo MI applications (Siemens Medical Solutions, Germany). According to the imaging, we planned the surgery to remove the destroyed lung with perfusion defect, preserving the lung with perfusion.

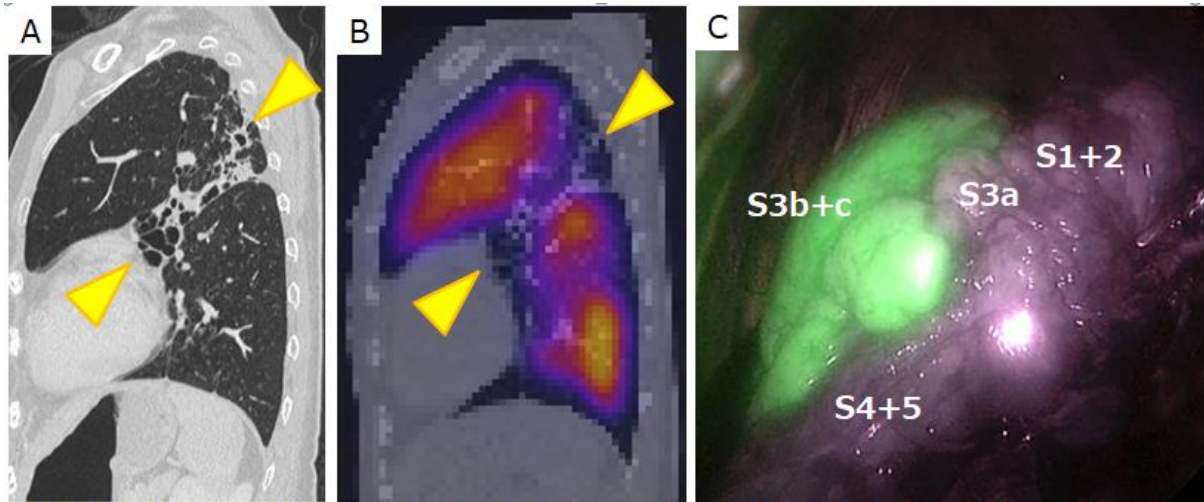
2. Intraoperative Lung blood flow assessment: IRT-ICG

Infrared thoracoscope (IRT) (Olympus, Japan) is a system that uses indocyanine green (ICG) (Daiichi Sankyo, Japan) to identify blood flow. ICG is injected into the blood via a peripheral vein intraoperatively. The perfused ICG allowed the normal functional lung to become fluorescent green on IRT monitor. On the other hand, the target destroyed lung, which was already isolated from the pulmonary vasculature, exhibited no fluorescence on IRT monitor. The border was then identified as the line separating the fluorescent and nonfluorescent lung parenchyma.

Patients and Outcome: Of the 29 patients with PNTM who underwent pulmonary segmentectomy between April 2021 and June 2022 at our hospital, we retrospectively collected data of 14 patients whose phenotype was C-NB. After excluding one patient who had not undergone lung perfusion scintigraphy, 13 patients were included in this study. Most of the patients were female (N=12) and the mean age was 61 (range 37-74). IRT-ICG well visualized the border between the destroyed lungs and non-affected lungs in all patients. As a result, all the patients but one completed surgery as planned. Combined segmentectomy in 12 and simple segmentectomy in one patient were performed. Postoperative complications with a Clavien–Dindo grade of 3 or more developed in 2 patients (15%) without mortality. All the patients achieved culture conversion, and no patients complained decline in activity in daily life during postoperative follow-up (57-418 days).

Conclusion: IRT-ICG imaging provided well visualization of the border between functional and destroyed lung in the surgery of C-NB type PNTM. This technique allows us to remove destroyed lungs completely while minimizing the sacrifice of the functional lung, resulting in a high conversion rate without a decline in patients' daily activity.

1.Koh WJ et al. *Eur Respir J.* 2017 2.Tarumi S et al. *Eur J Cardiothorac Surg.* 2014 3.Yotsukura M et al. *JTCVS Tech.* 2021



Computed tomography revealed severe bronchiectasis together with small cavities (arrowheads) in the left upper lobe (LUL) and bronchiectasis (not shown in the figure) in the left lower lobe (LLL) (A). Lung perfusion scintigraphy depicted defects in destroyed lung segments; S1+2, S3a, S4+5 (arrowheads), and S6+10 (not shown in the figure) (B). Intraoperative infrared thoracoscope imaging after intravenous indocyanine green injection revealed a definite borderline between perfused lung (green colored, S3b+c) and destroyed lung (nonfluorescent, S1+2+3a+S4+5) (C). Accordingly, the patients underwent complex segmentectomy of the destroyed lung (S1+2+3a+S4+5 in LUL following S6+10 in LLL).

Abstract No. 201

Longitudinal lung function assessment of patients hospitalised with COVID-19 using ^1H and ^{129}Xe MRI

Laura Saunders¹, Guilhem Collier^{1,*}, Ho-Fung Chan¹, Paul Hughes¹, Laurie Smith¹, James Watson², James Meiring², Zoe Gabriel², Thomas Newman², Megan Plowright², Philip Wade², James Eaden¹, Jody Bray¹, Helen Marshall¹, David Capener¹, Leanne Armstrong¹, Jennifer Rodgers¹, Martin Brook¹, Alberto Biancardi¹, Madhwesha Rao¹, Graham Norquay¹, Oliver Rodgers¹, Ryan Munro¹, James Ball¹, Neil Stewart¹, Allan Lawrie¹, Gisli Jenkins³, James Grist⁴, Fergus Gleeson⁴, Rolf Schulte⁵, Kevin Johnson⁶, Frederick Wilson⁷, Anthony Cahn⁷, Andrew Swift¹, Smitha Rajaram², Gary Mills¹, Lisa Watson², Paul Collini¹, Rod Lawson², Roger Thompson¹, and Jim Wild¹

¹University of Sheffield

²NHS Foundation Trust

³Imperial College London

⁴Oxford NHS Foundation Trust

⁵GE Healthcare

⁶University of Madison

⁷GlaxoSmithKline

*Presenting author

Introduction: Microvascular abnormalities and impaired gas transfer have been observed in patients with COVID-19. The longitudinal progression of pulmonary pathophysiological changes in these patients remains unclear.

Multinuclear (^1H & ^{129}Xe) MRI allows regionally sensitive measurement of pulmonary gas exchange, perfusion, ventilation and microstructure. The aim of this work is to use multinuclear MRI to assess pulmonary pathophysiological changes in patients who had been hospitalised with COVID-19 pneumonia, during the post-acute period.

Methods: Patients with no previously diagnosed respiratory disease who were hospitalised due to COVID-19 infection were recruited. MRI examinations (1.5T, GE scanner) were acquired at ~6, 12, 24 and 52 weeks after hospital admission. Patients that showed signs of interstitial lung damage on structural imaging at 12-weeks follow-up were retrospectively excluded.

^1H ultra-short echo time images were acquired with a 3D radial sequence during freebreathing with prospective respiratory bellows gating on expiration[1].

Dynamic contrast enhanced (DCE) lung perfusion MRI was acquired using time-resolved SPGR imaging. Parametric maps of pulmonary blood volume, pulmonary blood flow and mean transit time were calculated using indicator dilution theory[2].

^{129}Xe ventilation imaging using a 3D SSFP sequence was acquired after inhalation of 500ml ^{129}Xe + 500ml N_2 . Lung ventilation distribution was categorised using a generalised linear binning method, to define ventilation defect and normal ventilation percentages.

^{129}Xe DW-MRI was acquired after inhalation of 550ml ^{129}Xe + 450ml N_2 using a 3D SPGR multiple b-value sequence[3]. Maps of ^{129}Xe ADC and mean acinar airway dimension (LmD) were calculated.

3D spectroscopic imaging of the gas and dissolved phase ^{129}Xe resonance peaks (^{129}Xe dissolved in lung tissue membrane M and in red blood cells RBC)[4] was acquired using 1L of ^{129}Xe . Maps of gas transfer ratios (RBC:M, RBC:gas, M:gas) were calculated.

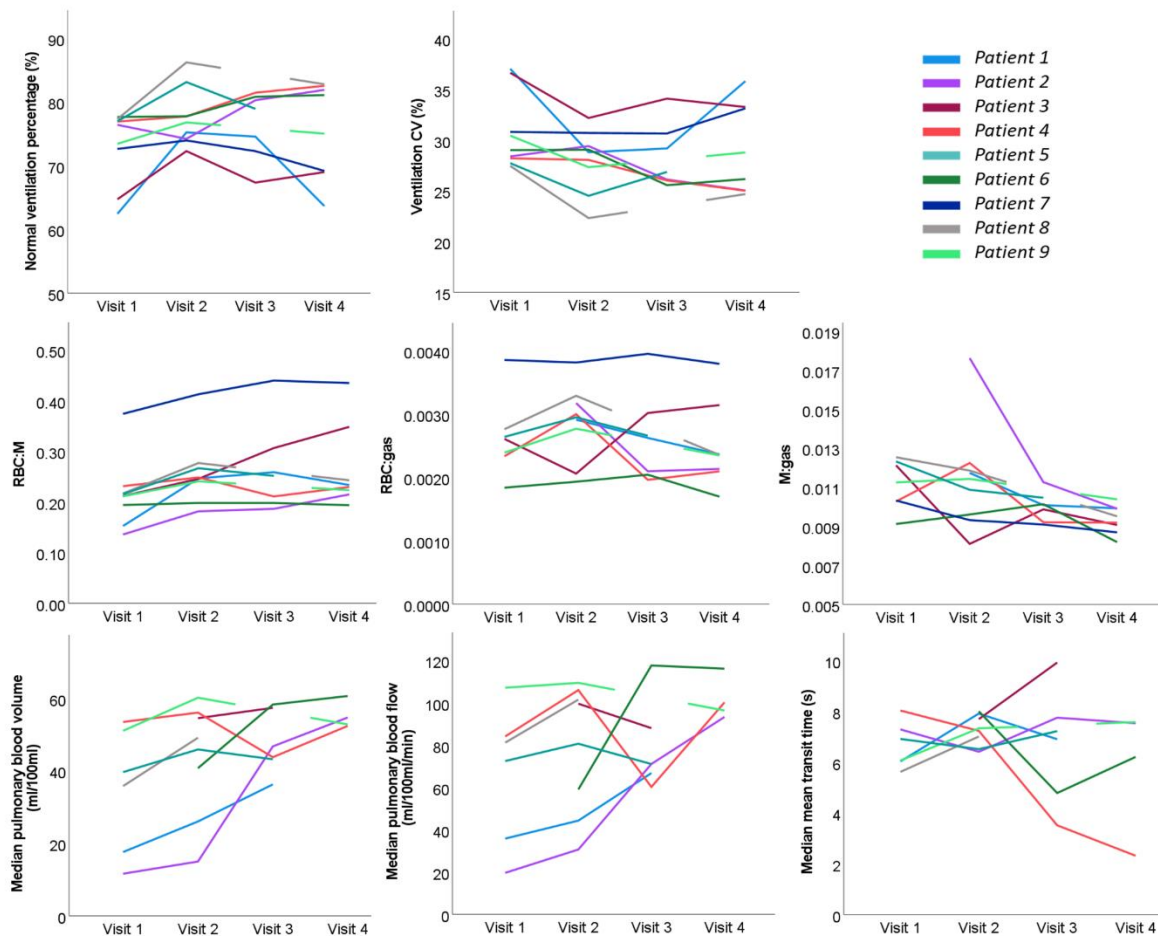
Global MRI metrics from the different visits were compared using a Skillings-Mack test with pairwise Wilcoxon tests and a correction for multiple testing was applied.

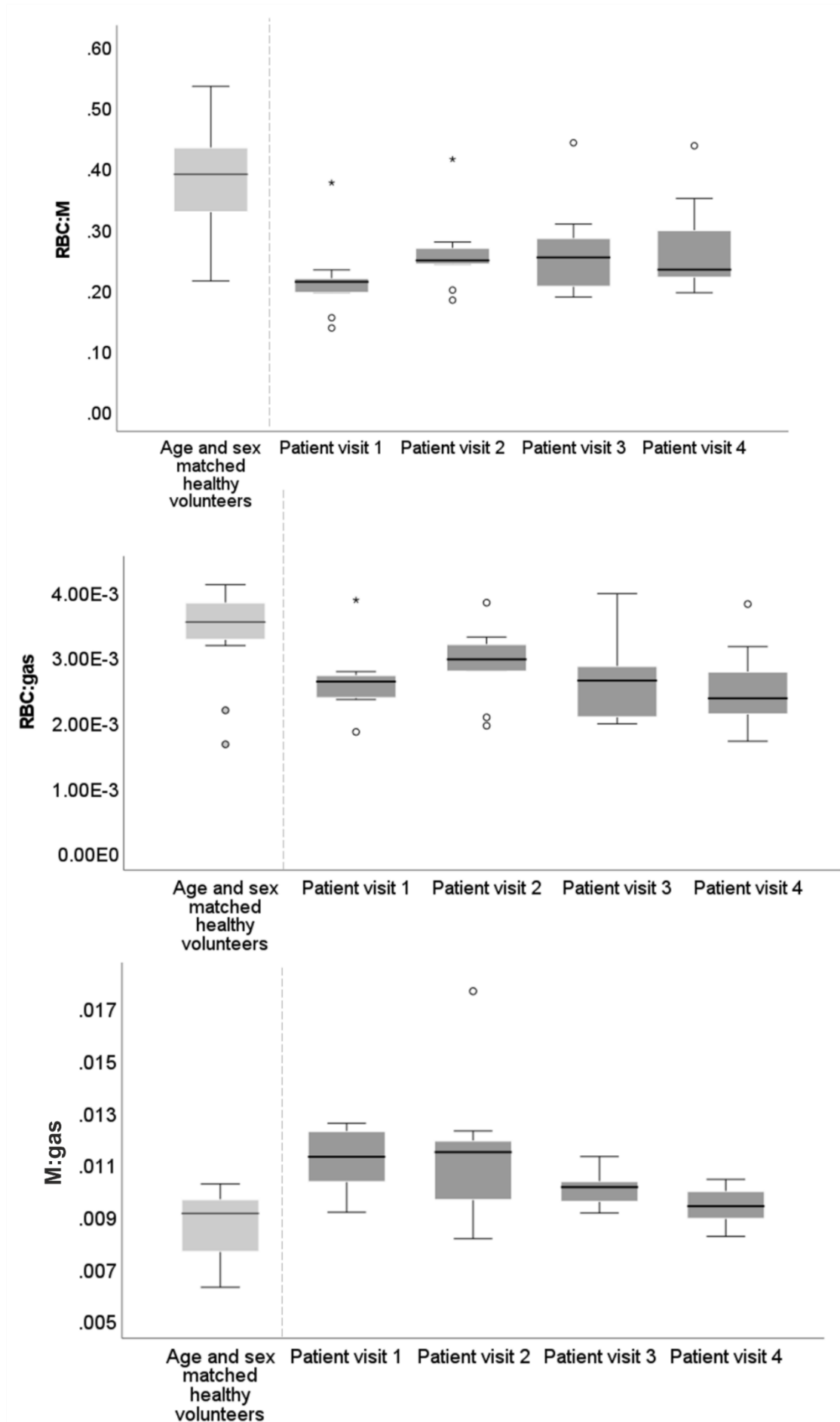
Results: 9 patients underwent MRI at 6, 12, 25 (n=7) and 51 (n=8) weeks after hospital admission. At 6 weeks post admission, patients demonstrated abnormal ^{129}Xe gas transfer

(RBC:M) but normal lung microstructure (ADC, LmD). Minor ventilation abnormalities present in four patients at 6 weeks post admission were largely resolved at 25 weeks. At 12-weeks, all patients with lung perfusion data available (n=6) showed an increase in both pulmonary blood volume and flow when compared to 6 weeks (Fig.1). Moreover, significant improvements in ^{129}Xe gas transfer were observed at 12 weeks compared to 6-weeks. However, ^{129}Xe gas transfer remained abnormal at weeks 12, 25 and 51 (Fig.2). Changes in ^{129}Xe gas transfer correlated significantly with changes in pulmonary blood volume ($r=0.49$, $p=0.029$) and TLCO Z-score ($r=0.64$, $p<0.001$).

Conclusions: This study demonstrates that multinuclear MRI is sensitive to pulmonary functional changes in the follow up of patients who were hospitalised with COVID-19. Impaired xenon gas transfer was observed up to one year after hospitalisation and may indicate damage to the pulmonary microcirculation. Longitudinal changes in xenon gas transfer are associated with changes in pulmonary blood volume.

1. Johnson, K.M., et al., *Optimized 3D ultrashort echo time pulmonary MRI*. *Magn Reson Med*, 2013. 70(5): p. 1241-50.
2. Sourbron, S.P. and D.L. Buckley, *Classic models for dynamic contrast-enhanced MRI*. *NMR Biomed*, 2013. 26(8): p. 1004-27.
3. Chan, H.F., et al., *3D diffusion-weighted (^{129}Xe) MRI for whole lung morphometry*. *Magn Reson Med*, 2018. 79(6): p. 2986-2995.
4. Collier, G.J., et al., *Dissolved (^{129}Xe) lung MRI with four-echo 3D radial spectroscopic imaging: Quantification of regional gas transfer in idiopathic pulmonary fibrosis*. *Magn Reson Med*, 2021. 85(5): p. 2622-2633.





Abstract No. 202

COVID-19 pneumonia and its lookalikes: How well do radiologists differentiate atypical pneumonias?

Athanasios Giannakis^{1,2}, Dorottya More^{1,2}, Stella Erdmann³, Laurent Kintzele¹, Ralph Fischer^{4,2}, Monika Vogel^{4,2}, David Lukas Mangold¹, Oyunaa von Stackelberg^{1,2}, Paul Schnitzler³, Stefan Zimmermann¹, Claus Peter Heußel^{4,2}, Hans-Ulrich Kauczor^{1,2}, and Katharina Hellbach^{1,2,*}

¹University Hospital Heidelberg

²German Center for Lung Research (DZL), Translational Lung Research Center (TLRC)

³Heidelberg University

⁴Thoraxklinik at University Hospital Heidelberg

*Presenting author

Objectives: Compared to the highly specific RT-PCR, the specificity of chest CT in diagnosing COVID-19 is lower, with a reported overall specificity of 46 - 80% (95% CI: 29–63%) [1, 2]. This can be explained by the fact, that typical signs of COVID-19 pneumonia partially overlap with that of other acute and chronic pulmonary conditions. The aim of this study was to investigate the diagnostic performance of radiologists with different level of experience in differentiating COVID-19 pneumonia from other atypical bacterial, fungal and viral pneumonias. Furthermore, this study contains a detailed analysis of infiltrate patterns of all pneumonias included, aiming at identifying those atypical pneumonias most similar to COVID-19 pneumonia and defining imaging markers that might help distinguish COVID-19 pneumonia from its top differential diagnoses.

Methods: Patients with positive RT-PCR tests for COVID-19 pneumonia (n=90) and non-COVID-19 atypical pneumonia (n=294) were retrospectively included. Five radiologists with different levels of experience in thoracic imaging, blinded to the pathogen tests results, assessed the CT scans and classified them as COVID-19 or non-COVID-19. For both groups, a pattern analysis based on the CT features was performed. A multivariate logistic regression model was used to calculate the ability of these CT features to predict COVID-19 pneumonia.

Results: The radiologists differentiated between COVID-19 and non-COVID-19 pneumonia with an overall accuracy, sensitivity, and specificity of 88% ± 4 (SD), 79% ± 6 (SD), and 90% ± 6 (SD), respectively. The variables associated with increased risk of COVID-19 pneumonia were peripheral distribution (odds ratio [OR] 2.13, p=0.116), rounded ground glass opacities (OR 1.96, p=0.099), band like subpleural opacities (OR 5.55, p<0.001), subpleural curvilinear lines (OR 2.52, p=0.021), and vascular enlargement (OR 2.63, p=0.071). Most important, pattern-based differential diagnoses of COVID-19 related infiltrates are atypical pneumonias caused by PJP, HSV1, CMV and Influenza A H1N1.

Conclusions: Radiologists can accurately differentiate between COVID-19 and non-COVID-19 atypical pneumonias on chest CT. Specific CT features help to make the correct diagnosis. The most important differential diagnoses for COVID-19 pneumonia were identified.

(1) Khatami F, et al. (2020) A meta-analysis of accuracy and sensitivity of chest CT and RT-PCR in COVID-19 diagnosis. *Sci Rep.* (2) Islam N, et al. (2021) Thoracic imaging tests for the diagnosis of COVID-19. *Cochrane Database of Systematic Reviews.*

Abstract No. 203



129Xe MRI VENTILATION IMPROVEMENTS 15 MONTHS POST-COVID INFECTION

Harkiran K Kooner^{1, 2, *}, Marrissa J McIntosh^{1, 2}, Alexander M Matheson^{1, 2}, Mohamed Abdelrazek¹, Inderdeep Dhaliwal¹, J Michael Nicholson¹, and Grace Parraga^{1, 2}

¹Western University

²Robarts Research Institute

*Presenting author

Overview: ¹²⁹Xe MRI ventilation defect percent (VDP), along with exercise capacity and quality-of-life, significantly improved in participants with post-acute COVID-19 syndrome 15-months post-infection, as compared to 3 months post-infection. There were no significant differences between hospitalized and non-hospitalized participants at 15-months. ¹²⁹Xe MRI VDP was significantly related to FEV₁, lung clearance index and post-exertional oxygen saturation measurements at follow-up.

Introduction: Post-acute COVID-19 syndrome (PACS) is an umbrella term encompassing persistent symptoms and poor quality-of-life four weeks after the onset of acute infection.¹ Most people with PACS report at least one symptom 12 months post-infection.^{2,3} Hyperpolarized ¹²⁹Xe magnetic resonance imaging (MRI) was previously used to quantify inhaled gas distribution abnormalities or ventilation defects in PACS,^{4,5} where ventilation defect percent (VDP) was related to exercise limitation and post-exertional oxygen saturation.⁵ Hence, our objective here was to evaluate PACS participants 15 months postinfection, which was a full year after the baseline investigation.⁵

Methods: Participants provided written informed consent to pulmonary function tests, six-minute walk test, quality-of-life questionnaires and ¹²⁹Xe MRI 12-months after a baseline visit. VDP was generated by normalizing ventilation defect volume to the ¹H MRI thoracic cavity volume.⁶ Differences between baseline and follow-up were evaluated using paired samples t-tests, with the post-hoc Holm-Bonferroni correction for multiple comparisons. Univariate relationships were evaluated using Pearson (r) and Spearman (ρ) correlations.

Results: We evaluated 41 participants (21 female, 20 male; mean age 56±14yr) who completed MRI 3-months and 15-months post-infection. Six-minute walk distance (6MWD) (p=.01), St. George's Respiratory Questionnaire (SGRQ) score (p<.001), International Physical Activity Questionnaire score (p=.04), and VDP (p<.001) significantly improved at follow-up. In addition, at follow-up, there were no significant differences in pulmonary function, exercise capacity, quality-of-life, or VDP between participants hospitalized (n=14) during acute infection and those not hospitalized (n=27). Improvements greater than the minimal clinically important difference were reported for 6MWD (26 m)⁷ by 53% (18/34) of participants, for SGRQ (4 points)⁸ by 68% (23/34) of participants, and for VDP (2%)⁹ by 41% (17/41) of participants. At follow-up, there were significant relationships for VDP with the forced expiratory volume in one second (FEV₁) (ρ=-.41, p=.008), lung clearance index (LCI) (ρ=.59, p<.001) and post-exertional SpO₂ (ρ=-.51, p=.001).

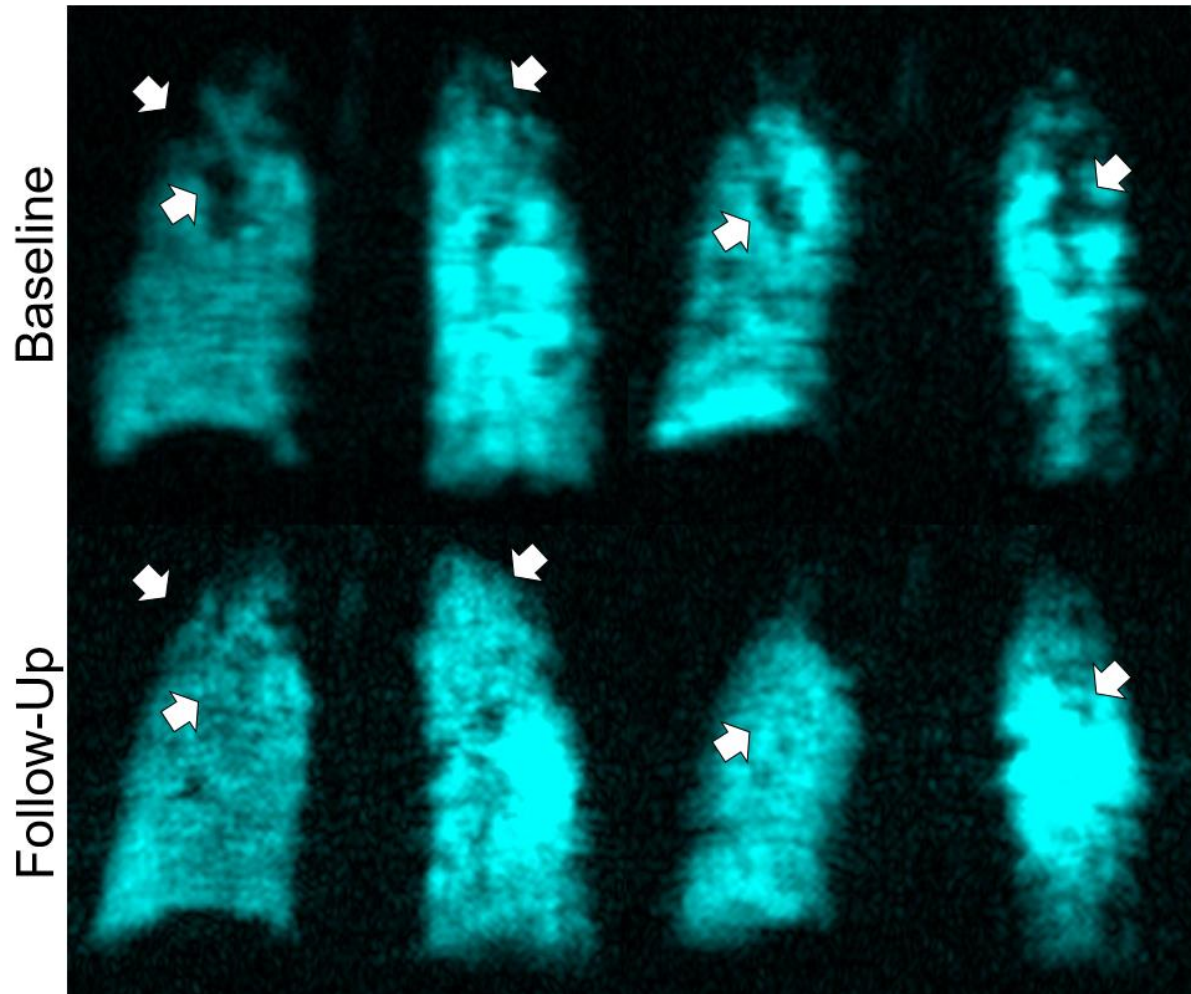
Figure 1 shows representative ¹²⁹Xe ventilation MRI (cyan) for a PACS participant who demonstrated an improvement in VDP between baseline and follow-up.

Conclusions: Participants with PACS demonstrated improved exercise capacity, quality-of-life and ¹²⁹Xe MRI ventilation, 15-months post-COVID-19 as compared to a baseline visit, 3-months post-infection. Participants with severe acute COVID-19 infection did not report more significant PACS symptoms 15-months post-infection. There were significant relationships for ventilation defects with FEV₁, LCI, and post-exertional oxygen saturation, providing mechanistic insights that link symptoms and exercise limitation with airways disease.

References:

1. Nalbandian et al. NatMed (2021).

2. Huang et al. Lancet (2021).
3. Lombardo et al. OpenForumInfectDis (2021).
4. Li et al. SciAdv (2021).
5. Kooner & McIntosh et al. BMJOpenRespirRes (2022).
6. Kirby et al. AcadRadiol (2012).
7. Puhan et al. ERJ (2011).
8. Jones COPD (2005).
9. Eddy et al. ERJ (2018).



Session:
Interstitial Lung Disease
Abstracts No. 300 – 302

Abstract No. 300

Automatic deep-learning-based lung analysis for interstitial lung disease

Ryo Aoki^{1,*}, Tae Iwasawa², Tomoki Saka³, Tsuneo Yamashiro¹, Daisuke Utsunomiya¹, Toshihiro Misumi¹, Tomohisa Baba², and Takashi Ogura²

¹Yokohama City University Graduate School of Medicine

²Kanagawa Cardiovascular and Respiratory Center

³Kanazawa Institute of Technology

*Presenting author

Purpose

We investigated the feasibility of a new deep-learning (DL) lung analysis method for the evaluation of interstitial lung disease (ILD) by comparing it with the Gaussian histogram normalized correlation system (GHNC) and visual evaluation by a thoracic radiologist.

Methods

We prospectively included 104 patients (84 with and 20 without ILD). First, an expert radiologist settled regions of interest in the typical areas of normal, ground-glass opacity, consolidation, fibrosis, honeycombing, reticulation, traction bronchiectasis, and emphysema and compared them with the GHNC and DL analysis results. Second, we measured the extent of ILD lesions by GHNC, and DL analysis and compared them. Finally, we compared the extent of computed tomography (CT) lesions measured by DL analysis with pulmonary function tests.

Results

Pearson's correlation analysis revealed a significant correlation between DL analysis and GHNC results. The agreement between DL analysis and radiologists on the volume ratio of normal lung and fibrotic lesions was also good to excellent. Forced vital capacity was significantly correlated with DL analysis ($r = 0.789$, $P < 0.001$ for normal lung volume and $r = -0.288$, $P = 0.004$ for fibrotic lesion volume).

Conclusion

A deep-learning-based algorithm provides automatic lung CT segmentation and quantification. The extent of lesion measured using DL analysis showed a negative correlation with pulmonary function.

Abstract No. 301

QCT and CFD Show SO₂-associated Lung Structure-Function Alteration in Healthy and IPF Subjects

Jiwoong Choi^{1,2,*}, In Kyu Lee^{1,2}, Mario Castro¹, Sunmi Choi³, Chang-Hoon Lee³, Kyoung-Nam Kim⁴, Kyung-Shin Lee³, Kum Ju Chae⁵, Ching-Long Lin⁶, Eric Hoffman⁶, Eun-Kee Park⁷ and Chang Hyun Lee³

¹University of Kansas School of Medicine

²University of Kansas

³Seoul National University Hospital

⁴Ajou University School of Medicine

⁵Jeonbuk National University Hospital

⁶University of Iowa

⁷Kosin University College of Medicine

*Presenting author

Introduction: We investigated how SO₂ is associated with changes in regional lung structure and function, using quantitative CT (QCT) image matching and one-dimensional (1D) CFD simulations of tidal breathing.

Methods: Inspiratory and expiratory chest CTs, residence (r) and work (w) address-based SO₂ exposure for the past 5 years (5y), and pulmonary function test (PFT) results were collected from 119 participants enrolled in 5 institutions in South Korea: healthy (age=68±10, M:F=15:51); IPF (age=72±7, M:F=43:10). Using VIDA Vision (Coralville, IA) and in-house QCT-CFD pipeline, 185 multiscale structural and functional features were derived, including 72 air flow features from tidal breathing simulations on the skeletonized entire conducting airway models. Pearson's correlation were used for analysis.

Results: Current (curr) residential address-based SO₂ exposure (SO_{2,r,curr}) associated with functional small airway disease percent (fSAD%) both in healthy subjects (r=0.58,p=0.010) and in IPF (r=0.41,p=0.049). SO_{2,w,curr} associated with relative regional air volume change (RRAVC), negatively in the left and right upper lobes (LUL,r=-0.71,p<0.001; RUL,r=-0.63,p=0.004) and positively in the right lower lobe (RLL,r=0.55,p=0.016) of healthy subjects, and negatively only in the left lower lobe (LLL) of IPF (r=-0.84,p=0.019). In healthy subjects, volume expansion ratio (J), anisotropic deformation index (ADI), and normalized local displacement (s*) were all negatively associated (r=-0.67,-0.53,-0.64;p=0.002,0.02,0.004) but no airway metrics significantly associated in healthy subjects. In IPF, however, Pi10 decreased (r=-0.42,p=0.040) and end-tracheal angle increased (r=0.53,p=0.007) as SO_{2,r,5y} increased. J, and s* were not associated, but ADI positively correlated with SO_{2,w,5y} (r=0.62,p=0.044) in IPF. CFD simulations showed that, in healthy subjects, SO_{2,r,curr} associated with flow rate fraction decrease in the LUL (r=-0.66,p=0.014) and increase in the RLL (r=0.67,p=0.012), shifting regional ventilation contribution. SO_{2,r,5y} exposure negatively associated with CFD-derived transpulmonary pressure (P_{tp}) (r=-0.64,p=0.018). From the PFT results, post-bronchodilator (post-BD) FEV1 associated with SO_{2,w,curr} (r=-0.52,p=0.027). In IPF, SO_{2,r,5y} associated with increased pressure drop through the entire conducting airway (P) (r=0.47,p=0.039), pressure workload in the RUL (P×flowrate,r=0.51,p=0.022).

Conclusions: QCT-CFD analysis showed how long-term and short-term residential and work address-based SO₂ associated with multiscale lung structure-function relationship, similarly and differently in healthy and IPF subjects. Highlighted features such as fSAD% may serve as imaging biomarkers for SO₂-associated lung structural and functional impairment.

Choi et al. *Am J Respir Crit Care Med* 2022;205:A2544.

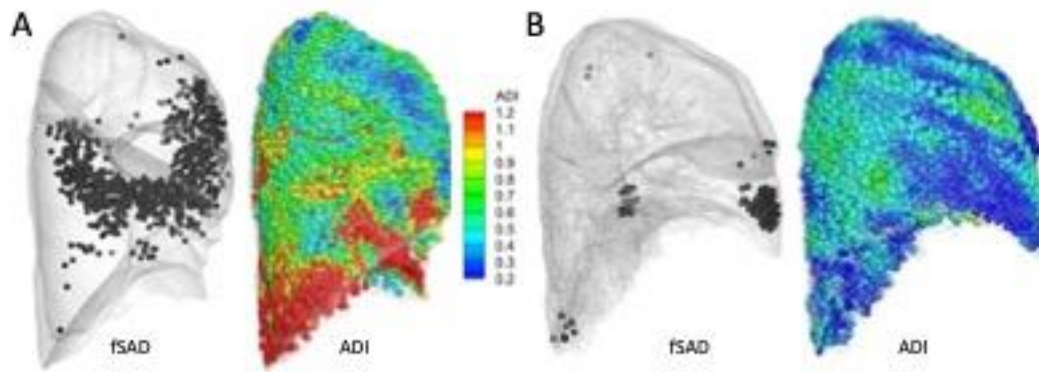


Figure. FSAD and ADI maps of representative IPF patients with (A) high and (B) low SO₂ exposure.

Abstract No. 302

Quantitative analysis of pleuroparenchymal fibroelastosis-like lesion

Tae Iwasawa^{1,*}, Naofumi Yasuda¹, Ryo Aoki², Tomohisa Baba¹, and Takashi Ogura¹

¹Kanagawa Cardiovascular & Respiratory Center

²Yokohama City University Graduate School of Medicine

*Presenting author

Purpose

The presence of pleuroparenchymal fibroelastosis (PPFE)-like lesion is reported to be associated with poor prognosis in patients with interstitial lung disease (ILD). We have developed a deep learning-based lung analysis system (QZIP-ILD, Ziosoft, Inc., Tokyo, Japan) and measured the PPFE-like lesion quantitatively. We evaluated the correlation between the PPFE-like lesion volume and survival of patients with ILD.

Participants and Methods

We evaluated consecutive 116 patients (86 men and 30 women) with idiopathic ILD who visited our center from January 2016 to March 2017. PPFE-like lesion was defined as subpleural consolidation associated with upper lung lobe fibrosis. Two expert chest radiologists evaluated the presence of a PPFE-like lesion.

We analyzed the initial computed tomography (CT) using the QZIP-ILD. The system automatically segmented the lung into eight patterns; normal, emphysema, ground-glass opacity, consolidation, reticulation, honeycomb, traction bronchiectasis, and fibrosis (F-pattern). F-pattern corresponds to consolidation with traction bronchiectasis. We measured each lesion volume and calculated the F-pattern extent in the upper lobe, which was the ratio of the lesion volume to the upper lung lobe volume.

The diagnostic performance of the F-pattern extent in the upper lobe was evaluated using the area under the receiver operating characteristic curve (AUC). We evaluated the whole lung F-pattern volume with the patients' survival using Cox regression analysis.

Results

Among 116 patients, 18 patients had a PPFE-like lesion. The AUC of the F-pattern extent in the upper lobe was 0.933 (95% CI 0.889–0.977).

The median follow-up time was 57.1 months, and 36 patients died, including 10 patients with PPFE-like lesions. Multivariate analysis showed that higher whole lung F-pattern volume (odds ratio 1.49, 95% CI 1.17–1.89, $p=0.01$), lower forced vital capacity (odds ratio 0.97, 95% CI 0.95–0.99, $p=0.03$), and age (odds ratio 1.05, 95% CI 1.01–1.10, $p=0.26$) were independent predictors of prognosis.

Conclusion

Higher PPFE-like lesion volume upon initial CT independently predicted worse survival in patients with ILD.

Session: Lung Cancer

Abstracts No. 400 – 402

Abstract No. 400

Comparing radiomics-based immunotherapy prediction models in advanced stage lung cancer patients

Jonas Bohn^{1, 2}, *Jonas Kroschke*^{3, 4}, *Marco Nolden*^{1, 3}, *Silvia Dias Almeida*^{1, 2}, *Petros Christopoulos*^{5, 2}, *Stephan Rheinheimer*^{3, 2}, *Alan Peters*^{3, 2}, *Thomas Muley*^{5, 5}, *Oyunbileg von Stackelberg*^{3, 2}, *Hans-Ulrich Kauczor*^{3, 2}, *Klaus Maier-Hein*^{1, 3}, *Claus Peter Heußel*^{5, 2}, and *Tobias Norajitra*^{1, 2}

¹German Cancer Research Center (DKFZ), Heidelberg, Germany

²Translational Lung Research Center (TLRC) a member of the German Center for Lung Research (DZL), Heidelberg, Germany

³University Hospital, Heidelberg, Germany

⁴Kantonsspital Thurgau, Institute for Radiology, Thurgau, Switzerland

⁵Thoraxklinik, Heidelberg, Germany

About 50% of lung cancer patients are not responding to assigned immunotherapy. This problem shows the need for a more precise non-invasive treatment prediction. Changes in the design of radiomics/machine learning pipelines and the integration of diverse additional data sources (clinical & radiological data) show differences in prediction performance of the treatment outcome. Radiomics aims to encode the tumors phenotype by standardized, reproducible and explainable features which can be invisible to the human eye. Machine learning models are at the backend of a radiomics pipeline classifying patients into nonresponders

or responders. This classification increases survival for advanced stage lung cancer patients in an early stage of therapy, reduces the number of non-necessary treatments and makes better treatment possibilities available for non-responders.

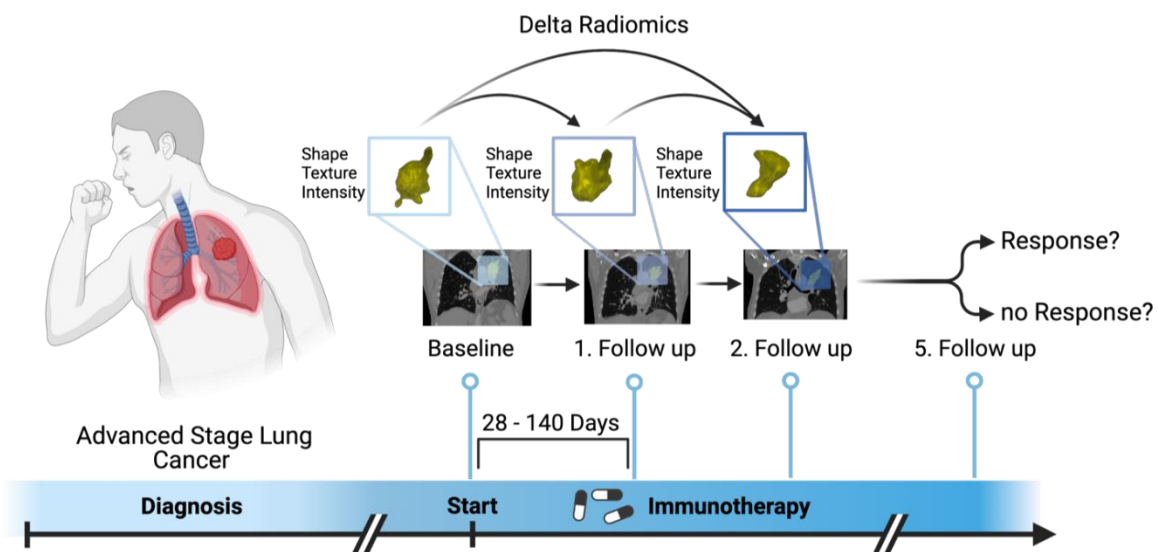
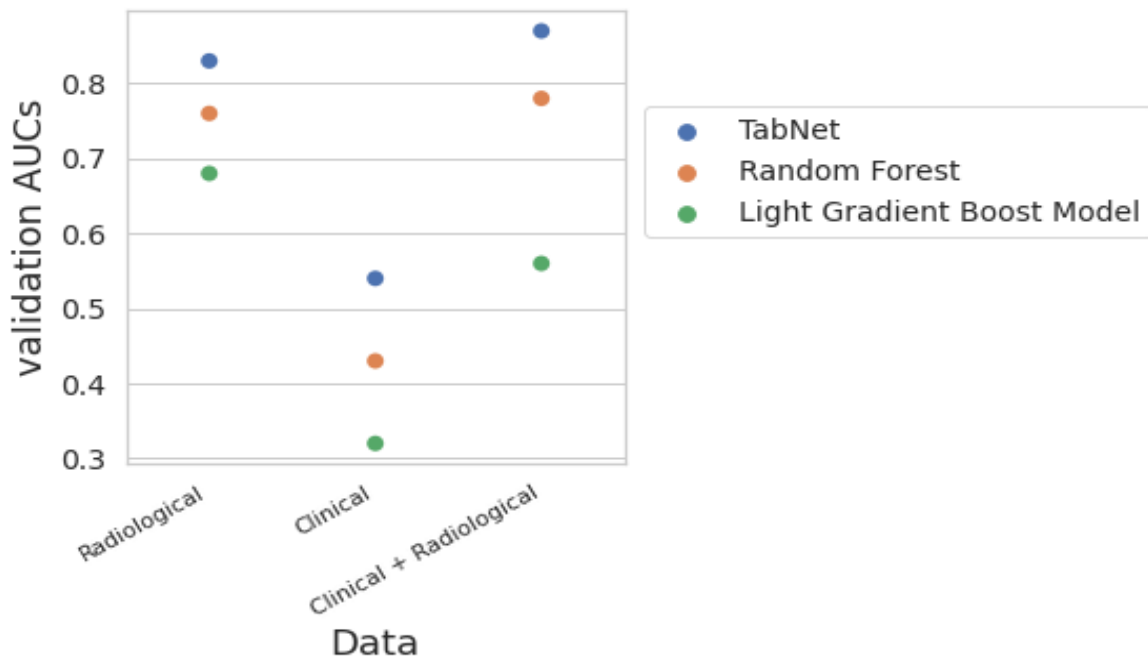
Published radiomics approaches are lacking on the comparison of machine learning models and evaluation of hyperparameter optimization as well as added data sources to increase and evaluate the performance of predictive models on tabulated data. This study compares performance of different pipeline designs with regard to inclusion of clinical and radiological data to the radiomics feature space and assessment of applied machine learning/deep learning methods. The presented approach analyzes 87 advanced-stage adenocarcinoma patients with 408 longitudinal Computer Tomography (CT) scans and 23 clinical/radiological parameters. The designed pipeline includes a state-of-the-art segmentation model (nnU-net) as well as a self-supervised body part regression model for automated image processing. Radiomics features have been extracted and selected from the intratumoral and the peritumoral (+ 3mm) region of the tumors. Delta radiomics features have been calculated during immunotherapy (see Figure 1). The evaluation of the best classifier has been performed on radiomics data, clinical data and a combination of clinical and radiomics data using group wise cross-validation. Compared models include a random forest classifier and a Light Gradient boost model (LGBM) optimized with an AutoML approach and a nonoptimized TabNet deep learning model.

On the radiomics data, the best model was a TabNet classifier with a validation Area Under the Receiver Operating Characteristics (AUROC) of 0.83 (+/- 0.11). Predictions of the treatment response only based on clinical and radiological features were in general hard to tackle due to unavailability or incompleteness of parameters. The best model on clinical and radiological data was a TabNet model with an AUROC of 0.54 (+/-0.11). On the combined dataset (radiomics and clinical/radiological parameters) the TabNet classifier reached the best validation AUROC of 0.87 (+/- 0.09). The random forest classifier and the LGBM classifier could not outperform the TabNet classifier on any of the used dataset (see Figure 2).

Overall, the TabNet deep learning model without hyperparameter optimization showed the best performance in the prediction of treatment responders in comparison to the optimized

random forest and the optimized LGBM classifier. In conclusion, applied models could not discriminate responders from non-responders only on clinical data but clinical data together with radiomics information increased the model performance. The model itself, its optimization as well as the quality of data are essential for accurate treatment response prediction.

Yang, F., et al., *CT-based radiomics signatures can predict the tumor response of non-small cell lung cancer patients treated with first-line chemotherapy and targeted therapy. Eur Radiol, 2022. 32(3): p. 1538-1547.*
 Isensee, F., et al., *nnU-Net: a self-configuring method for deep learning-based biomedical image segmentation. Nat Methods, 2021. 18(2): p. 203-211.*
 Schuëgger, S., *Body Part Regression for CT Images. arXiv, 2021*
 Shah, C., Q. Du, and Y. Xu, *Enhanced TabNet: Attentive Interpretable Tabular Learning for Hyperspectral Image Classification. Remote Sensing, 2022. 14(3).*



Abstract No. 401

**+ ORAL
PRESENTATION**

Association of Usual Interstitial Pneumonia and Survival in Stage IA Non-small Cell Lung Cancer

Won Gi Jeong^{1, 2, *}, Jong Eun Lee², and Yun-Hyeon Kim²

¹Chonnam National University Hwasun Hospital

²Chonnam National University Medical School

*Presenting author

Purpose

To assess the association of usual interstitial pneumonia (UIP) computed tomography (CT) pattern and survival in patients with resected stage IA non-small cell lung cancer (NSCLC).

Materials and Methods

Data of patients who underwent curative resection due to pathological stage IA NSCLC between 2010 and 2015 were retrospectively collected. CT features indicating interstitial pneumonia (IP) were classified according to the diagnostic criteria for idiopathic pulmonary fibrosis proposed by the Fleischner Society. The association of UIP CT pattern and causespecific mortality was assessed with Kaplan-Meier analysis with log-rank test. Cox proportional hazards regression was performed for assessing the risk factors of causespecific mortality.

Results

Overall, 228 patients were identified [63.27 ± 8.54 years, 133 men (58.3%)]. Typical or probable UIP CT pattern was present in 19 patients (19/228, 8.34%). Typical or probable UIP CT pattern was associated with higher cause-specific mortality compared to those without IP in Kaplan-Meier analysis with log-rank test ($p < 0.001$). Patients with typical or probable UIP CT pattern showed significantly higher cause-specific mortality compared to those without IP at 5 years after surgery (survival rate: 68.02% vs. 93.06%, $p < 0.001$). Multivariable Cox proportional hazards regression revealed that typical or probable UIP CT pattern was independently associated with higher cause-specific mortality (hazard ratio = 2.87; 95% confidence interval: 1.03, 7.99).

Conclusion

Typical or probable UIP CT pattern was associated with higher cause-specific mortality in patients with resected stage IA NSCLC. Patients with typical or probable UIP CT pattern should be provided with appropriate surveillance and management for better prognosis.

Raghu G, Remy-Jardin M, Richeldi L, Thomson CC, et al. Idiopathic pulmonary fibrosis (an update) and progressive pulmonary fibrosis in adults: an official ATS/ERS/JRS/ALAT clinical practice guideline. *Am J Respir Crit Care Med.* 2022;205(9):e18-e47.

Hatabu H, Hunninghake GM, Richeldi L, Brown KK, Wells AU, Remy-Jardin M, et al. Interstitial lung abnormalities detected incidentally on CT: a Position Paper from the Fleischner Society. *Lancet Respir Med.* 2020;8(7):726-737.

Luppi F, Kalluri M, Faverio P, Kreuter M, Ferrara G. Idiopathic pulmonary fibrosis beyond the lung: Understanding disease mechanisms to improve diagnosis and management. *Respir Res.* 2021;22(1):109.

Hida T, Hata A, Lu J, Valtchinov VI, Hino T, Nishino M, et al. Interstitial lung abnormalities in patients with stage I non-small cell lung cancer are associated with shorter overall survival: the Boston lung cancer study. *Cancer Imaging.* 2021;21(1):14.

Abstract No. 402

Ventilation and Perfusion Imaging at a 0.35 T MR-Linac - Feasibility and Reproducibility Study

Rabea Klaar^{1,2,}, Moritz Rabe³, Thomas Gaass^{1,2}, Moritz J. Schneider^{1,2}, Ilyes Benlala^{1,4}, Stefanie Corradini³, Chukwuka Eze³, Claus Belka^{3,5}, Guillaume Landry³, Christopher Kurz³, and Julien Dinkel^{1,2}*

¹Department of Radiology, University Hospital, LMU Munich, Munich, Germany

²Comprehensive Pneumology Center (CPC-M), Member of the German Center for Lung Research (DZL), Munich, Germany

³Department of Radiation Oncology, University Hospital, LMU Munich, Munich, Germany

⁴Univ. Bordeaux, INSERM, Centre de recherche Cardio-Thoracique de Bordeaux, U1045, F-33000 Bordeaux, France

⁵German Cancer Consortium (DKTK), Munich, Germany

*Presenting author

Introduction

Radiation therapy plays an important role in the treatment of lung cancer. The introduction of combined therapy and MR-imaging devices, so-called MR-Linacs, in the clinical routine opened up possibilities in terms of precise tumor tracking, dose delivery and adapted treatment planning [1]. Furthermore, these devices also allow functional lung imaging in the clinical workflow for treatment response monitoring without prolonging treatments. Several methods have been developed for non-contrast enhanced functional lung MRI at 1.5 T e.g. PREFUL [2] or Non-uniform Fourier Decomposition (NuFD) [3] to assess ventilation and perfusion. Since low-field MRI has been shown advantageous for lung imaging due to low susceptibility artefacts [4], we aim at demonstrating the feasibility and potential of NuFD for a 0.35 T MR-Linac and propose two signal normalization strategies for enhancing reproducibility of the results.

Methods

Ten healthy volunteers (five male, five female) were repeatedly scanned at a 0.35 T MR-Linac (MRIdian, ViewRay Inc., Cleveland, Ohio) using an optimized balanced steady-state free precession (bSSFP) sequence with flip angle=70°, TR/TE=2.42 ms/1.02 ms, FOV=500x500x20 mm³, matrix=128x128 and frame rate=3.68 images/s. Two coronal slices, referred to as 'aorta' and 'lung' slice were selected for each volunteer and image series (240 images) were acquired in normal free-breathing with breaks inside and outside the scanner as well as in deep and shallow breathing. After the image registration using ANTs and segmentation, the average lung signal was filtered into signals corresponding to ventilation and perfusion. The NuFD was performed pixel-wise and ventilation and perfusion maps were generated from the peak-value in the respective Fourier spectrum. For intra-volunteer ventilation map reproducibility, a normalization factor was defined based on the linear correlation of ventilation signal and diaphragm position of each scan as well as the diaphragm motion amplitude of the reference scan. This allows to correct the signal's dependence on the diaphragm motion amplitude, which varies with breathing pattern. The second strategy normalizes the ventilation maps with the average ventilation signal within a selected ROI and therefore eliminates the dependency on the signal amplitude.

Results

Due to a clear signal variation corresponding to the breathing frequency and the heart beat, the NuFD algorithm was successfully applied to all volunteer scans and ventilation and perfusion maps were generated. Comparing the normalization results of all volunteer scans, for the aorta slice a median deviation of 8.3%/6.0% (normalization factor/ROI normalization) and for the arbitrary lung slice of 7.7%/14.5% from the reference scan were achieved. This outperformed the uncorrected deviations of 29.2% and 34.4% for the aorta and lung slice, respectively. Combining both slices, a median deviation of 7.9%/12.2% was reached

compared to 31.3% for the uncorrected scans.

Conclusion

We were able to show that non-contrast enhanced functional lung MRI concepts can be transferred to a 0.35 T MR-Linac. In order to allow the comparison of intra-volunteer scans, two signal normalization strategies have been successfully introduced and demonstrated comparable performance. Due to the lack of dedicated equipment and the short acquisition, this method is easily integrable into the clinical treatment workflow.

[1] Crockett, Cathryn B et al. "Initial Clinical Experience of MR-Guided Radiotherapy for Non-Small Cell Lung Cancer." *Frontiers in oncology* vol. 11 617681. 10 Mar. 2021

[2] Pöhler, Gesa H et al. "Repeatability of Phase-Resolved Functional Lung (PREFUL)-MRI Ventilation and Perfusion Parameters in Healthy Subjects and COPD Patients." *Journal of magnetic resonance imaging : JMIR* vol. 53,3 (2021): 915-927

[3] Bondesson, David et al. "Nonuniform Fourier-decomposition MRI for ventilation- and perfusion-weighted imaging of the lung." *Magnetic resonance in medicine* vol. 82,4 (2019): 1312-1321

[4] Hori, Masaaki et al. "Low-Field Magnetic Resonance Imaging: Its History and Renaissance." *Investigative radiology* vol. 56,11 (2021): 669-679

Session:
Paediatric Lung Disease
Abstracts No. 500 – 502

Abstract No. 500


 + ORAL
PRESENTATION

Lung pathophysiology of preterm-born children using hyperpolarised ^{129}Xe lung MRI

Ho-Fung Chan^{1,*}, Laurie Smith¹, Alberto Biancardi¹, Guilhem Collier¹, Jody Bray¹, Helen Marshall¹, Paul Hughes¹, Madhwesha Rao¹, Graham Norquay¹, Andrew Swift¹, Kylie Hartz³, Michael Cousins^{2,3}, W. John Watkins², Sailesh Kotecha^{2,3}, and Jim Wild¹

¹University of Sheffield

²Cardiff University

³Cardiff and Vale University Health Board

*Presenting author

Introduction Decreased lung function or prematurity-associated lung disease (PLD) is common following preterm birth (<37 weeks' gestation). PLD may be associated with different early life factors, such as bronchopulmonary dysplasia (BPD) and gestation, and may result in distinct disease endotypes. Hyperpolarised ^{129}Xe MRI is highly sensitive to lung function abnormalities and could play a role in phenotyping different PLD disease endotypes. In this study we assessed the relationship between the historical diagnosis of BPD and current lung function on lung ventilation, microstructure and gas exchange metrics in preterm-born children using hyperpolarised ^{129}Xe MRI.

Methods 63 children (aged 9-13 years), including 44 preterm-born (34 weeks' gestation) and 19 term-born controls, were assessed with hyperpolarised ^{129}Xe MRI on a 1.5T GE HDx scanner as part of the Respiratory Health Outcomes in Neonates study (EudraCT: 2015-003712-20). All children underwent 3D ^{129}Xe ventilation^[1] and diffusion-weighted MRI^[2]; while dissolved ^{129}Xe whole lung spectroscopy^[3] was acquired in 51 children (34 preterm-born, 17 term-born) only. ^{129}Xe metrics derived were: ventilation defect percentage (VDP) and ventilation heterogeneity index (VHI) from ^{129}Xe ventilation MRI, global mean alveolar dimension (L_{mD}) and L_{mD} interquartile range (IQR) from ^{129}Xe diffusion-weighted MRI, and the ratio of ^{129}Xe dissolved in the red blood cells (RBC) and membrane compartments (RBC/M) from ^{129}Xe spectroscopy data.

Preterm-born children were classified, using spirometry, into prematurity-associated obstructive lung disease (POLD, n=13); prematurity-associated preserved ratio of impaired spirometry (pPRISm, n=4); preterm- (PTc, n=27) and term-born controls; and into those with BPD (n=11) and no-BPD (n=33). One-way ANOVA with post-hoc Tukey's tests was performed to assess differences across the lung function or BPD groups for all ^{129}Xe metrics.

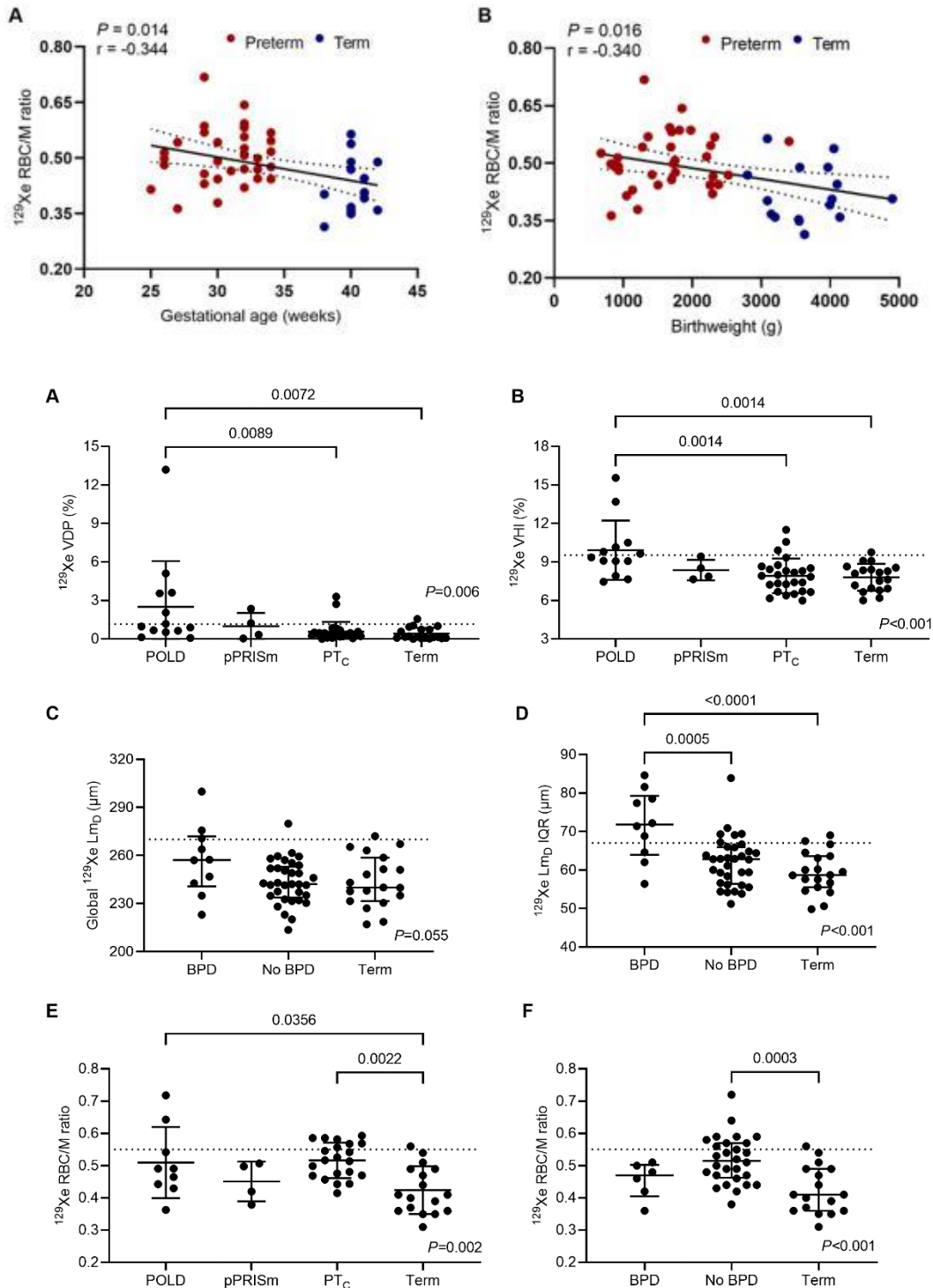
Results Significantly higher ^{129}Xe VDP (p=0.009, p=0.007), ^{129}Xe VHI (p=0.001, p=0.001) was observed in the POLD group when compared to the PTc and term-born groups, respectively (Fig 1A-B). In contrast, ^{129}Xe L_{mD} IQR was significantly increased in preterm-born children with BPD when compared to both the no-BPD (p<0.001) and the term-born control (p<0.001) groups indicating alterations of alveolar dimensions (Fig 1D). These results demonstrate that ^{129}Xe ventilation heterogeneity is often abnormal in those with a current obstructive pattern of lung disease; while increased ^{129}Xe alveolar dimension metrics are associated with a historical BPD diagnosis.

^{129}Xe RBC/M ratio was significantly increased for preterm-born groups when compared with term-born controls: POLD (p=0.036), PTc (p=0.002), no-BPD (p<0.001) (Fig 1E-F), suggesting that these differences are related to preterm birth regardless of current lung function and/or historical BPD diagnosis. This is further supported by significant correlations between RBC/M ratio with gestational age (p=0.014, r=0.344) and birthweight (p=0.016, r=0.340) (Fig 2). Increased ^{129}Xe RBC/M in preterm-born children could result from simplified alveolar geometry with reduced alveolar septation and membrane surface area, caused by birth at an early stage of lung development^[4].

Conclusion In preterm-born children ^{129}Xe ventilation abnormalities were found in those with POLD, whilst BPD in infancy was associated with abnormal lung microstructure.

Furthermore, ^{129}Xe RBC/M ratio was elevated in preterm-born children due to reduced alveolar septation from birth at an early stage of lung development.

1. Stewart NJ, Norquay G, Griffiths PD, Wild JM. Feasibility of human lung ventilation imaging using highly polarized naturally abundant xenon and optimized three-dimensional steady-state free precession. *Magn Reson Med* 2015; 74(2): 346-352.
2. Chan HF, Stewart NJ, Norquay G, Collier GJ, Wild JM. 3D diffusion-weighted (^{129}Xe) MRI for whole lung morphometry. *Magn Reson Med* 2018; 79(6): 2986-2995.
3. Collier GJ, Eaden JA, Hughes PJC, Bianchi SM, et al. Dissolved (^{129}Xe) lung MRI with four-echo 3D radial spectroscopic imaging: Quantification of regional gas transfer in idiopathic pulmonary fibrosis. *Magn Reson Med* 2021; 85(5): 2622-2633.
4. Moschino L, Bonadies L, Baraldi E. Lung growth and pulmonary function after prematurity and bronchopulmonary dysplasia. *Pediatr Pulmonol* 2021; 56(11): 3499-3508.



POLD (Prematurity-associated obstructive lung disease) ($\text{FEV}_1 \leq \text{LLN}$, $\text{FEV}_1/\text{FVC} \leq \text{LLN}$);
pPRISm (Prematurity-associated preserved ratio of impaired spirometry) ($\text{FEV}_1 \leq \text{LLN}$, $\text{FEV}_1/\text{FVC} > \text{LLN}$);
PT_C (Preterm control) ($\text{FEV}_1 > \text{LLN}$); **BPD** (Preterm with BPD diagnosis); **No BPD** (Preterm with no BPD);
Term (Term-born control)



Abstract No. 501

EFFECT OF KAFTRIO THERAPY ON 3D PHASE-RESOLVED FUNCTIONAL LUNG VENTILATION MRI IN CF PATIENTS

Filip Klimeš^{1,2,}, Andreas Voskrebenezv^{1,2}, Marcel Gutberlet^{1,2}, Milan Speth^{1,2}, Robert Grimm³, Martha Dohna¹, Gesine Hansen^{1,2}, Frank Wacker^{1,2}, Diane Renz¹, Anna-Maria Dittrich^{1,2}, and Jens Vogel-Claussen^{1,2}*

¹Hannover Medical School, Hannover

²Biomedical Research in Endstage and Obstructive Lung Disease (BREATH), German Center for Lung Research

³Siemens Healthcare GmbH, Erlangen, Germany

*Presenting author

Introduction

In a recent study, Elexacaftor/Tezacaftor/Ivacaftor (Elx/Tez/Iva) treatment has been shown to improve global clinical ventilation parameters and the semi-quantitative morphologic MRI scoring in cystic fibrosis (CF) patients (1). 3D phase-resolved functional lung (PREFUL) MRI is a promising technique, which enables quantitative assessment of pulmonary ventilation during free breathing on a regional level of the total lung volume (2). 3D PREFUL ventilation parameters have been shown to correlate well with spirometric measurements and showed a good interscan reproducibility in a study cohort consisting of healthy volunteers and chronic obstructive pulmonary disease patients (3). However it is unknown, whether 3D PREFUL parameters are sensitive to post-treatment changes. The objective of this study was to investigate if the ventilation parameters derived by 3D PREFUL are able to measure response to Elx/Tez/Iva therapy by comparison to clinical outcome in CF patients.

Methods

Ventilation parameters of 23 CF patients (13 female, age range: 13-46 years) were measured by MRI, spirometry and multiple breath washout (MBW) at baseline and 11-28 weeks after initiation of Elx/Tez/Iva therapy. In addition to morphological sequences as described before (1), a 8 minute 3D PREFUL measurement (2) was used to assess regional lung ventilation. Morphological images were evaluated using MRI based on a well-established semi-quantitative scoring system (4) (including Morphology, Mucus and Global score), and 3D PREFUL functional scans were assessed by ventilation defect percentage (VDP) maps derived from static regional ventilation (RVent) and dynamic cross-correlation (CC) map based on previously published thresholds (3). Further, spirometry outcomes were forced expiratory volume in 1second (FEV1) and forced expiratory flow at 25% (FEF25) of forced vital capacity. Also, lung clearance index (LCI) was assessed using the MBW technique.

The treatment effect on all derived parameters was analyzed by Bland-Altman plot analyses. Differences were tested for significance using Wilcoxon signed rank test. Post-treatment agreement between 3D PREFUL VDPs and clinical parameters was evaluated using Pearson correlation (r) analyses.

Results

Therapy with Elx/Tez/Iva significantly improved all ventilation markers including VDP parameters derived by 3D PREFUL (all $P < 0.0116$, Table 1). Relative change differences of 3D PREFUL VDP parameters were similar to relative change differences of FEV1 and LCI and slightly lower than relative change differences of FEF25 and all MRI scores. In posttreatment

analysis, 3D PREFUL derived VDP values significantly correlated to all clinical outcome parameters (all $r > 0.43$, all $P < 0.04$, Table 2), except for correlation of VDP_{CC} with Morphology and Mucus Scores.

Discussion & Conclusion

3D PREFUL MRI shows significantly reduced ventilation defects (19-22%) after Elx/Tez/Iva

therapy. The relative change differences of 3D PREFUL VDP parameters are in agreement with FEV₁ % pred. and LCI. The significant correlations in post-treatment analysis especially with FEV₁ % pred, LCI and global MRI score suggest that 3D PREFUL is sensitive to lung parenchyma ventilation changes induced by Elx/Tez/Iva therapy. Future multicenter validation studies are necessary to investigate if 3D PREFUL-MRI regional ventilation assessment may add value to current clinical standard techniques as spirometry, MBW, or gas-based MRI techniques.

1. Graeber SY et al. *Am J Respir Crit Care Med.* May 2022.; 2. Klimeš F et al. *Magn Reson Med.* 2021.; 3. Klimeš F et al. *J Magn Reson Imaging.* 2021.; Eichinger M et al. *Eur J Radiol.* 2012.

Tables

Table 1. Analysis of 3D PREFUL, spirometry, MBW and morphological MRI parameters in response to Elexacaftor/Tezacaftor/Ivacaftor therapy. Baseline and post treatment ventilation values are expressed as average with standard deviation in brackets. Significant results are marked with *.

Parameter	Baseline	Post Treatment	Mean Difference	P value	Relative change [%]
VDP _{RVent} [%]	18.2 (8.9)	14.0 (9.3)	4.2	0.0035*	-18.8
VDP _{CC} [%]	10.0 (8.0)	5.6 (6.7)	4.4	0.0116*	-21.6
FEV ₁ % pred. [%]	87.8 (19.4)	105.7 (18.8)	-18	<0.0001*	22.4
FEF25 % pred. [%]	55.3 (26.5)	89.4 (43.5)	-34.2	<0.0001*	74.7
LCI [-]	10.2 (3.0)	7.9 (3.0)	2.3	<0.0001*	-22.4
Morphology Score [-]	17.9 (5.1)	11.8 (4.1)	6.1	<0.0001*	-31.9
Mucus Score [-]	5.6 (4.1)	1.7 (2.5)	3.8	<0.0001*	-49.5
Global Score [-]	23.1 (7.6)	15.8 (6.2)	7.3	<0.0001*	-30.1

Table 2. Post-treatment correlation analysis of 3D PREFUL VDP parameters to clinical and morphological MRI parameters. Significant correlations are marked with *.

Parameter	VDP _{RVent}		VDP _{CC}	
	Pearson r	P	Pearson r	P
FEV ₁ % pred.	-0.65	0.0008*	-0.67	0.0005*
FEF25 % pred.	-0.56	0.0059*	-0.57	0.0047*
LCI	0.82	<0.0001*	0.67	0.0008*
Morphology Score	0.47	0.0252*	0.37	0.0785
Mucus Score	0.43	0.0419*	0.30	0.1677
Global Score	0.59	0.0033*	0.47	0.0231*

Abstract No. 502

Deep learning-based classification of perfusion defects in chest MRI for cystic fibrosis

Friedemann G. Ringwald^{1,*}, Luca Dulz¹, Anna Martynova¹, Urs Eisenmann¹, and Mark Wielpütz²

¹Heidelberg University Hospital

²Dept. of Diagnostic & Interventional Radiology, University Hospital Heidelberg; Translational Lung Research Center, a member of DZL, Heidelberg, Germany

*Presenting author

In the assessment of cystic fibrosis (CF) lung disease, magnetic resonance imaging (MRI) has been introduced as a valuable radiation-free alternative to computed tomography scans. It is used for routine imaging, monitoring of disease progression, therapy response and interventional trials. A morpho-functional MRI scoring system with six different items was developed to evaluate and compare MRI from different examinations, including the scoring of lung perfusion abnormalities amongst other [1]. Manual, visual scoring by a human operator is tedious, time-consuming and prone to inter- and intra-reader variability [2]. Hence, a fully automated approach such as deep learning is desirable for reader-independent and reproducible measurement of CF lung disease severity based on MRI. In this work we propose an automated classification of lung perfusion abnormalities in CF on perfusion MRI. Standardised 1.5T MRI has been performed at the Heidelberg University Hospital for more than a decade, incl. 4D perfusion imaging with injection of 0.1 mmol/kg bodyweight of gadolinium-based contrast material. Patients of all age groups ranging from 3 months to 51 years of age were scanned. A pool of patients was selected where all necessary data was available. In total, 669 individual MRI scans were retrieved and used for training of a custom pre-trained convolutional neural network (CNN). The perfusion defect score was provided by a single experienced reader. Each lung lobe received a score from 0 to 2 depending on the amount of area affected by the perfusion defect. The data was grouped for the entire lung and lung halves. In order to achieve a semi-balanced distribution, additional grouping on part of the scores was utilized to reach a comparable number of MRIs in each group. Pre-processing in form of normalization and data augmentation using common augmentation techniques was conducted. Additionally, the lung was segmented with a semi-automatic approach using a NN-UNET. To receive a rough estimate for each lung half, the lung slices were split in the middle. Afterwards, training, validation and testing followed by hyperparameter tuning was used to receive a mean performance. Preliminary results showed an overall accuracy of 83.72% averaged over all classes with an average sensitivity of 47.32% and a specificity of 89.77%. While the lungs with very high or very low perfusion defects were classified quite well, lungs with intermediate scores averaged worse results. Nonetheless it was observed that misclassifications into the adjacent classes of the lungs with medium perfusion defects were quite common, which is in line with the reader variability for the scoring system [2]. Currently, additional pre-processing steps as well as methodological changes are being implemented such as extensive data augmentation and the use of additional views to improve the results and decrease variance. Special focus lies on the lung lobe segmentation in order to receive an overall better performance. Eventually, an automated classification of perfusion defects on MRI could support the radiologists, improve the diagnostic process and save time.

[1] Wielpütz MO, Puderbach M, Kopp-Schneider A, et al. Magnetic resonance imaging detects changes in structure and perfusion, and response to therapy in early cystic fibrosis lung disease. *Am J Respir Crit Care Med.* 2014;189(8):956-965.

[2] Eichinger M, Optazait DE, Kopp-Schneider A, et al. Morphologic and functional scoring of cystic fibrosis lung disease using MRI. *Eur J Radiol.* 2012;81(6):1321-1329.

Session:
Pre-clinical DZL Session
Abstracts No. 600 - 602

Abstract No. 600

Classifying the monopodial bronchopulmonary vasculature - A cluster based performance analysis

Jonas Labode^{1,}, Christian Dullin², Willi L. Wagner³, Despoina Myti⁴, Rory E. Morty⁴, and Christian Mühlfeld¹*

¹Medizinische Hochschule Hannover

²University Medical Center Göttingen

³University of Heidelberg

⁴Translational Lung Research Center

*Presenting author

The pulmonary artery tree of mammals is composed of functionally different sub segments, whose design changes along the path through the organ. A morphological analysis of the vessel tree is thus advanced by grouping its branch segments into biologically similar groups. In contrast to the human lung with its dichotomous branching pattern, the lungs of the most widely used animal models of pulmonary disease have a monopodial branching pattern which exhibits a high degree of asymmetry. Thus, established methods of classification deliver widely different results when employed on the same monopodial lung. To address this problem, we formulate and demonstrate a workflow to quantify the precision of various grouping methods employed to the monopodial lung.

A mouse lung was imaged using synchrotron micro computed tomography. The resulting volume image was digitally segmented and the vessel tree extracted. Measurements were acquired for each of its segments. Different grouping algorithms taken from the literature, such as (Strahler) order and (fractal) generations were then employed on the vessel tree. Additionally, a grouping approach based on morphological features, as opposed to location in the vessel tree, was employed for comparison purposes.

Significant differences in method performance were observed. The Strahler order could be identified as the best performing method of the tested set. Both orders and generations, standard methods for characterizing human lung structure, were unable to provide results of comparable precision. Additionally, the morphology based clustering approach demonstrated the possibility to achieve groupings of even higher precision.

*Labode, J.; Dullin, C.; Wagner, W. L.; Myti, D.; Morty, R. E. & Mühlfeld, C.; Evaluation of classifications of the monopodial bronchopulmonary vasculature using clustering methods, *Histochemistry and Cell Biology*, 2022, DOI: 10.1007/s00418-022-02116-x*

Abstract No. 601

Characterization of the cellular contacts between alveolar epithelial type 2 cells and fibroblasts

supak Panpeng^{1,*}, Julia Schipke¹, Christoph Wrede¹, and Lars Knudsen¹

¹Institute for Functional and Applied Anatomy, Hannover Medical School, Hannover

*Presenting author

Communication between alveolar epithelial type 2 cells (AE2) and fibroblasts (FB) is involved in inflammatory response and fibrogenesis in the lung. Previous studies mentioned cellular contacts between AE2 cell and FB through apertures in the basal lamina, however, the precise ultrastructure of these contacts have not been investigated. In this study, lung parenchyma from a healthy human donor lung was analyzed by focused ion beam scanning electron microscopy. The resulting high-resolution data was utilized to reconstruct a 3-dimensional model of a septal region spanning two AE2 cells and their corresponding basal lamina and, two fibroblasts. We observed eight and eleven contact sites per AE2 cell. The ultrastructure of the contact is comprised of foot processes of the AE2 cells with or without cytoplasmic extensions of FB. One complex contact area consisting of AE2 cell foot processes, cell protrusions of two FBs and one prominent elastic fiber was found. AE2 cell foot processes generally appear as clusters, which scatter over the basal surface of these cells. Interestingly, some of them coil underneath the intact basal lamina. The foot processes show differences in morphology (e.g. length, orientation, and branching). The apertures in the basal lamina are round or oval and vary in size. Despite the low number of investigated AE2 cell and FB, our results reveal the diversity and the special ultrastructure of the intercellular AE2-FB contacts, the possible number of contact site per cell, the actual shape and size of the aperture in the basal lamina. These findings complement the previous descriptions and define the precise morphology of the cellular contacts between AE2 cell and FB.

Sirianni FE, Chu FS, Walker DC. Human alveolar wall fibroblasts directly link epithelial type 2 cells to capillary endothelium. *Am J Respir Crit Care Med.* 2003 Dec 15;168(12):1532-7. doi: 10.1164/rccm.200303-371OC. Epub 2003 Oct 9. PMID: 14551162.

Sirianni FE, Milaninezhad A, Chu FS, Walker DC. Alteration of fibroblast architecture and loss of Basal lamina apertures in human emphysematous lung. *Am J Respir Crit Care Med.* 2006 Mar 15;173(6):632-8. doi: 10.1164/rccm.200509-1434OC. Epub 2006 Jan 13

Adamson IY, Hedgecock C, Bowden DH. Epithelial cell-fibroblast interactions in lung injury and repair. *Am J Pathol.* 1990 Aug;137(2):385-92. PMID: 1696785; PMCID: PMC1877605

Abstract No. 602

An optimized protocol for vascular casting of infant and adult mouse lungs for micro-CT imaging

Zhe Zhou-Suckow^{1,}, Qian Li², Willi Wagner², Jolanthe Schatterny¹, Martin Finke², Mark Wielpütz², Hans-Ulrich Kauczor², and Rory E. Morty¹*

¹Dept. of Translational Pulmonology, University Hospital Heidelberg; Translational Lung Research Center (TLRC), a member of DZL, Heidelberg, Germany

²Dept. of Diagnostic & Interventional Radiology, University Hospital Heidelberg; Translational Lung Research Center, a member of DZL, Heidelberg, Germany

*Presenting author

Alterations to the pulmonary vasculature are observed in many lung diseases. Vascular casting is a technique that provides an effective method to examine the vascular architecture of normal and pathological tissues. Little information is currently available that described the preparation and filling of the pulmonary vascular network in mice for radiological studies. The aims of this study were to 1) optimize vascular casting to produce high-resolution images of the pulmonary vascular tree in mice of different ages; 2) to apply this technique in the Scnn1b-Tg mouse model of cystic fibrosis (CF)-like lung disease and evaluate the pulmonary vasculature changes, which features are often hidden components of CF lung disease and thus have not been intensively studied. First of all, wild-type (WT) mice of postnatal ages of 10 days, and 4, 8, and 12 weeks were deeply anesthetized and heparinized, a PE-10 catheter was inserted into the pulmonary artery, and the vasculature was flushed of blood via a syringe pump. The lungs were inflated via the trachea at a standard pressure. Microfil MV-120, prepared at a ratio of 8:10:1 parts of polymer: diluent: curing agent, was infused into the vascular bed at a specified flow rate/volume. After filling and curing, the lung vasculature was imaged on a micro-CT scanner (SykScan1176, Bruker) using the following setting: aluminum filter (0.2mm), energy (45kV and 555µA), high resolution (i.e. 1000 projections), voxel size (9µm) and exposure time (730ms). Next, we used Microfil compound to cast the pulmonary arteries in 6 and 10-week-old Scnn1b-Tg mice and WT controls, and assessed the status of peripheral vascular bed by determining the fractional vessel volume and vascular surface density, using VGSTUDIO MAX (Volume Graphics GmbH, Germany). From infant to adult mice, we improved the pulmonary artery injection technique in catheter placement/stabilization, established a guideline for the flow rate/volume according to the animal age/size, and yielded ~70% casting success. The fractional vessel volume and vascular surface density were significantly lower in both 6 and 10-week-old Scnn1b-Tg mice compared to WT controls, indicating the reduction of vascular bed, a proof of concept of pulmonary vascular remodeling in the diseased mice. In summary, our data provide important groundwork for the radiological imaging of the pulmonary vasculature, for future studies on bronchopulmonary dysplasia and pulmonary hypertension, and other murine models of lung diseases that involve the remodeling of vasculature.

Session:
Pulmonary Vascular Disease
Abstracts No. 700 – 701

Abstract No. 700

A Stepwise Approach to Pulmonary Hypertension for Radiologists

*Ki Yeol Lee*¹, *Yu Whan Oh*², *Sung Ho Hwang*², *Eun Ju Chun*³, *Jeon Joo Woo*⁴, and *Sang Min Lee*⁵

¹Korea University Hospital

²Korea University Anam Hospital, Seoul, South Korea

³Seoul National University Bundang Hospital, Seongnam, South Korea. South Korea

⁴Nowon Eulji University Hospital, Seoul, South Korea.

⁵Asan Medical Center, University of Ulsan College of Medicine, Seoul, South Korea.

PURPOSE :

Pulmonary hypertension (PH), defined as the elevation of mean pulmonary arterial pressure (mPAP) above 25 mmHg, has numerous causes, which the World Health Organization (WHO) has divided into five distinct categories based upon the underlying mechanism of action. A number of imaging tools are utilized in the evaluation of PH, such as chest X-ray, computed tomography (CT), ventilation/perfusion (V/Q) scan, cardiac magnetic resonance imaging, dual-energy CT and single-photon emission computed tomography/computed tomography V/Q scanning. The purpose of this exhibit is to review the clinical, pathologic, and imaging findings of these unique cases which have caused increased pulmonary arterial pressure and specific characteristics which help narrow the differential diagnosis.

MATERIALS AND METHOD :

We reviewed 1345 patients with PH with a variety of causes, including idiopathic pulmonary hypertension (PH) or secondary PH. We propose a step-by-step approach for diagnosing the causes and PH of pulmonary hypertension associated with various etiologies.

RESULTS :

We discuss the various causes of idiopathic or secondary PH such as connective tissue disease, portal hypertension, congenital heart disease, venous/capillary disease (PVOD), lung disease, pulmonary arterial occlusion, metabolic disorders, fibrosing mediastinitis, etc. We want to identify the underlying disease and demonstrate the diagnostic process and clinical outcome.

CONCLUSION :

Accurate diagnosis and appropriate treatment of PH are associated with important clinical, functional and quality-of-life benefits and often longer survival. Here, we outline an approach for the accurate diagnosis and timely management of patients with PH.

Eur Radiol 2021; 31:6230-38

Radiology 2021; 298:531-49

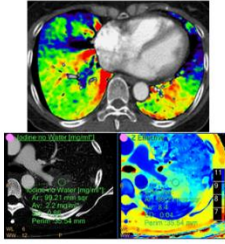
RadioGraphics 2018; 38:357-73

Pulm Circ 2016; 6:70-81

4.1 CTEPH

Looking for Specific cases

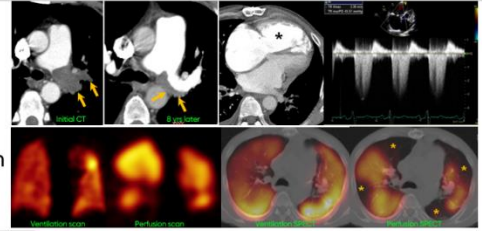
Evaluation of pulmonary perfusion —Dual-energy CT (DECT)



- Pulmonary perfusion can be evaluated using DECT images taken at 140 kVp and 80 kVp
- DECT can measure **contrast uptake in the lung parenchyma as an indicator of pulmonary arterial perfusion** and is highly sensitive to perfusion defect.

Radiographics 2016; 36(7):91-92. Radiographics 2016; 36(8):91-92

51-year-old man with dyspnea, edema



CTEPH: Chronic Thromboembolic Pulmonary Hypertension

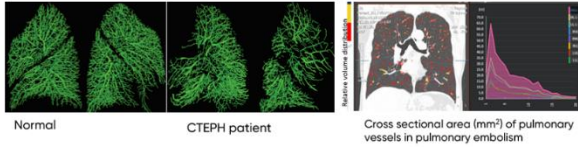
- Initial CT scan shows filling defect in the left and LUL pulmonary artery.
- Despite of anticoagulant treatment, eccentric filling defect remains on CT after 8 years, MPA dilates, and RV becomes hypertrophic. The pulmonary arterial pressure was 113 mmHg on 2D echocardiography.
- Ventilation and perfusion SPECT show the mis-matched perfusion defect "V/Q mismatch".
- This patient underwent pulmonary endarterectomy, but the outcome was poor.

The Pulmonary Arteries

Looking for Pulmonary Arteries

Pruning of peripheral pulmonary vessels in PH

- CTEPH
 - > pruning of the distal vasculature due to loss of precapillary vessels
 - > dilation of the central pulmonary arteries
 - > tortuous-appearing vessels
- COPD, ILD, asthma, etc.



Normal

CTEPH patient

Cross sectional area (mm²) of pulmonary vessels in pulmonary embolism

Pulm Crit Care 2016; 4(30):81. Chest 2021; 150(6):72

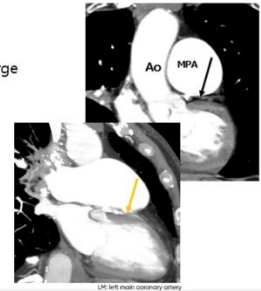
Cardiac Complications, miscellaneous

Pericardial effusion

- Relatively common
- Higher mortality, particularly when moderate or large
- Minimal hemodynamic impact

Left main coronary artery compression

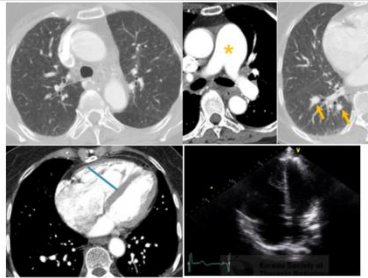
- Dynamic stenosis of LM due to PA compression
 - Take off angle < 60°
 - MPA to LM Distance < 1 mm
 - Stenosis ≥ 50%
- Anginal Sx
- Relieved with percutaneous coronary intervention



J Am Coll Cardiol 2012; 60(5):597. Fluid One 2018; 13(2):202-49. Radiology 2021; 298(5):149

LM: left main coronary artery

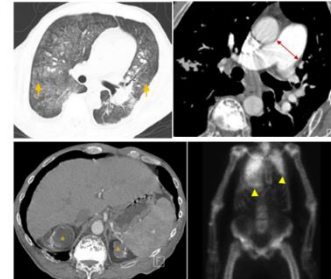
48-year-old man with dyspnea on exertion, one year ago



Pulmonary Capillary Hemangiomas

- CT scans show innumerable ground glass nodules in both lungs, enlarged MPA (asterisk).
- The ratio of the segmental pulmonary artery to the segment bronchus is > 1 indicating pulmonary hypertension (arrows).
- The pulmonary arterial pressure on 2D echocardiography was 115 mmHg.

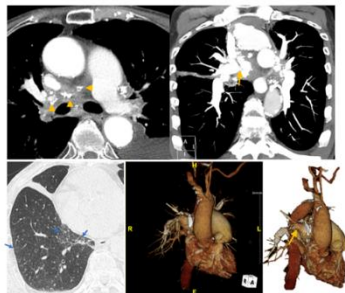
60-year-old man with dyspnea



Metastatic pulmonary calcification with PH due to chronic renal failure

- CT scans show centrilobular GGO and solid nodules in both lungs (yellow arrows) and enlargement of the main pulmonary artery.
- Abdominal CT scan shows atrophy of both kidneys suggesting chronic renal insufficiency.
- Technetium^{99m} bone scan displays diffuse uptake in both lungs.

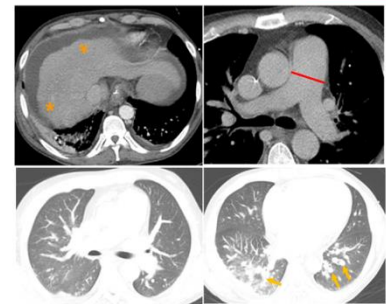
40-year-old woman with chest pain and dyspnea



Fibrosing mediastinitis with PH

- Soft tissue lesion in the middle mediastinum with scattered calcifications (arrowheads) and narrowing of the right pulmonary artery (yellow arrow).
- Thickening of interlobular septa (blue arrows) and major fissure.

49-year-old man with shortness of breath



Portopulmonary hypertension

- Axial CT sections show nodular liver surface, enlarged MPA, diffuse GGO in both lungs.
- The ratio of the segmental pulmonary artery to the segmental bronchus is > 1, which indicates pulmonary hypertension (arrows).

Abstract No. 701

Reproducibility of Pulmonary MRA in Adults with Muco-Obstructive Pulmonary Disease

Lena Wucherpfennig^{1, 2, *}, *Simon M. F. Triphan*^{3, 2}, *Oliver Weinheimer*^{3, 4}, *Monika Eichinger*^{5, 2}, *Sabine Wege*^{5, 2}, *Ralf Eberhardt*^{6, 7}, *Michael U. Puderbach*^{8, 9}, *Hans-Ulrich Kauczor*^{3, 4}, *Claus P. Heußel*^{5, 4}, *Gudula Heußel*⁵, and *Mark O. Wielpütz*^{10, 2}

¹Diagnostic and Interventional Radiology

²German Center for Lung Research (DZL)

³University Hospital Heidelberg

⁴German Lung Research Center (DZL)

⁵Thoraxklinik at University Hospital Heidelberg

⁶Asklepios Clinic Barmbek

⁷Thoraxklinik at University hospital Heidelberg

⁸Hufeland Hospital Bad Langensalza

⁹University hospital Heidelberg

¹⁰University of Heidelberg

*Presenting author

Background:

Recent studies support magnetic resonance angiography (MRA) as a diagnostic tool for pulmonary arterial disease.

Purpose:

To determine MRA image quality and reproducibility, and the dependence of MRA image quality and reproducibility on disease severity in patients with chronic-obstructive pulmonary disease (COPD) and cystic fibrosis (CF).

Material and Methods:

20 patients with COPD (66.5±8.9y, FEV1%=42.0±13.3%) and 15 with CF (29.3±9.3y, FEV1%=66.6±15.8%) underwent morpho-functional chest MRI including time-resolved MRA twice one month apart (MRI1, MRI2), and COPD patients underwent non-contrast CT. Image quality was assessed visually using standardised subjective 5-point scales. Contrast-to-noise-ratio (CNR) and signal-to-noise-ratio (SNR) were measured by regions-of-interest.

Disease severity was determined by spirometry, a well-evaluated chest MRI score and by computational CT emphysema index (EI) for COPD.

Results:

Subjective image quality was diagnostic for all MRA at MRI1 and MRI2 (mean score=4.7±0.6). CNR and SNR were 43.8±8.7 and 50.5±8.7, respectively. Neither image quality score nor CNR or SNR correlated with FEV1% or chest MRI score for COPD and CF (r=0.239-0.248). CNR and SNR did not change from MRI1 to MRI2 (p=0.434-0.995). Further, insignificant differences in CNR and SNR between MRA at MRI1 and MRI2 did not correlate with FEV1% nor chest MRI score in COPD and CF (r=-0.238-0.183), nor with EI in COPD (r=0.100-0.111).

Conclusion:

MRA achieved diagnostic quality in COPD and CF patients and was highly reproducible irrespective of disease severity. This supports MRA as a robust alternative to CT in patients with underlying muco-obstructive lung disease.

Session:
Technical Advances in
Functional Lung Imaging
Abstracts No. 800 – 814

Abstract No. 800

Challenging 3D MR spirometry biomarkers with respect to gravity

Nathalie Barrau¹, Killian Sambourg¹, Angéline Nemeth¹, Brice Fernandez², Tanguy Boucneau², Vincent Lebon¹, and Xavier Maître¹

¹Université Paris-Saclay, CEA, CNRS, Inserm, BioMaps, Orsay, France

²GE Healthcare, Buc, France

INTRODUCTION

3D MR spirometry carries a double paradigm shift from standard spirometry: from forced to free maneuvers and from global to local measurements [1]. The technique regionally characterizes lung function under free breathing with voxel-wise flow-volume loops. Beyond the parameters extracted from these curves, original biomechanical markers are also produced. In this study, sensitivity and repeatability of main 3D MR spirometry parameters were challenged with respect to gravity.

METHODS

Ten-minute dynamic lung MRIs were performed on nine healthy volunteers, freely breathing in supine then prone positions, with repeated acquisitions for each position. The study was performed at 3T using an ultrashort echo time (UTE) sequence combined with an AZTEK trajectory [2]. Retrospective gating was performed over twenty respiratory phases using selfnavigation. Reconstructed dynamics images were then elastically registered and the resulting deformation fields were used to establish flow-volume loops in each voxel of the lung.

Five parameters from free breathing spirometry [3] were computed for every loop: tidal volume (TV), volume until spontaneous peak expiratory flow (VSPEF), spontaneous peak expiratory flow (SPEF), spontaneous expiratory flow at remaining 25% of expiration (SEF25), with their corresponding ratios VSPEF/TV and SEF25/SPEF. From the Green-Lagrange tensor [1][4], we derived five additional parameters taken at global end of inspiration for the slab-rob index (SRI) and at their maximal mean value over the respiratory cycle for anisotropic deformation index (ADI) and strain tensor components for anatomical directions (superior-inferior, E_SI, left-right, E_LR, anterior-posterior, E_AP).

Intra-subject repeatability of the technique was locally assessed after spatial normalization of repeated acquisitions, and globally after integrating maps throughout the lung. Local repeatability was assessed using absolute measurements. To probe gravity lung dependence, anterior and posterior regions were separated into two equal volumes and paired Wilcoxon tests, performed.

RESULTS

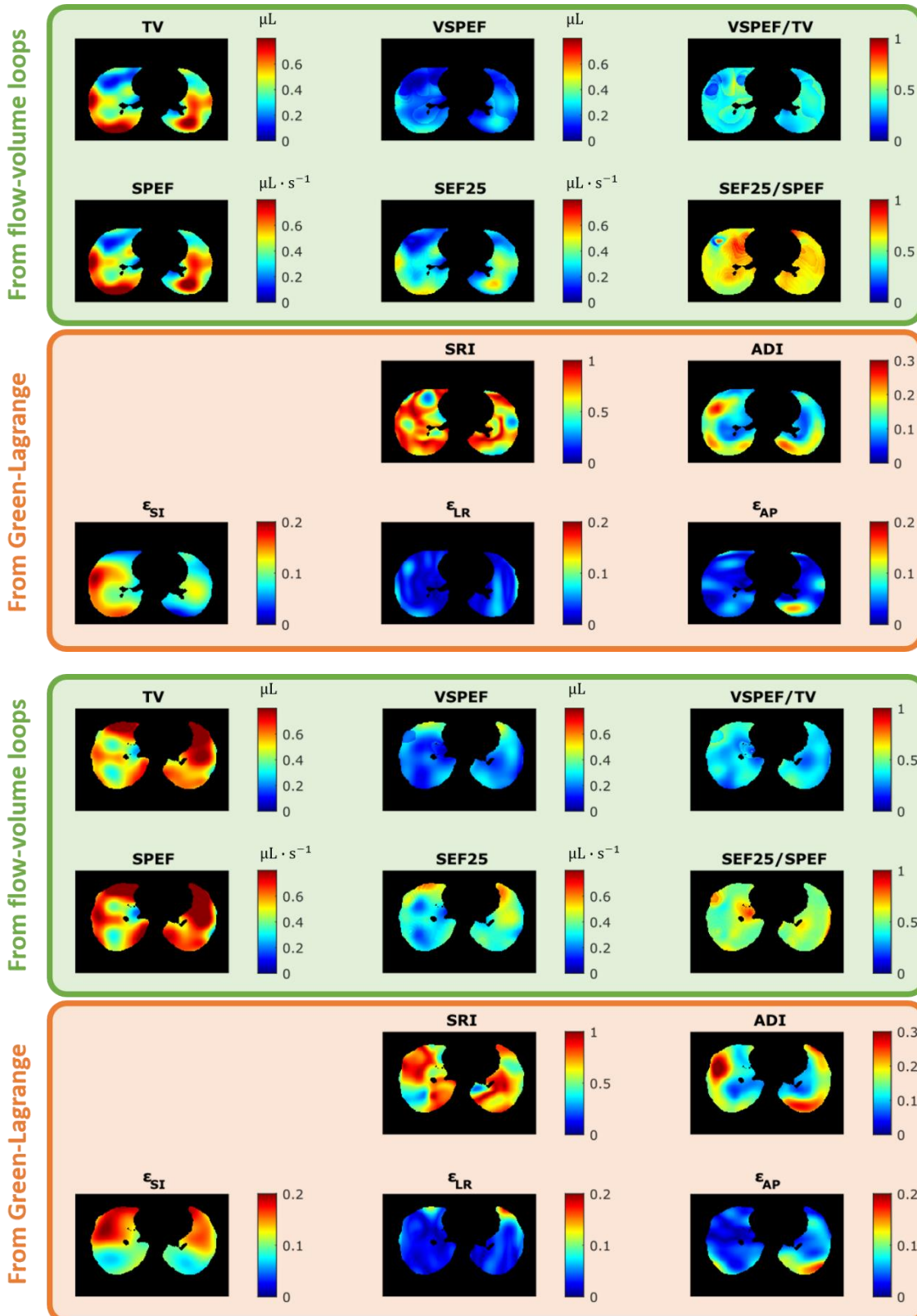
Typical parametric maps are provided for a healthy subject in supine (Figure 1) and prone (Figure 2) positions. Biomarkers had global variation rates ranging from 4% (SRI) up to 15% (SEF25). Absolute local measurements present important variations between repeated acquisitions (31% for TV and 28% for SPEF). TV, VSPEF, SPEF and E_SI are found higher in the anterior region for prone and in the posterior region for supine. They are significantly different between anterior and posterior regions for both positions ($p < 0.05$). SRI shows very different spatial distribution between positions with anterior-posterior dependence in supine. The dominant strain component _SI supports ventilation along the superior-inferior axis, which would be governed by the diaphragm, either in the anterior (prone) or posterior (supine) parts. E_SI lateral discrepancy is compensated by E_AP higher values in the other lung. E_LR plays little role.

DISCUSSION

Over ventilation parameters (TV, VSPEF, SPEF) and strain components (E_SI), 3D MR spirometry reveals the lung gravity dependence in functional and mechanical ways. The different values between left and right lungs might be explained by the heart, which would (1) enforce the left dependence in prone and (2) constraint the left lung mechanics along the

superior-inferior axis especially in supine. These preliminary outcomes highlight the rich three-dimensional biomechanics of the lung.

1. Boucneau, T., Fernandez, B., Larson, P., Darrasse, L., & Maître, X. (2020). 3D magnetic resonance spirometry. *Scientific Reports*, 10(1), 1-12.
2. Boucneau, T., Fernandez, B., Besson, F. L., Menini, A., Wiesinger, F., Durand, E., ... & Maître, X. (2021). AZTEK: Adaptive zero TE kspace trajectories. *Magnetic Resonance in Medicine*, 85(2), 926-935.
3. Carlsen, K. L., Magnus, P., & Carlsen, K. H. (1994). Lung function by tidal breathing in awake healthy newborn infants. *European Respiratory Journal*, 7(9), 1660-1668.
4. Amelon, R., Cao, K., Ding, K., Christensen, G. E., Reinhardt, J. M., & Raghavan, M. L. (2011). Threedimensional characterization of regional lung deformation. *Journal of biomechanics*, 44(13), 2489-2495.



Abstract No. 801

Phase-resolved functional lung imaging (PREFUL) with ultrashort echo time sequence (PUTE)

Lea Behrendt^{1,2,*}, Marcel Gutberlet^{1,2}, Andreas Voskrebenev^{1,2}, Filip Klimes^{1,2}, Arnd J. Obert^{1,2}, Agilo L. Kern^{1,2}, Frank Wacker^{1,2}, and Jens Vogel-Claussen^{1,2}

¹Institute for Diagnostic and Interventional Radiology

²Biomedical Research in Endstage and Obstructive Lung Disease Hannover (BREATH)

*Presenting author

Introduction

Phase-resolved functional lung (PREFUL) MRI₁ is a free breathing 1H lung MRI postprocessing technique to gain dynamic ventilation and perfusion information from one data set, acquired at echo times >0.6ms_{2,3}. Due to short T2* times in lung tissue, sequences with ultrashort echo times (UTE) are desirable to gain more signal. A combination of PREFUL with a 2D ultrashort echo time sequence (PUTE) was developed and ventilation parameters were compared to PREFUL derived from a spoiled gradient echo sequence (SPGRE).

Methods

A 2D UTE sequence was developed according to Triphan et al.⁴. All spokes were sorted according to their respiratory phase and dynamic image reconstruction was performed.

UTE and SPGRE scans were performed in free breathing for one healthy subject and one COPD patient with the following sequence parameters:

- UTE: TE 0.07ms, TR 2.3ms/3.2ms, FoV 500x500mm², in plane resolution 2.8mm², slice thickness (ST) 12.5mm, measurement time 99s/48s.
- SPGRE: TE 0.82ms, TR 3ms, FoV 500x500mm², in plane resolution 3.9mm², ST 12.5mm/15mm, measurement time 99s/48s.

Data sets were evaluated with PREFUL postprocessing. Regional ventilation (RV) maps, ventilation defect percentage (VDP) maps and the dynamic respiratory cycle (DRC) were compared.

Results

A similar visual appearance of ventilation maps derived with SPGRE-PREFUL and PUTE is shown. However, more ventilation defects can be seen for PUTE. For the COPD patient, the same areas with ventilation defects are present in the ventilation maps and the DRCs. For the healthy subject, both DRCs showed homogeneous ventilation.

Conclusion

We could show the feasibility of PUTE with regional ventilation similarities on visual inspection compared to SPGRE-PREFUL.

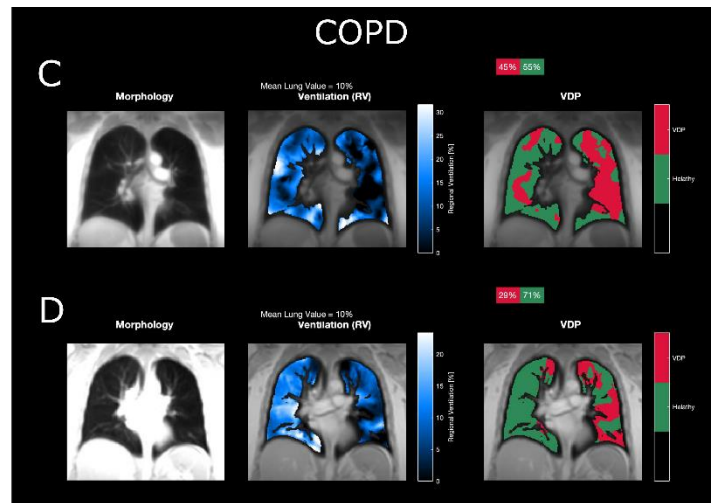
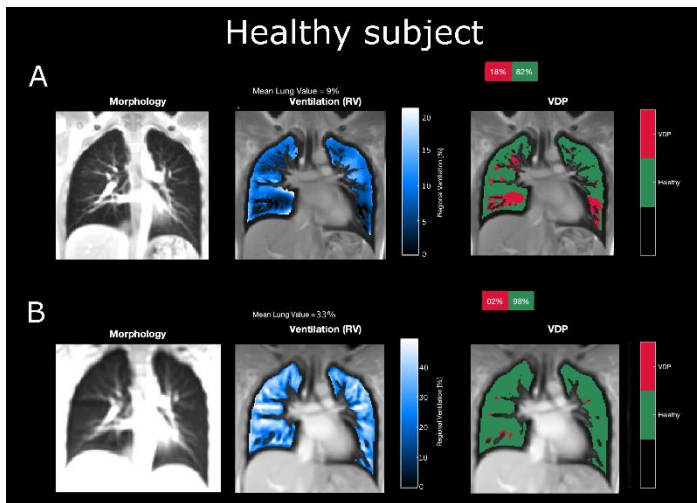
Further analysis in patient cohorts is necessary as well as the examination of perfusion parameters and the adjustment of PREFUL settings for PUTE.

1. Voskrebenev A, Gutberlet M, et al. Feasibility of quantitative regional ventilation and perfusion mapping with phase-resolved functional lung (PREFUL) MRI in healthy volunteers and COPD, CTEPH, and CF patients. *Magn Reson Med* 2018; 79: 2306–2314.

2. Klimes F, Voskrebenev A, Gutberlet M, et al. Free-breathing quantification of regional ventilation derived by phase-resolved functional lung (PREFUL) MRI. *NMR Biomed*; 32. Epub ahead of print 1 June 2019. DOI: 10.1002/nbm.4088.

3. Behrendt L, Smith LJ, Voskrebenev A, et al. *Pulm Circ* 2022; 12: e12054.

4. Triphan SMF, Breuer FA, Gensler D, et al. Oxygen enhanced lung MRI by simultaneous measurement of T₁ and T₂* during free breathing using ultrashort TE. *J Magn Reson Imaging* 2015; 41: 1708–1714.



Abstract No. 802

Lung Development in a Murine Model of CF-like Lung

Sanja Blaskovic^{1,*}, Pinelopi Anagnostopoulou², Florian Kronig¹, Elena Borisova¹, Dominik Schittny¹, Sai Krishnan Ganesh¹, Zhe Zhou-Suckow³, Marcus A. Mall^{4,5}, Christian Matthias Schlepütz⁶, Marco Stampanoni⁶, and Johannes Constantin Schittny¹

¹Institute of Anatomy, University of Bern, Switzerland

²Medical School, University of Cyprus, Nicosia, Cyprus,

³Translational Lung Research Center (TLRC), a member of the German Center for Lung Research

(DZL), Heidelberg, Germany

⁴Charité - Universitätsmedizin Berlin

⁵German Center for Lung Research (DZL)

⁶Swiss Light Source, Paul Scherrer Institute, Villigen PSI, Switzerland

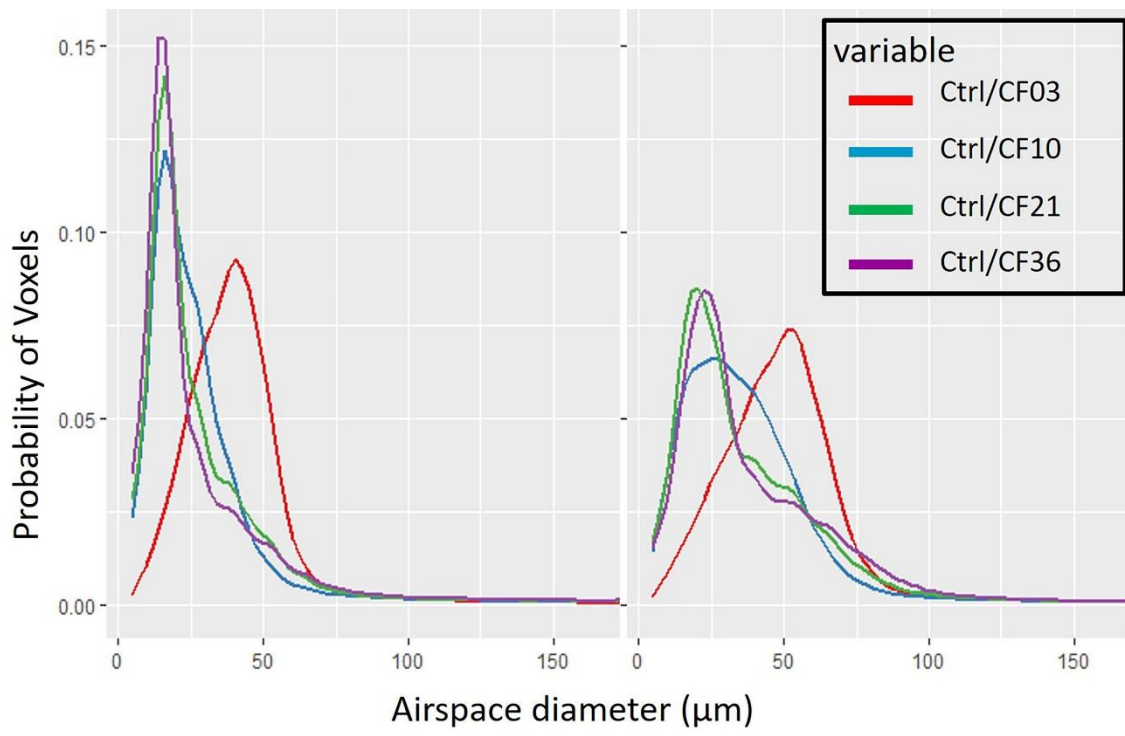
*Presenting author

RATIONALE: Cystic fibrosis (CF), an inherited disease caused by mutations of the Cystic fibrosis transmembrane conductance regulator (CFTR) gene, is characterized by thick airway mucus, which favors airway infections that lead to structural changes and lung function decline. Recent clinical and experimental studies suggest that lung structural changes occur early in life even in the absence of infections. We hypothesized that CF might affect prenatal and early lung development on the level of branching morphogenesis and alveolarization. We aimed to compare the airspace diameters in healthy and CF mouse lungs at different stages of post-natal lung development, by applying X-ray tomographic high resolution imaging followed by structural analysis.

METHODS: Lungs from ENaC-transgenic (tg) mice with CF-like lung disease (CF) and control (ctrl) littermates were obtained at postnatal day (pnd) 3, 10, 21 and 36 (n=8 per genotype and age group, both males and females) and scanned at a pixel size of 1.6 μm using synchrotron radiation based X-ray tomographic microscopy (beamline TOMCAT, Swiss Light Source, Paul-Scherrer-Institut, Villigen, Switzerland). The images were reconstructed with gridrec algorithm and stitched using the non-rigid stitching algorithm NRStitcher. The segmentation of the lung was performed with the combination of Ilastik and ImageJ and the airspace diameters were determined by applying the pi2 thickness map algorithm. Histograms were calculated by voxel counting.

RESULTS: We observed the dilatation of airspaces already at pnd3 in mice with CF-like lung disease when comparing airspace probability distributions diameter means (60 ± 2.6 vs. 50 ± 4.15 μm, $p=0.001391$) and peaks (51 ± 4 vs. 42 ± 2.3 μm, $p=0.001974$) (Figure 1). When analyzing the total voxel count for conducting airways, we found that they were significantly bigger in the CF group at pnd3 (peak position: 92 ± 3 vs. 86 ± 3 μm, $p=0.004$; peak height: $13 \times 10^6 \pm 2 \times 10^6$ vs. $10 \times 10^6 \pm 2 \times 10^6$ μm, $p=0.04$; peak width: 72 ± 11 vs. 49 ± 12 μm, $p=0.005$). Dilatation of total airspaces in CF group vs. controls was observed at all other analyzed days (diameter means: 47 ± 5 vs. 38 ± 3 μm, $p=0.001$ at day 10, 47 ± 3 vs. 41 ± 2 μm, $p=0.001$ at day 21, 52 ± 2.8 vs. 41.5 ± 2.5 μm, $p=8.1 \times 10^{-6}$ at day 36 and peaks: 30.5 ± 10 vs. 16 ± 2 μm, $p=0.002$ at day 10, 21 ± 3 vs. 16.5 ± 2 μm, $p=0.02$ at day 21, 24 ± 3 vs. 15 ± 1 μm, $p=1.1 \times 10^{-5}$ at day 36) (Figure 1). The surface areas under the histogram fit curve were comparable in CF and ctrl mice of the same age.

CONCLUSION: In the ENaC-tg mice we observed enlarged airspaces throughout postnatal lung development. However, our mice did not show any histological signs of infections. The enlarged airspaces we observed in CF mice soon after birth (day3) are likely the effect of prenatal mucus obstruction and pulmonary overextension on fetal branching morphogenesis. The progression of the phenotype may be caused by further mucus obstruction and inflammation. Our results confirm clinical observations and are suggestive of a beneficiary effect of starting therapy early after birth in patients with CF.



Abstract No. 803

Analysis of regional differences of airspace diameters in rat lungs

Sai Krishnan Ganesh^{1,}, Elena Borisova², and Johannes Schittny¹*¹University of Bern²Paul Scherrer Institute

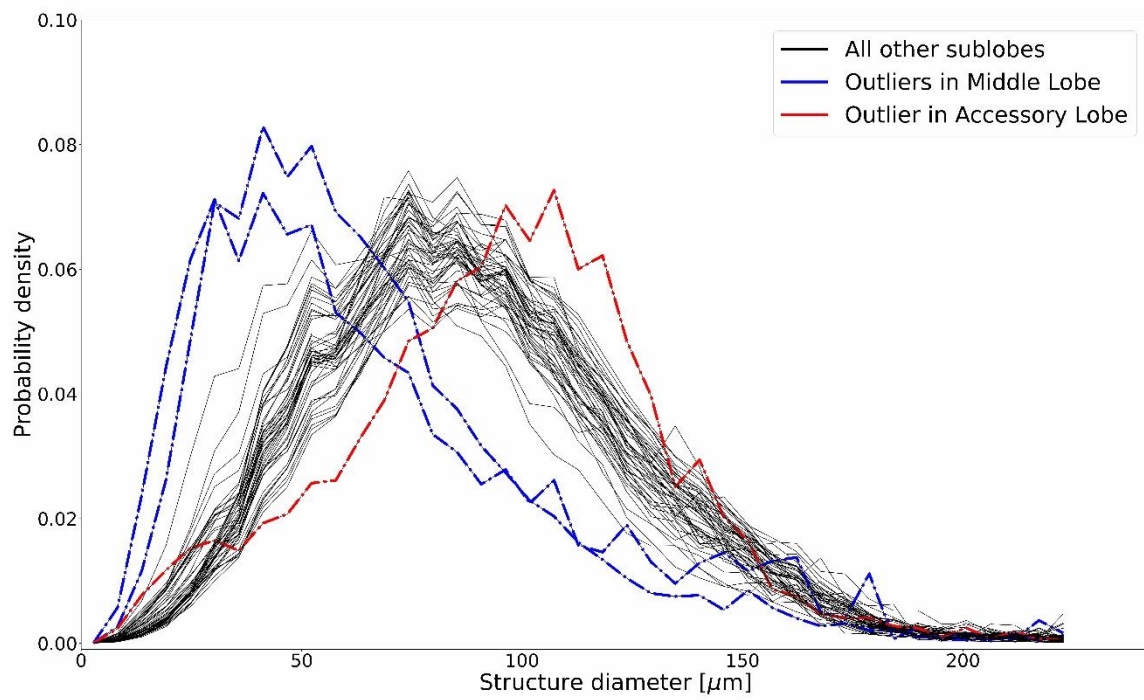
*Presenting author

Rationale: A characterisation of the size of lung structures may contribute to a better understanding of lung physiology, because differences of airspace sizes have an influence on pulmonary ventilation and particle deposition. Now we are asking, if the airspace size distribution may be related to this finding. We performed a quantitative, high resolution analysis of the distribution and homogeneity of the airspace diameters of a juvenile rat lung based on an already published open access dataset (<https://doi.org/10.16907/7eb141d3-11f1-47a6-9d0e-76f8832ed1b2>).

Methods: X-ray tomographic microscopy measurements of the fresh postmortem lungs of a 13-day-old Wistar rat were scanned at the TOMCAT beam-line (Swiss Light Source, Paul-Scherrer-Institute, Villigen, Switzerland) with an effective pixel size of 2.75 x 2.75 μ m. One of the first steps of analysing and quantifying the data is segmentation. Labels are assigned to different parts of data corresponding to air, tissue and bone region. The output of the segmentation is a binary image, where slices contain the label mask of the airways in the lung. Lobes and lobular sub-regions were segmented for further analysis. Airspace diameters were determined using the pi2 software package. Probability density maps were calculated by voxel counting.

Results: High-resolution tomographic datasets of a juvenile rat lung allowed a visualisation and a voxel-based estimation of the airspace diameters. Comparing lung lobes and sub-lobal regions, we observed a quite homogenous distribution of airspace diameters. However, we detected small regional inhomogeneities in a few regions in the middle lobe. The total range of airspace diameters were recorded in the range of 3-220 μ m with a peak at 50-150 μ m.

Conclusion: This analysis helped us in the quantification of the airspace diameters across all the lung lobes. The distribution of the airspace diameters were homogenous across the different regions of the lung lobes. We hypothesise that the described higher particled deposition in caudal over cranial regions is not related to airspace diameters. Most likely, it is related to difference of ventilation. In addition, structural difference of the conducting airways may be also important. A better understanding of this can be helpful for further studies of lung structure and function at a new level of resolution and detail.



Abstract No. 804

Perfusion quantification using voxel-wise proton density and median signal decay in PREFUL MRI

Julian Glandorf^{1,2,*}, Filip Klimes^{1,2}, Lea Behrendt^{1,2}, Andreas Voskrebenzev^{1,2}, Till Kaireit^{1,2}, Marcel Gutberlet^{1,2}, Frank Wacker^{1,2}, and Jens Vogel-Claussen^{1,2}

¹Institute for Diagnostic and Interventional Radiology

²Biomedical Research in Endstage and Obstructive Lung Disease Hannover (BREATH)

*Presenting author

Purpose: Contrast-free lung MRI based on Fourier decomposition is an attractive method to monitor various lung diseases. However, the accuracy of the current perfusion quantification is limited. In this study, a new approach for perfusion quantification based on voxel-wise proton density and median signal decay toward the steady state for Fourier decomposition based

techniques is proposed called QQuantified (QQuant).

Methods: Twenty patients with chronic obstructive pulmonary disease and 18 patients with chronic thromboembolic pulmonary hypertension received phase-resolved functional lung-MRI (PREFUL) and dynamic contrast-enhanced (DCE)-MRI. Nine healthy participants received phase-resolved functional lung-MRI only. Median values of QQuant were compared to a Fourier decomposition perfusion quantification presented by Kjørstad et al (QKjørstad) and validated toward pulmonary blood flow derived by DCE-MRI (PBFDC). Blood fraction maps determined by the new approach were calculated. Regional and global correlation coefficients were calculated, and Bland-Altman plots were created. Histogram analyses of all cohorts were created.

Results: The introduced parameter QQuant showed only 2 mL/min/100 mL mean deviation to PBFDC in the patient cohort and showed less bias than QKjørstad. Significant increases of regional correlation with PBFDC were achieved ($r = 0.3$ vs. $r = 0.2$, $P < .01^*$). The trend of global correlation toward PBFDC is not uniform, showing higher values for QKjørstad in the chronic obstructive pulmonary disease cohort than for QQuant and vice versa in the chronic thromboembolic pulmonary hypertension cohort. In contrast to QKjørstad, QQuant perfusion maps indicate a physiologic dorsoventral gradient in supine position similar to PBFDC with similar value distribution in the histograms.

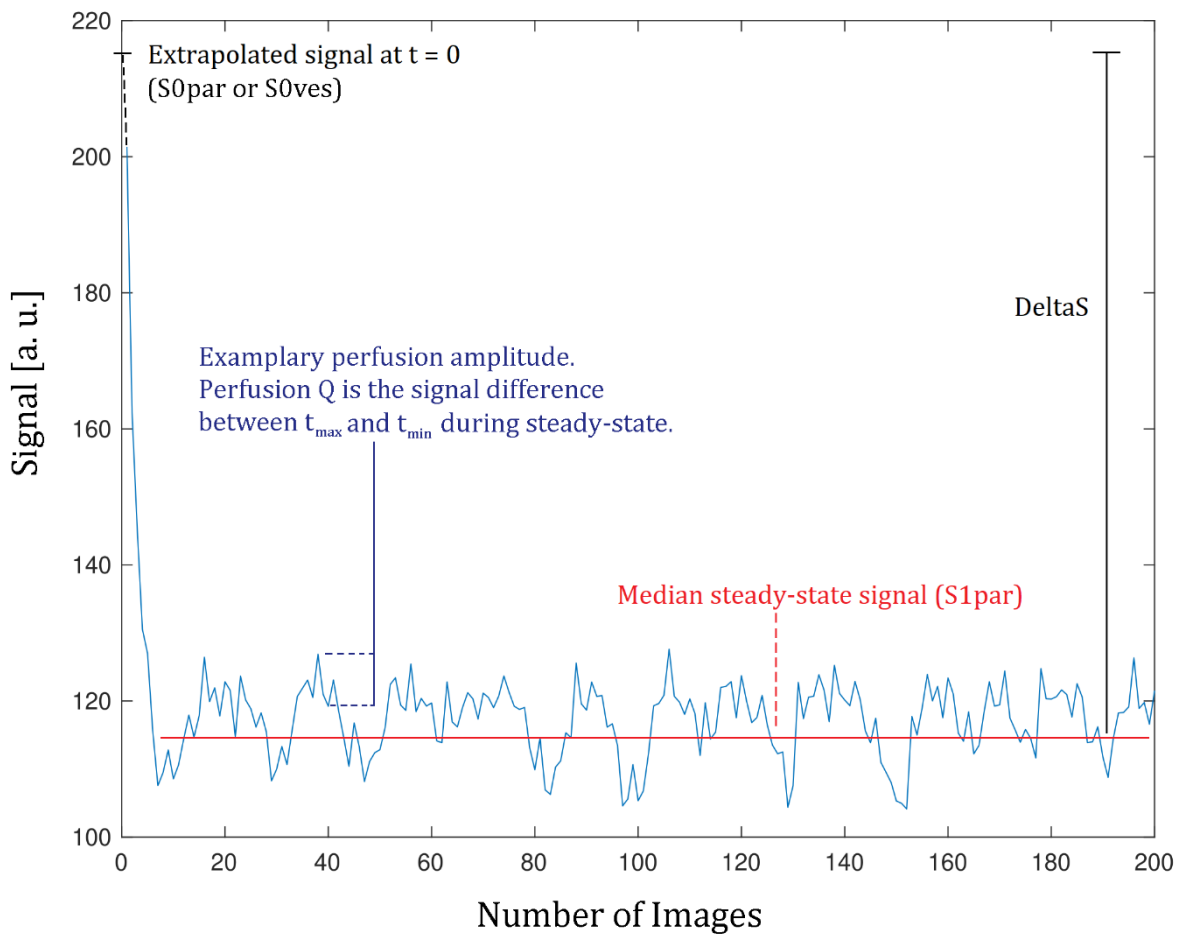
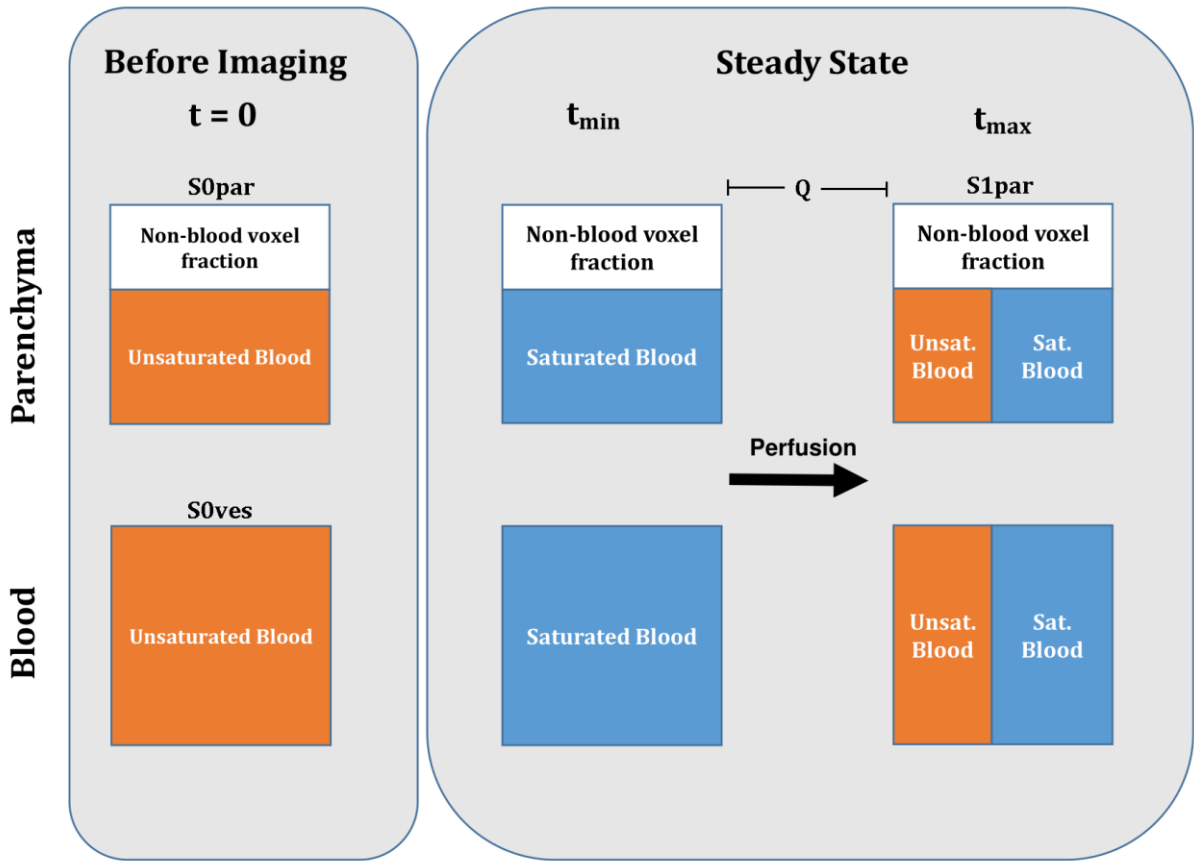
Conclusion: We proposed a new approach for perfusion quantification of phase-resolved functional lung measurements. The developed parameter QQuant reveals a higher accuracy compared to QKjørstad.

Kjørstad , Corteville DMR, Fischer A, et al. Quantitative lung perfusion evaluation using Fourier decomposition perfusion MRI. Magn Reson Med. 2014;72:558-562.

Kjørstad , Corteville DMR, Henzler T, Schmid-Bindert G, Zilner FG, Schad LR. Non-invasive quantitative pulmonary V/Q imaging using Fourier decomposition MRI at 1.5T. Z Med Phys. 2015;25:326-332.

Voskrebenzev A, Gutberlet M, Klimes F, et al. Feasibility of quantitative regional ventilation and perfusion mapping with phase-resolved functional lung (PREFUL) MRI in healthy volunteers and COPD, CTEPH, and CF patients. Magn Reson Med. 2018;79:2306-2314

Bauman G, Puderbach M, Deimling M, et al. Non-contrast- enhanced perfusion and ventilation assessment of the human lung by means of Fourier decomposition in proton MRI. Magn Reson Med. 2009;62:656-664.



Abstract No. 805

Hyperpolarized ^{129}Xe MRI shows changes in lung microstructure during the cardiac cycle

Agilo Kern^{1,2,*}, Marcel Gutberlet^{1,2}, Jens M. Hohlfeld^{3,2}, Frank Wacker^{1,2}, and Jens Vogel-Clausen^{1,2}

¹Hannover Medical School

²German Center for Lung Research (DZL)

³Fraunhofer Institute for Toxicology and Experimental Medicine

*Presenting author

Introduction

Many aspects of normal lung function and structure are still to be elucidated. Microscopy is typically used for lung morphometry but tissue fixation does not accurately conserve the in-vivo state.¹

CSSR spectroscopy combined with gas uptake models² is an experimental tool for non-invasive assessment of alveolar septal thickness, surface-to-volume ratio and capillary transit time. Influence of cardiac function on CSSR results has been acknowledged³ but is not well investigated. Results from microscopy indicate an influence of vascular pressure on pulmonary capillary diameters and consequently septal thickness but provide limited information on the in-vivo situation.⁴

Purpose of this study was to develop a Look–Locker-based rapid CSSR pulse sequence allowing measurement of uptake curves in different cardiac phases and to investigate the influence of cardiac function on CSSR in healthy volunteers.

Methods

A rapid CSSR sequence based on the Look–Locker approach was implemented. The study was approved by the institutional review board and all subjects provided written informed consent. 6 healthy volunteers underwent hyperpolarized ^{129}Xe MRI at 1.5T.

^{129}Xe was hyperpolarized, diluted with nitrogen to 1L and inhaled by subjects from functional residual capacity. Fingertip plethysmograms were recorded and gating signals stored in raw data.

To avoid potential delays in plethysmographic gating, spectra were interpolated to coarsely resolve the two dissolved-phase resonances and piecewise sine functions fit to filtered ratio data using plethysmographic data for starting values. Each readout was assigned to the phases crest and trough assuming widths of 40/60% (symmetric). The Patz model was fit to the uptake curves and results compared by signed-rank tests. Data were additionally analyzed in a sliding window of width 40% with a variable phase subtracted from the sine phase from piecewise fits.

Results

Figure 1 shows exemplary data and fitting results. There was a significant increase of septal thickness during crest of the pulse wave compared to trough, $p = 0.031$.

Figure 2 shows results from sliding-window reconstruction with varying phase in individual participants and averaged over the study group. Strong relative changes of capillary transit time are apparent.

Discussion

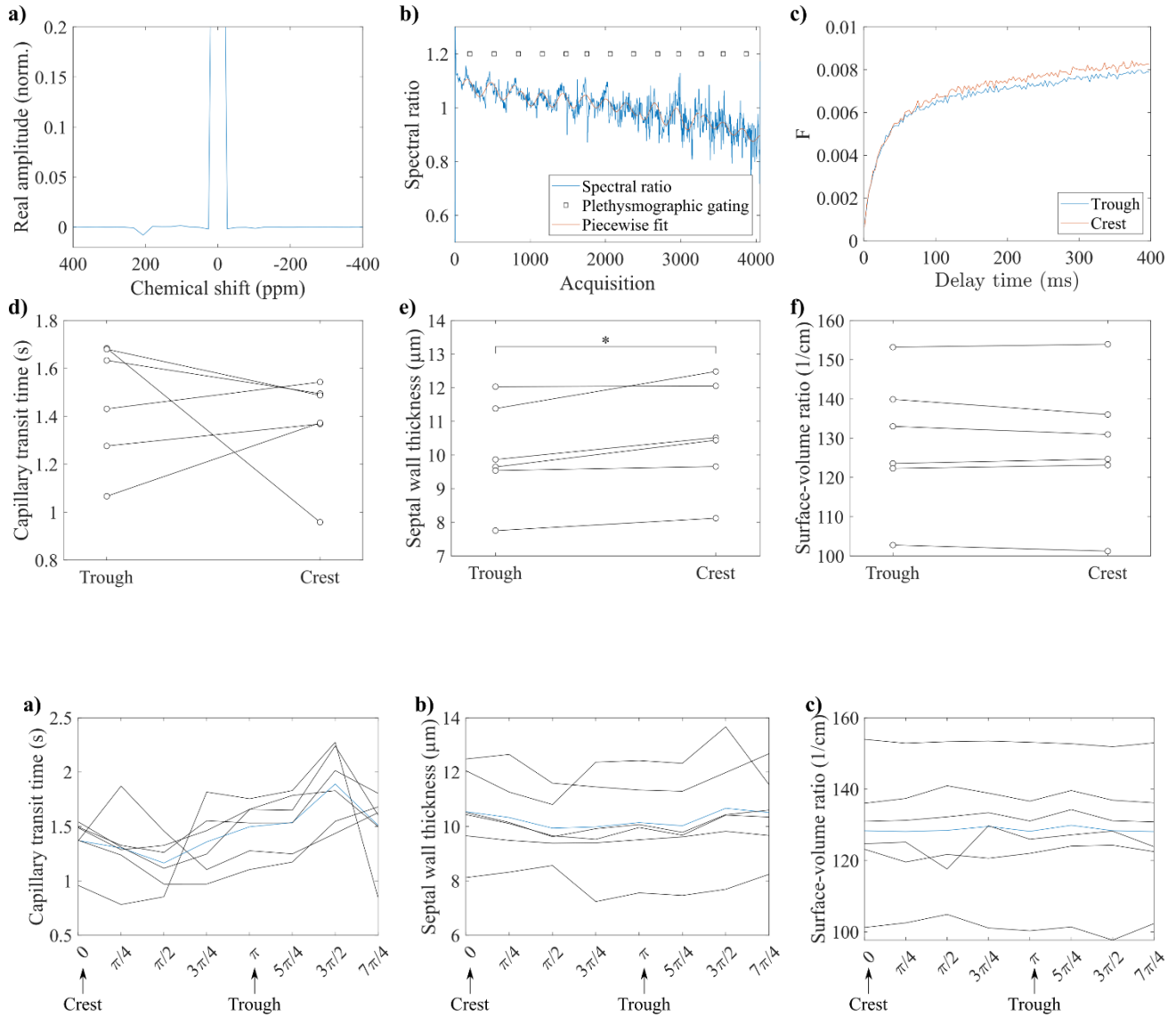
We found a significant difference of septal thickness between trough and crest of the blood pulse wave going through the lung consistent with diameter changes of pulmonary capillaries with blood pressure.⁴ The authors are not aware of a previous literature report of changes in septal thickness throughout the cardiac cycle. Previous studies found a periodic change in capillary blood flow for which we found no evidence, possibly due to changes in capillary diameter or due to the small cohort. Future studies involving MOXE analysis would require sacrificing temporal resolution to cleanly separate the dissolved-phase resonances. A potential clinical application could be discrimination of different cardiopulmonary diseases.

The method may have improved precision due to control of the cardiac influence.

Conclusion

Rapid CSSR may provide novel insights into physiological processes not well established in the literature. Septal thickness as obtained from rapid CSSR is influenced by the cardiac cycle. The precision of CSSR could potentially be improved by controlling the cardiac phase.

1. Hsia, C. C. et al. *Am J Respir Crit Care Med* 181, 394–418 (2010).
2. Patz, S. et al. *New J. Phys.* 13, 015009 (2011).
3. Ruppert, K. et al. *Magn. Reson. Med.* 75, 1771–1780 (2016).
4. Watson, R. R. et al. *Respir. Physiol. Neurobiol.* 160, 208–214 (2008).



Abstract No. 806

Long-COVID breathlessness underlying normal CT: Hyperpolarized Xenon-129 MRI & FAN model Analysis

Minsuok Kim^{1,*}, Jeongeun Hwang², James Grist³, Gabriele Abueid⁴, Vicente Grau³, Emily Fraser⁵, and Fergus Gleeson⁶

¹Loughborough University

²Korea University Guro Hospital

³University of Oxford

⁴Churchill Hospital, University of Oxford

⁵Oxford Interstitial Lung Disease Service

⁶Oxford NHS Foundation Trust

*Presenting author

Background: After two years of ongoing COVID-19 pandemic, we are now facing a new challenge. People who recovered from COVID-19 may experience a complex prolonged illness with persisting symptoms beyond the initial infection. It is defined as Long-COVID if the symptoms over weeks to months. Breathlessness is one of the most common symptoms in people with Long-COVID. It remains unclear, however, why some Long-COVID patients experience breathlessness despite normal CT scans. This study shows the characteristics of regional lung ventilation in Long-COVID using state-of-the-art functional imaging and computational modelling techniques to elucidate the association of small-scale regional ventilation impairment with breathlessness symptoms.

Materials and Methods: A total of twenty-two patients (male/female = 10/12; age = 49.5 ± 12.9) with Long-COVID underwent thoracic CT and hyperpolarized xenon-129 MRI (HPXMRI) scans followed by dyspnea-12 (D-12) survey. We used a CT image-based full-scale airway network (FAN) flow model to simulate dynamic ventilation in the Long-COVID lungs. The ventilation projection on a coronal plane and the percentage lobar ventilation were compared between HPX-MRI and FAN models. A weak ventilation zone was defined where gas concentration was lower than 10% of the lung mean. Fractal dimensions (FDs) of the weak ventilation zones in HPX-MRI and FAN models were calculated using a box-counting method to assess the heterogeneity in small airways. We compared the FDs between low D-12 (< 6) and high D-12 (> 6) score groups.

Results: HPX-MRI and FAN model showed excellent agreement in the ventilation distribution. There were no visible ventilation defects in either model or image, regardless of the dyspnea-12 score of the patients. The structure similarity index between the HPX-MRI and the FAN modelled ventilation projections on a coronal plane was 0.87 ± 0.04. The percentage lobar ventilation of the imaging and the model showed a strong correlation (r = 0.63, p < 0.001). The distribution of weak ventilation zone became more heterogeneous as D-12 scores increased. Consequently, the Spearman correlation between FD and D-12 score were r = 0.53 (p = 0.01) and r = 0.42 (p = 0.05) for HPX-MRI and FAN model, respectively. There was a significant difference in the FD of weak ventilation zones between the low and high D-12 groups (HPX-MRI: 1.97 and 2.08, p = 0.005; FAN: 2.60 and 2.64, p = 0.056).

Conclusions: Lung ventilation acquired from HPX-MRI and the FAN model shows significant similarities. The FAN model constructed from conventional CT scans can detect functional complications that result from small-scale airway impairments. Long-COVID patients with high FDs resulting from small airway impairments are more likely to experience breathlessness symptoms. Our imaging and modelling study provides insight into the role of pulmonary function of small airways affecting healthcare and suggests future research for a better understanding of Long-COVID.

Abstract No. 807

COMPARISON OF 3D PREFUL MRI TO 19F VENTILATION IMAGING IN PATIENTS WITH OBSTRUCTIVE LUNG DISEASES

Filip Klimeš^{1,2,}, Arnd Jonathan Obert^{1,2}, Andreas Voskrebenezv^{1,2}, Marcel Gutberlet^{1,2}, Robert Grimm³, Hendrik Suhling^{1,2}, Julian Glandorf^{1,2}, Till Kaireit^{1,2}, Tawfik Moher-Alsady^{1,2}, Frank Wacker^{1,2}, and Jens Vogel-Claussen^{1,2}*

¹Hannover Medical School, Hannover

²Biomedical Research in Endstage and Obstructive Lung Disease (BREATH), German Center for Lung Research

³Siemens Healthcare GmbH, Erlangen, Germany

*Presenting author

Introduction

3D phase-resolved functional lung (PREFUL) MRI allows for contrast-agent free regional evaluation of ventilation parameters within the whole lung parenchyma during tidal breathing (1). Until now a comparison of 3D PREFUL-derived ventilation parameters with direct measurement of ventilation using pulmonary gas MRI techniques (¹⁹F, ¹²⁹Xe) has not been carried out. In the current study, ventilation defect percentage (VDP) maps derived by 3D PREFUL were compared to VDP maps derived by fluorinated gas breath-hold ¹⁹F MRI in patients with obstructive lung disease.

Methods

Fourteen patients with chronic obstructive pulmonary disease (COPD) and 13 patients with asthma were examined. 3D PREFUL images were obtained during 8 minutes of free-breathing using a prototype golden-angle stack-of-stars sequence (1). After image reconstruction and image registration, 3D PREFUL VDP maps were derived for static regional ventilation (RVent) and dynamic cross-correlation (CC) ventilation parameters based on previously published thresholds (1,2).

During eight consecutive breaths of a C₃F₈/O₂ mixture ¹⁹F imaging was performed in breath-hold using a 3D gradient-echo pulse sequence (3). For each breath-hold a VDP map was calculated as the ratio between the defect lung volume (relative signal intensity < 20%, (4)) and the whole lung volume. Also a time to fill (TTF) in number of breaths map was derived for each lung parenchyma voxel by determining the number of breaths which is needed to ventilate the voxel, i.e. relative signal intensity > 20% (3). Subsequently, a TTF VDP map was calculated by considering voxels with a TTF > 4 breaths as ventilation defects.

VDP values derived from both techniques were compared on global level using Pearson correlation coefficient. The global analysis was followed by regional analysis, where the 3D PREFUL VDP maps were co-registered on 19F VDP maps and assessed using Sørensen-Dice and spatial overlap parameters.

Results

Similarities and differences were observed between 19F and 3D PREFUL VDP maps, as depicted in Figure 1. On global level, both 3D PREFUL VDP maps correlated significantly (all $r > 0.52$; all $P < 0.01$) with VDPTTF and VDP3-8 of 19F ventilation imaging (see Table 1A).

Regarding regional comparison, the best overlap of defect areas (see Table 1D) was between 3D PREFUL VDP maps and 19F derived VDPTTF and VDP1-2.

Discussion & Conclusion

3D PREFUL VDP maps showed good correlation with 19F VDPTTF on global level, however various differences were observed on a regional level. Differences may be explained by several factors. Firstly, the 19F signal is generated by gas density, whereas the PREFUL signal is modulated by the respiratory motion. Secondly, while 19F is a breath-hold technique, PREFUL enables ventilation assessment during free breathing. Different lung volumes may consequently result in different VDP values, which is in agreement with a previous publication on hyperpolarized gas imaging in healthy volunteers (5). Some

inaccuracies in spatial co-registration of VDP maps were observed, and also the spatial resolution was different: (3.9 x 3.9 x 3.9mm³) for 3D PREFUL compared to (6.25 x 6.25 x 15mm³) for ¹⁹F imaging, which might explain slightly different sensitivity for disease of both techniques.

Klimeš F et al. Magn Reson Med. 2021.; 2. Klimeš F et al. J Magn Reson Imaging. 2021.; 3. Obert AJ et al. Proc Intl Soc Mag Reson Med 28.; 4. He M et al. Acad Radiol. 2014.; 5. Hughes PJC et al. J Appl Physiol. 2019.

Table 1. Global (A) and regional comparison (B-D) of VDP maps derived by ¹⁹F ventilation imaging (in columns) and 3D PREFUL (in rows) method. Significant Pearson correlation coefficients (*r*) are marked with *. Correlation coefficients were compared using Fisher's Z-transformation for each *r* value. *P* value < 0.05 was considered as statistically significant. Spatial overlap and Sørensen-Dice coefficients are expressed as medians with interquartile range.

A. Pearson Correlation	VDP _{TTF}		VDP ₁		VDP ₂		VDP ₃		VDP ₄		VDP ₅		VDP ₆		VDP ₇		VDP ₈	
	<i>r</i>	<i>P</i>	<i>r</i>	<i>P</i>	<i>r</i>	<i>P</i>	<i>r</i>	<i>P</i>	<i>r</i>	<i>P</i>	<i>r</i>	<i>P</i>	<i>r</i>	<i>P</i>	<i>r</i>	<i>P</i>	<i>r</i>	<i>P</i>
VDP _{RVent}	0.57	<0.01*	0.12	0.54	0.37	0.06	0.58	<0.01*	0.67	<0.001*	0.65	<0.001*	0.62	<0.001*	0.64	<0.001*	0.62	<0.001*
VDP _{CC}	0.55	<0.01*	0.13	0.51	0.27	0.18	0.52	<0.01*	0.65	<0.001*	0.63	<0.001*	0.60	<0.001*	0.62	<0.001*	0.62	<0.001*
B. Spatial Overlap [%]	VDP _{TTF}		VDP ₁		VDP ₂		VDP ₃		VDP ₄		VDP ₅		VDP ₆		VDP ₇		VDP ₈	
	55.2 (50.2-58.3)		49.3 (47.6-52.4)		54.2 (49.9-57.6)		54.8 (50.2-59.8)		56.0 (51.1-59.9)		56.5 (51.4-60.2)		57.0 (51.2-60.0)		56.9 (51.5-59.8)		56.2 (51.3-59.8)	
56.8 (52.6-60.5)		51.1 (47.9-53.8)		56.2 (51.6-59.9)		56.3 (52.9-61.1)		57.1 (55.0-61.8)		57.2 (54.5-62.0)		58.7 (54.4-62.3)		59.4 (54.2-62.5)		59.6 (54.3-62.7)		
C. Dice Healthy [%]	VDP _{TTF}		VDP ₁		VDP ₂		VDP ₃		VDP ₄		VDP ₅		VDP ₆		VDP ₇		VDP ₈	
	63.6 (56.9-69.1)		49.5 (37.0-56.6)		63.1 (54.7-68.7)		66.8 (62.5-71.8)		69.7 (64.8-73.7)		70.1 (65.1-74.2)		70.0 (65.4-74.3)		70.4 (65.8-74.3)		69.9 (65.9-74.2)	
67.4 (60.5-71.5)		51.9 (38.3-59.8)		65.2 (56.6-71.1)		69.6 (64.7-74.6)		71.6 (67.1-75.6)		72.2 (68.4-75.6)		72.3 (68.7-75.8)		73.2 (68.7-75.9)		73.4 (68.3-76.0)		
D. Dice Defect [%]	VDP _{TTF}		VDP ₁		VDP ₂		VDP ₃		VDP ₄		VDP ₅		VDP ₆		VDP ₇		VDP ₈	
	37.4 (31.4-42.4)		48.8 (42.4-54.8)		36.9 (29.9-45.6)		26.0 (17.2-33.4)		16.7 (11.7-23.3)		11.5 (7.3-19.3)		8.2 (5.5-15.6)		7.2 (3.8-15.4)		8.1 (3.6-15.5)	
36.8 (32.3-42.6)		46.6 (42.0-54.2)		37.8 (30.5-44.3)		25.2 (17.8-35.6)		18.1 (11.6-24.1)		12.6 (8.2-20.4)		8.8 (6.0-17.4)		7.8 (4.2-16.1)		9.3 (4.1-16.4)		

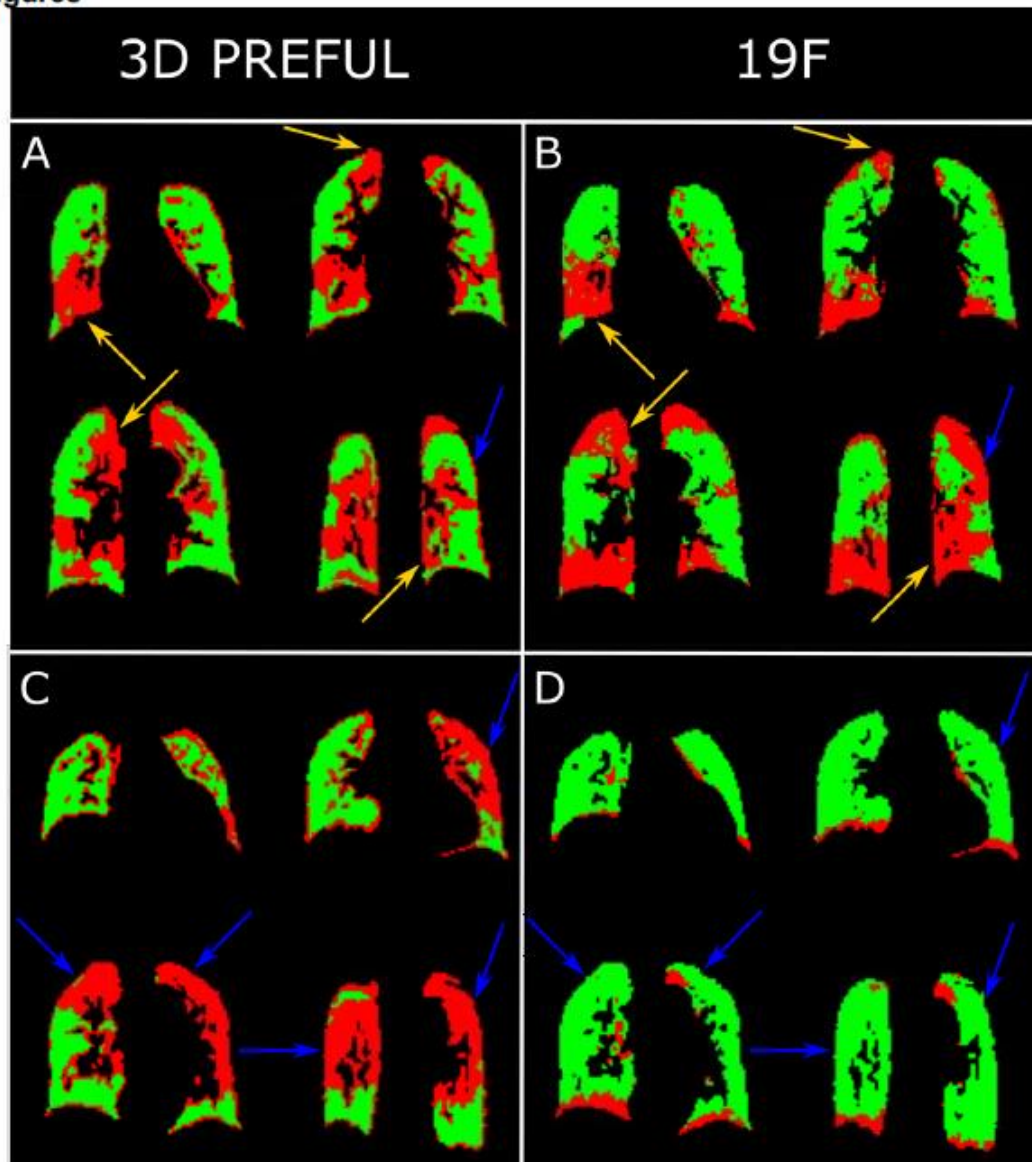
Figures


Figure 1. Regional comparison of 3D PREFUL VDP_{RVent} map (on the left) and ^{19}F derived VDP_{TTF} (on the right). Defect regions are color-coded in red. Gold arrows point out the regional agreement and blue arrows point out regional differences in VDP maps. In (A) and (B), a comparison for a 60-year old COPD male (FEV_1 % pred. = 53) with Sørensen-Dice coefficient of 54.7% and 61.5% in defect and healthy areas, is depicted, which results in total spatial overlap of 58.4%. In (C) and (D) an example of discrepancy of both methods is observed for a 71-year old COPD female (FEV_1 % pred. = 90) with Sørensen-Dice coefficient of 18.5% and 57.2% in defect and healthy areas, which results in total spatial overlap of 44.4%.

Abstract No. 808

Linear deformations of the 3D alveolar shape

Alex Reimelt^{1,*}, Dragos Vasilescu², Richard Beare^{3,4}, Jonas Labode⁵, Lars Knudsen⁶, and Roman Grothausmann⁷

¹Institute for Functional and Applied Anatomy, Hannover Medical School

²Department of Pathology and Laboratory Medicine, University of British Columbia, Vancouver, Canada

³Academic Unit, Medicine, Peninsula Clinical School, MONASH University, Melbourne, Australia

⁴Developmental Imaging, Murdoch Children's Research Institute, Melbourne, Australia

⁵Medizinische Hochschule Hannover

⁶Functional and Applied Anatomy

⁷Faculty of Engineering and Health, HAWK University of Applied Sciences and Arts, Göttingen, Germany

*Presenting author

Introduction

In several pathologic conditions external forces act on lung parenchyma. Linear deformations are likely to have an impact on alveolar microarchitecture and micromechanics. In a setting of a tension pneumothorax, a mediastinal shift induces an approximately linear compression of the non-collapsed lung while a resection of a lung lobe leads to a compensatory linear elongation of the remaining lung tissue. Severe shape deformations with altered tensile properties of lung tissue are also considered to play a role in the progression of lung fibrosis and therefore changed tensile properties of alveolar tissue are an essential part of the understanding of mechanisms leading to fibrosis. In this study we aimed to simulate the impact of forces which result on linear deformation of lung parenchyma on alveolar morphometrics.

Materials & Methods

We applied a segmentation algorithm for human microCT lung data (11m/voxel, six cubic datasets from each right lung lobe of two persons containing ca. 4000 alveoli each) where alveolar morphometrics were performed based on 3D alveolar models which enables the determination of the following parameters: alveolar volume, surface area, similarity to an ellipsoid, number of planar surface parts and angles between their normals (interplanar angles, see the violinplots). Using these alveolar models, linear elongation and compression was achieved by multiplying the voxel edge length within the existing models along one dimension with the factors 2 and 0.5. The MannWhitneyU test was used to compare nondeformed with deformed data.

Results

During elongation, the mean surface size was 166-171% (69-71% during compression) of the original values while the mean number of planar surface parts was 80-84% (64-70% during linear compression). The median interplanar angles ranged from 66 to 69° being 98-106% compared to the native data (103-113% during linear compression) depending on the degree of deformation. The ratio of alveolar entrance size to surface size was 73-78% (68-71% during compression). Changes between non-deformed and deformed data were significant ($p < 0.001$).

Conclusion

The simulations demonstrated that alveolar shape parameters systematically change when linear elongation and compression are applied. Further, linear shape deformations result in a smaller number of planar surface parts as surface parts with similar orientations fuse together, thus shifting the interplanar angle distribution to higher values. Taken together, these data show that macroscopic shape deformations of lung tissue also entail

morphological changes at the microscopic level.

Vasilescu, Drago M., et al. "Comprehensive stereological assessment of the human lung using multiresolution computed tomography." Journal of Applied Physiology 128.6 (2020): 1604-1616.

Grothausmann, Roman, et al. "Shape and Facet Analyses of Alveolar Airspaces of the Lung." International Workshop on Shape in Medical Imaging. Springer, Cham, 2018.

Abstract No. 809

Evaluation of 3-timepoint quantitative ^3He ventilation change maps with radiologist review

Ummul Afia Shammi^{1,}, Talissa Altes¹, John Mugler III^{2,2}, Eduard E de Lange², Jaime Mataz and Robert Thomen^{1,1}*

¹University of Missouri, Columbia, MO, USA

²University of Virginia, Charlottesville, Virginia, USA

*Presenting author

Background

Hyperpolarized gas (HPG) MRI has the potential of producing high-quality images of lung ventilation. Regions of low signal in HPG images are often quantified as a whole-lung ventilation defect percentage (VDP). While VDP is sensitive to measure lung-treatment efficacy, it lacks regional ventilation information inherent in images. There is a need to quantify regional ventilation changes analogous to visual inspection which may be useful for assessing regional treatment response or disease progression [1]. Here, we present an algorithm for calculating maps of changes in regional ventilation in asthma patients before and after albuterol-treatment. We validate the results with a radiologist evaluation for accuracy. Our hypothesis is that, change map would be in-congruence with radiologist's visual examination.

Methods

Nine asthma-patients (4M/5F, age= 24.5±5.9, FEV1pp at baseline= 69±19.23) were enrolled in an IRB-approved study. All subjects underwent HP ^3He imaging at three-different timepoints of each day: baseline, then again at 1-hour and 5-hours following albuterol. HPG MRI consisted of a 2D-Flash scan (TR/TE=7/2.7ms, matrix=256×256, FA=9°, voxel size= 1.64×1.64×10mm³, pixel bandwidth= 200). N4ITK bias-correction and voxel-smoothing were performed on images, which were normalized to the signal-distribution's 95th percentile voxel signal value. For calculating regional ventilation change maps, post-treatment images were registered to baseline. The difference in the voxel-signal intensity was calculated for baseline to 1-hour, baseline to 5-hours and 1-hour to 5-hours. Difference-map voxel values of >60% of the baseline mean-signal value were identified as-improved and those of <-60% were identified as-worsened (green and red respectively in Fig.1). In addition, short-term improvement (STI) was identified in which voxels improved at 1-hour but returned to normal at 5-hours (blue region) [2]. The total change in the lung volume were expressed as percentage of whole-lung volume: regional percent change (RPC). A grading rubric was developed for radiologist scoring that had the following assessment category: "level of volume-discrepancy" and "discrepancy causes" for each ventilation change map.

Results

The average improvement, STI, and worsening in RPC of the lung for nine asthmatics after inhaling albuterol was 7.72±7.54, 0.98±1.67, 1.18±0.90 respectively. According to the radiologist score, among the 9 cases, volume-discrepancies in the change map were small. Two cases were found to have moderate and large volume discrepancy. The under-detection of improved, worsened and STI region was considered to be very-small to small. The summary of radiologist score is given in Table 1. The specific case with a large volumediscrepancy

was a subject who had many defects that improved/resolved 1-hour following albuterol but recurred at 5-hours. The change map detected the improvement successfully but failed to detect the recurrence (Fig. 1). Coil-sensitivity may have contributed to the discrepancy since the radiologist assessed images without bias-correction.

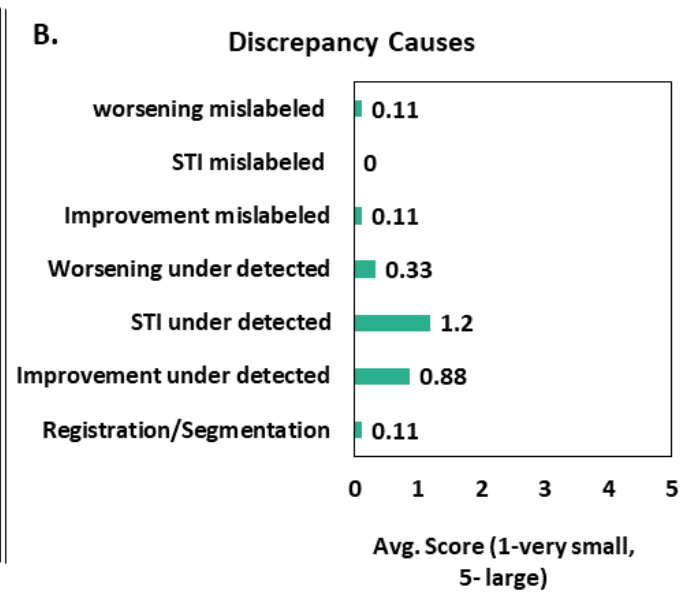
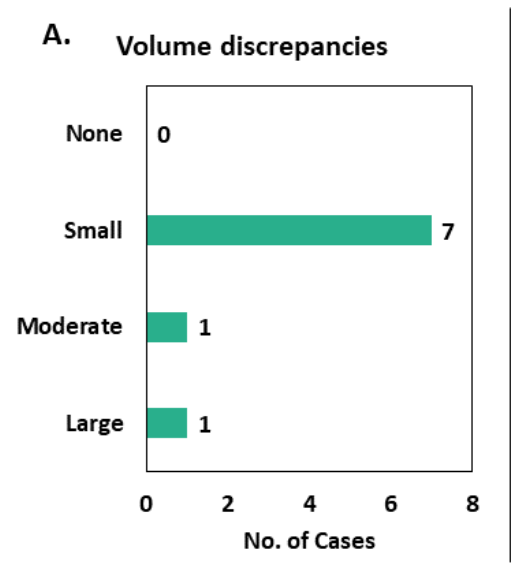
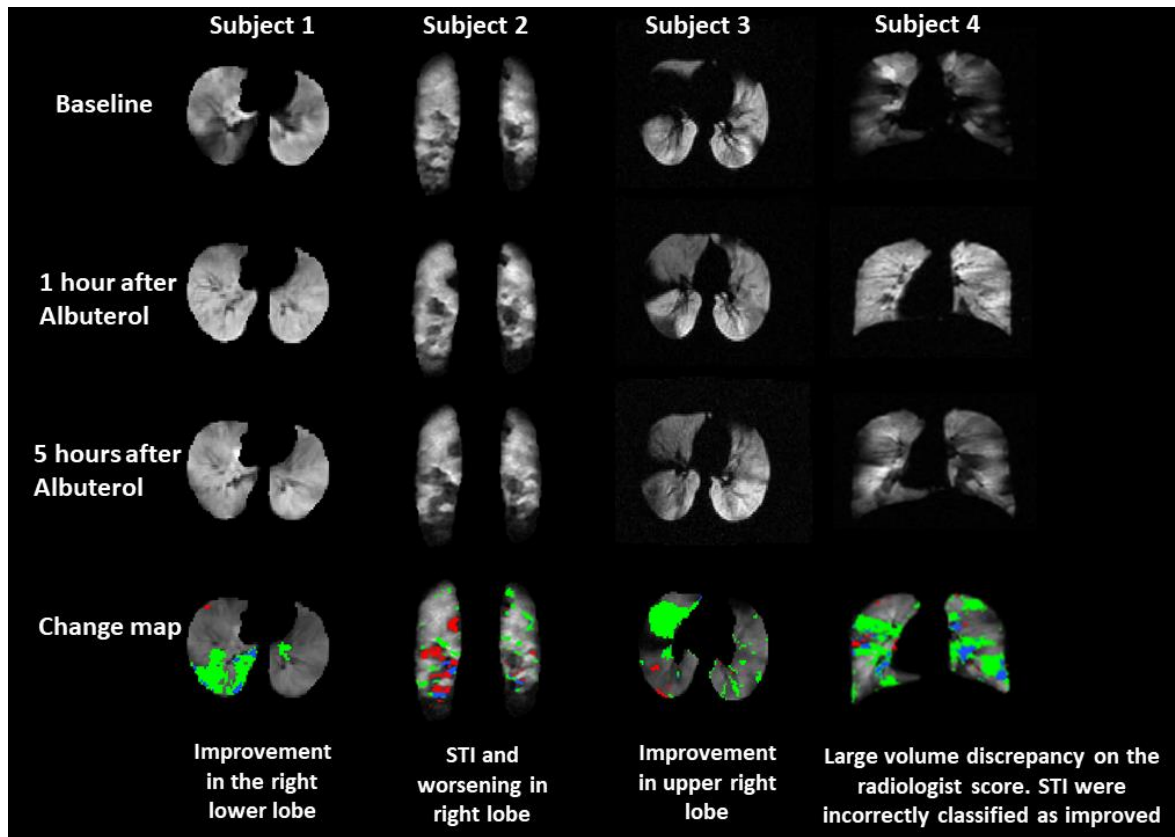
Discussion

Our regional change maps demonstrated congruence with visual examination and may be a useful tool for clinicians evaluating ventilation changes longitudinally. To our knowledge, this

is the first time, regional ventilation change map of HPG MRI has been scored by an expert and exhibited good agreement. In future, we plan to apply this algorithm to other lung diseases.

1. Horn FC et al. *Regional Ventilation Changes in the Lung: Treatment Response Mapping by Using Hyperpolarized Gas MR Imaging as a Quantitative Biomarker. Radiology. 2017 Sep;284(3):854-861. doi: 10.1148/radiol.2017160532. Epub 2017 May 4. PMID: 28471738*

2. Shammi UA et al. *Quantifying regional pulmonary ventilation changes in hyperpolarized 3He MRI of asthma subjects following bronchodilator at three timepoints. The International Society for Magnetic Resonance in Medicine Annual Meeting 2022*



Abstract No. 810

Local Comparison of T₁(TE) and Quantitative Perfusion in Patients with COPD

Simon Triphan^{1,2,}, Marilisa Konietzke^{3,1}, Claus Heußel^{4,2}, Jürgen Biederer^{1,2}, Hans-Ulrich Kauczor^{1,2}, and Mark Wielpütz^{1,2}*

¹University Hospital Heidelberg

²Translational Lung Research Center (TLRC), Member of the German Center of Lung Research (DZL)

³Boehringer Ingelheim Pharma GmbH & Co. KG

⁴Thoraxklinik at University of Heidelberg

*Presenting author

Introduction

TE-dependent observed T₁ (T₁(TE)) mapping has shown potential for functional lung imaging: Correlations between T₁(TE) and reader scores based on dynamic contrast-enhanced

(DCE) perfusion MR images have been shown. However, these are based on T₁(TE) measured in 1-2 slices in comparison to 3D images of the entire lungs, while scores have both low numerical resolution and are only global measures. DCE MRI also allows for quantitative approaches that can provide local pulmonary blood flow (PBF) maps as well as a local classification of healthy and defective tissue. Thus, the purpose of this work was to use these data to examine this connection locally.

Methods

22 patients with COPD (aged 68±7 years) were examined using an MRI protocol including 3D DCE MRI and T₁(TE) mapping using an inversion recovery multi-echo 2D ultra-short TE (UTE) sequence at 5 different TE (70µs to 2300µs) in 1-2 slices per patient. The DCE images were acquired in inspiratory breath-holds with higher in-plane resolution and thinner slices compared to UTE images, which were acquired during free breathing and gated using 50% of data. T₁ maps were calculated at each TE from the UTE images. Lungs were segmented independently for DCE and UTE images. PBF and defect classification maps were calculated from DCE images and registered onto UTE images using ANTs. Additionally, both segmentations were divided into areas of equal volume. Correlations were calculated per voxel from registered images and using means in equivalent segmented areas.

Results

An example of the image registration and parameter maps is shown in the Figure. Visually, good agreements were found in patients with notable remaining areas of healthy lung.

Voxelwise

Spearman's correlations based on registered images between 0.24 and 0.66 were found at TE₁=70s as well as 0.16 to 0.65 at TE₂=500s with overall lower correlations at later TEs: The average of these intra-patient correlations was 0.44 and 0.39, respectively.

Correlations based on segmented areas were stronger in some patients and weaker in others, but on average similar with 0.44 and 0.35, respectively. Considering median values over entire slices, the inter-patient correlations of PBF and T₁ was 0.56 at TE₁ and 0.64 at TE₂, while the correlation between the defect percentage QDP and T₁ was -0.56 and -0.76, respectively. In 18 patients, T₁(TE₁) in defect areas according defect classification maps was significantly shorter than in the remaining lung.

Conclusion

The intra-patient correlations found reached from very weak to moderately strong, resulting in only moderate average correlation. That neither registration nor segmented areas yields consistently stronger correlations might imply that a more accurate mapping is possible. Here, stronger inter-patient correlations of T₁ with quantitative perfusion were found at medium TE compared to UTE, which agrees well with those previously found using reader

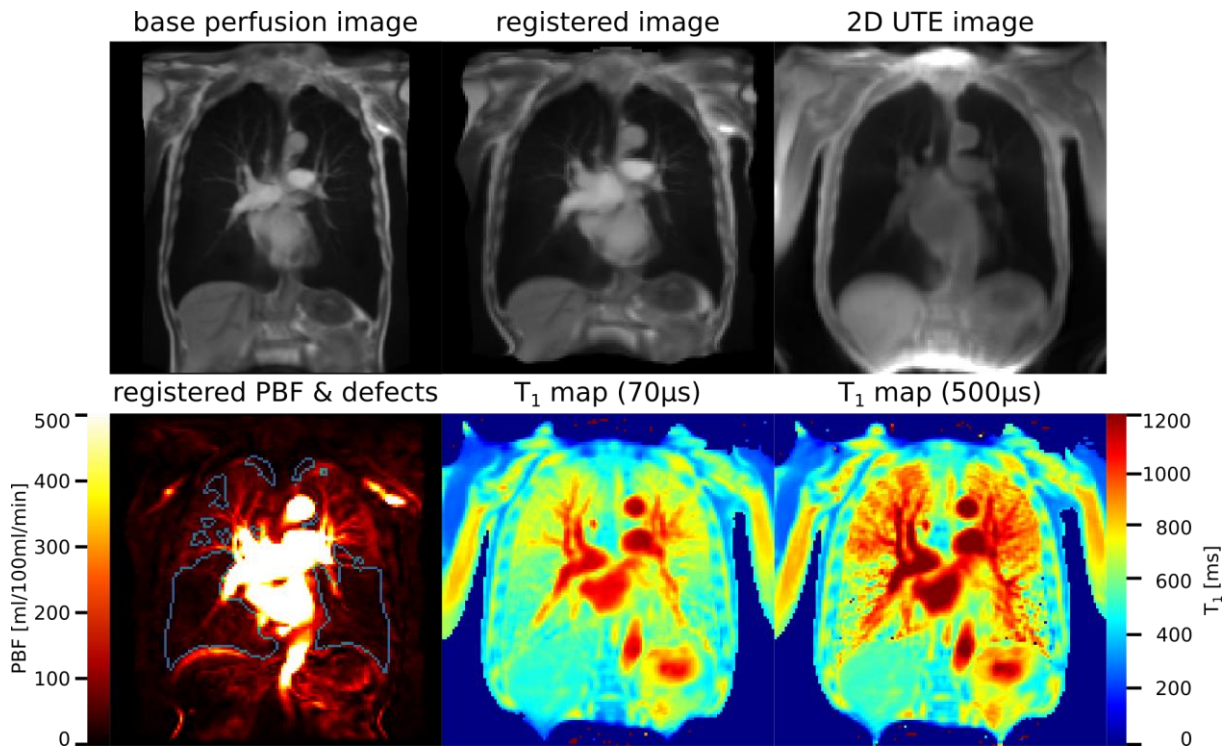
scores, but not with the intra-patient correlations, which were strongest at UTE. Further, the visual impression of maps like the example shown here implies that high correlations are found in patients who have remaining healthy lung areas in the slices covered by UTE.

Triphan, S. M.; Jobst, B. J.; Breuer, F. A.; Wielpütz, M. O.; Kauczor, H.-U.; Biederer, J. & Jakob, P. M., (2015), Echo time dependence of observed T1 in the human lung, JMRI, 42, <https://doi.org/10.1002/jmri.24840>

Triphan, S.M.F. et al, (2021), Echo Time-Dependent Observed Lung T1 in Patients With Chronic Obstructive Pulmonary Disease in Correlation With Quantitative Imaging and Clinical Indices, JMRI, <https://doi.org/10.1002/jmri.27746>

Schiwek, M., Triphan, S.M.F., Biederer, J. et al. , (2022), Quantification of pulmonary perfusion abnormalities using DCE-MRI in COPD: comparison with quantitative CT and pulmonary function, European Radiology, <https://doi.org/10.1007/s00330-021-08229-6>

Avants, Brian B., Nick Tustison, and Gang Song. "Advanced normalization tools (ANTs)." Insight j 2.365 (2009): 1-35.



Abstract No. 811

CNN detects Partial Volume Artifacts on 2D MR-Images of the Lung for Automated Quality Control

Andreas Voskrebenzev^{1, 2, *}, Cristian Crisosto^{1, 2}, Maximilian Zubke^{1, 2}, Frank Wacker^{1, 2}, and Jens Vogel-Claussen^{1, 2}

¹Institute for Diagnostic and Interventional Radiology

²Biomedical Research in Endstage and Obstructive Lung Disease Hannover (BREATH)

*Presenting author

Introduction: The partial volume effect (PVE) is a well-known artifact in MR imaging. One application case, where especial consideration of the PVE is required, is phase-resolved functional lung imaging (PREFUL₁). This method is based on the 2D acquisition of coronal image-time-series to assess ventilation and perfusion dynamics. Since the whole PREFUL analysis relies on accurate voxel time-series originating from lung parenchyma, PVE can result in compromised results. Therefore, it is desirable to find an automated method, which can identify such slices. The hypothesis of this study is that a convolutional neural network (cnn) can be used to detect images containing strong PVE artifacts with at least 90% accuracy.

Methods: Seven healthy volunteers and 34 patients with suspicion of chronic thromboembolic pulmonary hypertension underwent 1.5T MRI. For PREFUL MRI, multiple coronal slices with a slice gap of 20% were acquired (see Figure 1) in free breathing using a 2D spoiled gradient sequence². After a non-rigid registration, the image time-series was averaged in the temporal dimension and preprocessed as follows:

1. Cut to center (exclude 20 voxels from each edge)
2. Resize image to input size of 299 x 299
3. replicating the image to 299 x 299 x 3 (account for pretraining on RGB images)
4. Normalize the value range by maximal value

The pretrained Inception-v3 architecture was adapted for two classes. Data (n=294) was labeled by a MR-physicist and randomly split according to a 60% training (n=176), 20% validation (n=59) and 20% test (n=59) scheme. Due to a high class-imbalance, the sets were over-sampled by duplicating randomly selected images to establish an even class distribution³. Image augmentation with random shearing, translation, scaling and rotation operators was performed to prevent the net from over-fitting. Image augmentation was also applied for the over-sampled data to introduce some variation between the duplicated images.

The classification accuracy was calculated for the original test data and for the over-sampled test data. To reduce random bias introduced by oversampling selection, the oversampling was repeated 100 times to obtain an averaged accuracy.

Results: Transfer learning was completed after ~7 minutes (NVIDIA Titan V) and converged to a validation accuracy of 98%. An accuracy of 95% was achieved for the test data without oversampling. For over-sampled data, an average accuracy of 91% (=0.03) was obtained. See Figure 2 for the visual presentation of the cases, which were falsely classified.

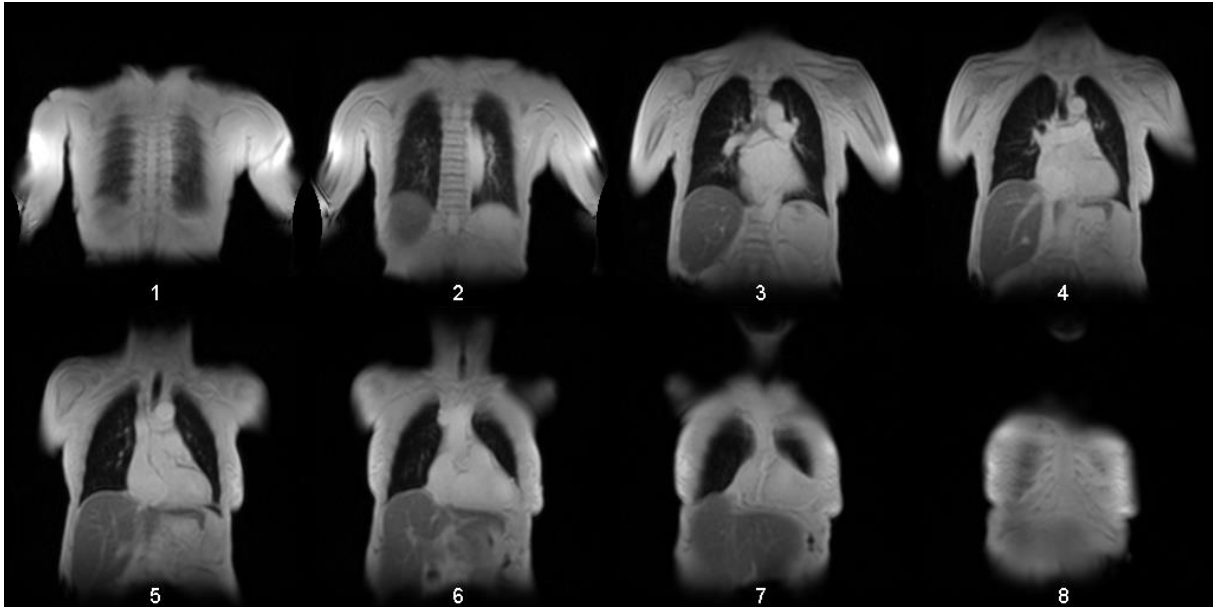
Discussion: As hypothesized, an accuracy over 90% was achieved. The falsely classified cases are all located in the more anterior and posterior sections of the lung and thus contain at least some proportion of voxels with PVE. Therefore, the classification of such slices is not unambiguous and can probably vary from observer to observer. Analysis of the activation in the convolutional layers suggests, that the net actually learned to identify ribs structures. One drawback of this study is that classification was only performed by one observer for single-center data.

Conclusion: This study demonstrates, that CNNs can be employed for automated quality management by excluding slices, which show PVE.

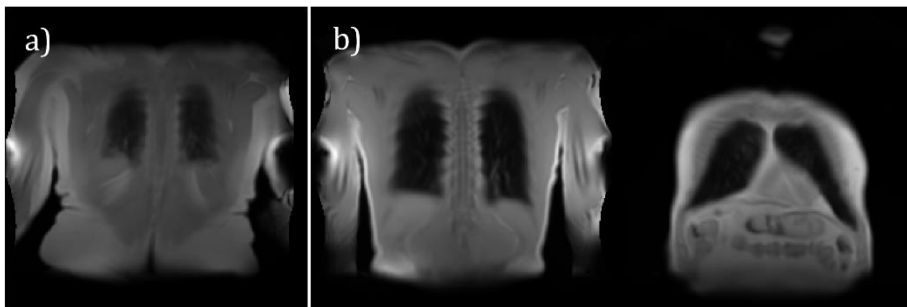
[1] Voskresbenzev A, et al. Feasibility of quantitative regional ventilation and perfusion mapping with phaseresolved functional lung (PREFUL) MRI in healthy volunteers and COPD, CTEPH, and CF patients. *Magn Reson Med.* 2018;79(4):2306-2314.

[2] Lasch F et al. Comparison of MRI and VQ-SPECT as a Screening Test for Patients With Suspected CTEPH: CHANGE-MRI Study Design and Rationale. *Front Cardiovasc Med.* 2020;7:51. doi:10.3389/fcvm.2020.00051

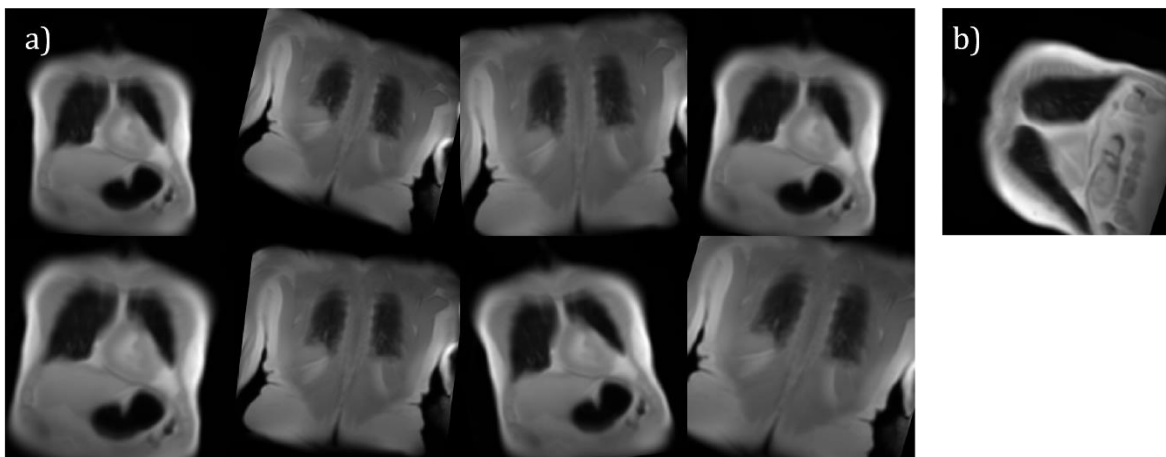
[3] Kenta (2022). Oversampling for deep learning: classification example (<https://github.com/Kentaltakura/Imageclassification-using-oversampling-imagedatastore/releases/tag/2.0>), GitHub.



I Original Test Data



II Oversampled and augmented Test Data



Abstract No. 812

Improving CT numbers in thoracic imaging by using a simultaneously scanned miniphantom

Oliver Weinheimer^{1, 2, *}, Lena Wucherpfennig^{1, 2}, H. Henry Guo³, Katie J. Bayfield⁴, Hans-Ulrich Kauczor^{1, 2}, Claus Peter Heussels^{5, 2}, Craig J. Galbán⁶, Terry E. Robinson⁷, Brian J. Bartholmai⁸, Paul D. Robinson⁴, and Mark O. Wielpütz^{1, 2}

¹University Hospital of Heidelberg

²Translational Lung Research Center (TLRC), a member of the German Center for Lung Research (DZL), Heidelberg, Germany

³Stanford Medical Center

⁴The Children's Hospital at Westmead

⁵Thoraxklinik at University of Heidelberg

⁶University of Michigan

⁷Stanford University

⁸Mayo Clinic, Rochester

*Presenting author

Purpose: Quantitative CT (QCT) of chronic obstructive pulmonary diseases is becoming an increasingly recognized and viable approach for the evaluation of the severity of lung manifestations [1]. Various quantitative evaluation techniques of CT images have been proven to deliver useful and objective biomarkers describing lung parenchyma and airways [2,3]. The CT number accuracy plays an important role in QCT. We propose CT number improvement by means of a mini-phantom [4], which can be carried with each examination without further falsification of the CT images.

Methods and Materials: In a single-center study paired inspiratory-expiratory chest CT scans were performed twice (spirometry-directed) at The Children's Hospital at Westmead on 14 subjects with cystic fibrosis lung disease, once with a low dose (LD, ~ CTDI_{vol} 1.17±0.42 mGy) and once with an ultra-low dose (ULD, ~ CTDI_{vol} 0.21±0.04 mGy) CT protocol. The mini-phantom was placed on the middle of the patient's chest and was analyzed fully automated. CT number adjustment was done by using CT number deviations from the miniphantom

and from extra-corporal and tracheal air nominal numbers. The CT number adjustment is spatially weighted by means of a body distance map, the work-flow is depicted in Figure 1. CT number differences in original CT and HU adjusted CT were compared.

Results: HU deviation from nominal HU in extra-corporal air was reduced by 6.4±6.9 HU (LD: 4.4±5.2 HU, ULD: 8.3±8.0 HU). For tracheal air HU the deviation reduction was 21.4±9.9 HU (LD: 17.0±8.6 HU, ULD: 25.8±9.2 HU), see Figure 2. The mean lung density (MLD) was reduced by 6.5±17.8 HU (LD: 1.2±18.2 HU, ULD: 12.0±15.8 HU), MLD differences between LD and ULD were slightly reduced by 0.1 HU.

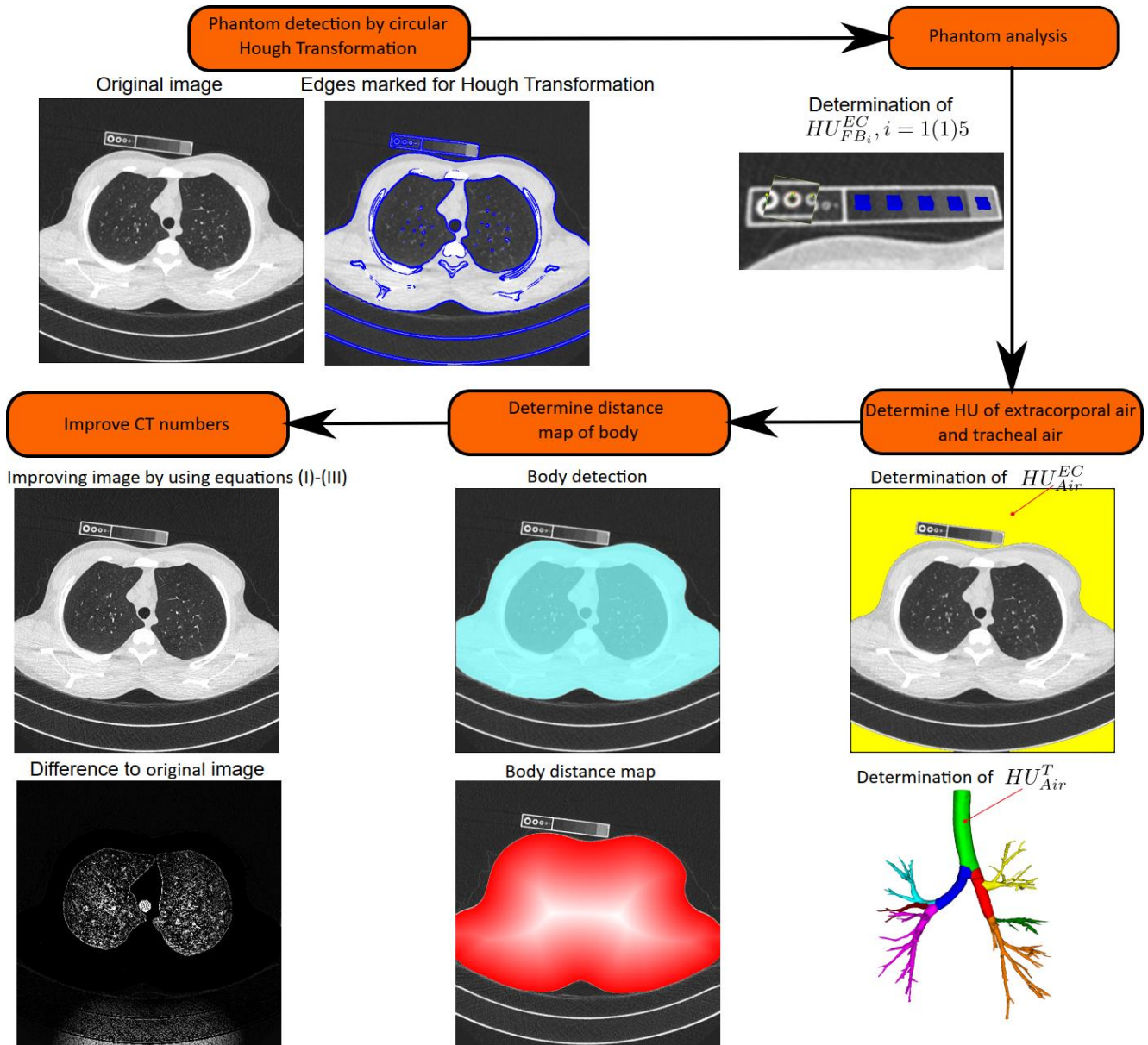
Conclusion: This initial study shows that the mini-phantom can help to improve the accuracy and to reduce dose-dependent shifts in CT numbers, and thus improve accuracy of densitometry and comparability between scanners and scan protocols. If dose is further reduced in the future, differences may be compensated. It is shown that CT numbers in extracorporeal and tracheal air are pushed closer to the desired -1000 HU, but further investigations focused on the whole CT number range are needed.

[1] Herth FJF, Kirby M, Sieren J, Herth J, Schirm J, Wood S, Schuhmann M. *The Modern Art of Reading Computed Tomography Images of the Lungs: Quantitative CT. Respiration. 2018;95(1):8-17. doi: 10.1159/000480435. Epub 2017 Sep 16. PMID: 28918422.*

[2] Bertram J. Jobst and Oliver Weinheimer et al. *Longitudinal airway remodeling in active and past smokers in a lung cancer screening population. European Radiology, Dec 2018.*

[3] Galbán, Craig J. et al.(2012): *Computed tomography-based biomarker provides unique signature for diagnosis of COPD phenotypes and disease progression. In Nature medicine 18 (11), pp. 1711–1715. DOI: 10.1038/nm.2971.*

[4] H. Henry Guo, Mats Persson, Oliver Weinheimer, Jarrett Rosenberg, Terry E. Robinson, and Jia Wang. A calibration ct mini-lung-phantom created by 3-d printing and subtractive manufacturing. *Journal of Applied Clinical Medical Physics*, May 2021.



Equations for CT number improvement

(I) Nominal values

$$\begin{aligned} \overline{HU}_{Air} &= -1000.0 \text{ HU} \\ \overline{HU}_{FB_1} &= -897.0 \text{ HU} \\ \overline{HU}_{FB_2} &= -844.1 \text{ HU} \\ \overline{HU}_{FB_3} &= -774.1 \text{ HU} \\ \overline{HU}_{FB_4} &= -695.3 \text{ HU} \\ \overline{HU}_{FB_5} &= -351.0 \text{ HU} \end{aligned}$$

(II) HU prediction functions

$$HU_{Air}^d = HU_{Air}^{EC} + \frac{e^{\left(\frac{c}{d_T} - 1\right)}}{(e^c - 1)} (HU_{Air}^T - HU_{Air}^{EC}),$$

d given by body distance map, $d=0$ outside body, $c=3.5$

$$HU_{FB_i}^d = HU_{FB_i}^{EC} + \frac{e^{\left(\frac{c}{d_T} - 1\right)}}{(e^c - 1)} (HU_{Air}^T - HU_{Air}^{EC}) \sigma_{FB_i}, \quad i = 1(1)5$$

where $\sigma_{FB_i} = \frac{HU_{FB_i}^{EC} - \overline{HU}_{FB_i}}{HU_{Air}^{EC} - \overline{HU}_{Air}}, \quad i = 1(1)5$

(III) Improving HU values

$$f(x, d) = \begin{cases} x - (1 - \omega_i) (HU_{FB_{i-1}}^d - \overline{HU}_{FB_{i-1}}) - \omega_i (HU_{FB_i}^d - \overline{HU}_{FB_i}), & \text{for } HU_{FB_{i-1}}^d \leq x \leq HU_{FB_i}^d, i = 2(1)5 \\ x - (1 - \omega_1) (HU_{Air}^d - \overline{HU}_{Air}) - \omega_1 (HU_{FB_1}^d - \overline{HU}_{FB_1}), & \text{for } HU_{Air}^d \leq x \leq HU_{FB_1}^d \\ x - (HU_{Air}^d - \overline{HU}_{Air}), & \text{for } x < HU_{Air}^d \end{cases}$$

with $\omega_1 = (x - HU_{Air}^d) / (HU_{FB_1}^d - HU_{Air}^d)$

$$\omega_i = (x - HU_{FB_{i-1}}^d) / (HU_{FB_i}^d - HU_{FB_{i-1}}^d), \quad \text{for } i = 2(1)5$$

Figure 1: Workflow for CT number improvement

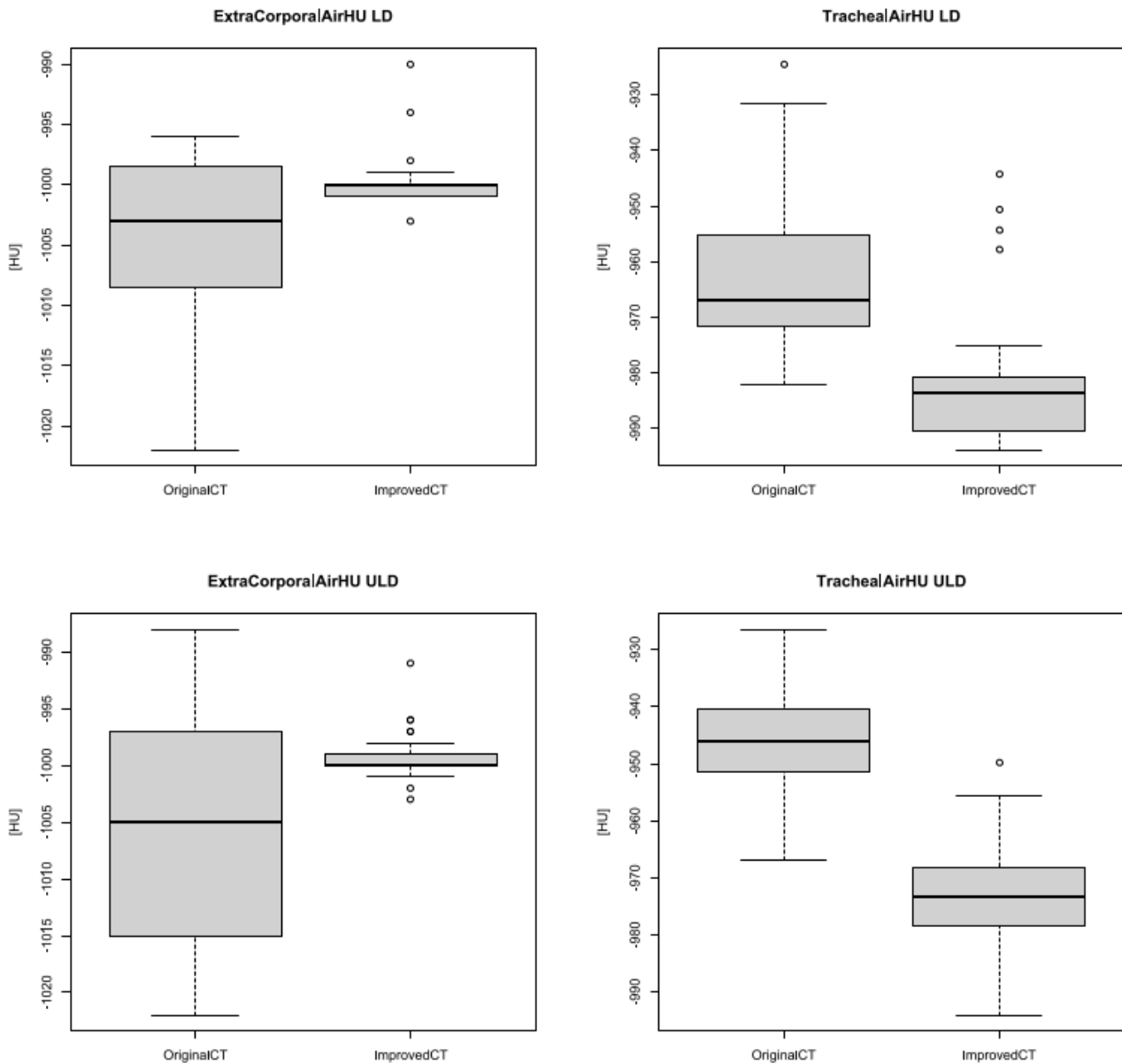


Figure 2: Boxplots showing the influence of the CT number improvement on parameters ExtracoporalAirHU and TrachealAirHU. Both parameters are pushed closer to the desired -1000 HU.

Abstract No. 813

INFLUENCE OF LUNG VESSEL SEGMENTATION ON THE REPRODUCIBILITY OF PREFUL MRI

Marius Wernz^{1,2,*}, Maximilian Zubke^{1,2}, Andreas Voskrebenezv^{1,2}, Robin Müller^{1,2}, Filip Klimeš^{3,4}, Bernd Schweizers⁵, Frank Wacker^{1,2}, and Jens Vogel-Claussen^{1,2}

¹Institute for Diagnostic and Interventional Radiology

²Biomedical Research in Endstage and Obstructive Lung Disease Hannover (BREATH)

³Hannover Medical School, Hannover

⁴Biomedical Research in Endstage and Obstructive Lung Disease (BREATH), German Center for Lung Research

⁵RheinMain University of Applied Sciences Rüsselsheim

*Presenting author

Introduction

Phase-resolved functional lung (PREFUL) MRI allows for the voxel-wise calculation of ventilation and perfusion parameters within the lung parenchyma [1]. For the functional analysis, segmentation of lung parenchyma including lung vessel recognition is necessary. For current image-based algorithms, lung vessel exclusion is challenging due to its anatomical complexity and signal intensity variations. Thus in this work, an automated deep learning method to exclude voxels containing large vessels was developed and compared to traditional threshold-based lung vessel segmentation technique regarding the reproducibility of functional parameters derived by PREFUL.

Methods

A convolutional neural network (CNN) in U-Net architecture [2] and a thresholding method based on Otsu's method [3] were implemented into the 2D PREFUL MRI algorithm to detect and exclude large pulmonary vessels from perfusion and ventilation analysis (figure 1). The CNN was trained on 257 coronal proton MR images and corresponding manual ground-truth segmentation maps. 28 chronic obstructive pulmonary disease (COPD) patients underwent PREFUL MRI and spirometry at a baseline point and after two weeks of placebo treatment as part of the CLAIM study [4]. The PREFUL analysis was conducted using both lung vessel segmentation methods and without any lung vessel exclusion. The resulting ventilation and perfusion parameters were tested for difference using Wilcoxon signed rank test, compared regarding their reproducibility using intraclass correlation coefficient (ICC) and correlation to spirometry using Pearson correlation analysis.

Results

All calculated parameters differed significantly depending on the method of vessel segmentation (all $p < 0.05$) as indicated in table 1. ICC was higher for ventilation parameters using the CNN segmentation or Otsu's method compared to no vessel segmentation (Regional ventilation (RV): 0.67, 0.67, 0.64; Flow-volume loop correlation metric (FVL-CM): 0.92, 0.9, 0.83). Ventilation defect percentages (VDP) achieved highest ICC using the CNN (VDPRV: 0.86, 0.85, 0.79; VDPFVL-CM: 0.86, 0.81, 0.74). For perfusion defect percentage (QDP) ICC was comparable between all three segmentation methods (QDP: 0.8, 0.82, 0.8). Pearson correlation to spirometry (FEV1/FVC) was calculated for all ventilation parameters, showing similar correlations for RV (0.48, 0.47, 0.47) and for VDPRV (-0.76, -0.77, -0.74) regarding all three segmentation methods. For FVL-CM and VDPFVL-CM, correlation was best using the CNN (FVL-CM: 0.67, 0.65, 0.65; VDPFVL-CM: -0.81, -0.74, -0.71).

Discussion & Conclusions

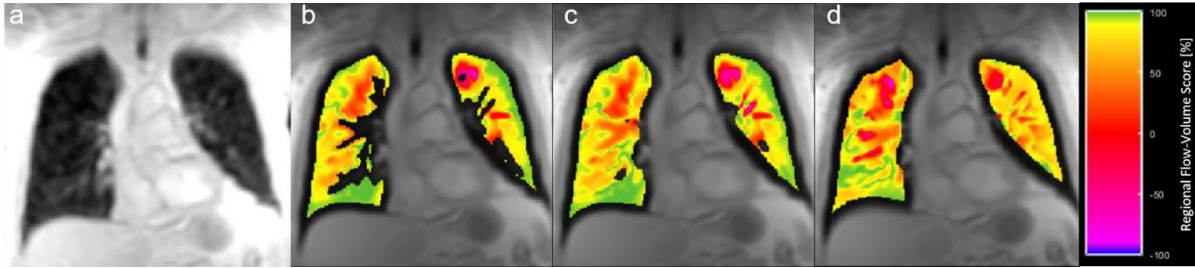
Vessel segmentation significantly influences the values and reproducibility of PREFUL parameters. For ventilation analysis, the CNN-based segmentation improved reproducibility while maintaining correlation to spirometry. Significantly lower VDP values are likely due to the exclusion of vessel regions from the analysis; higher QDP values also correspond to the exclusion of highly perfused areas in the central vasculature.

[1]: Voskresbenzev A et al. Feasibility of quantitative regional ventilation and perfusion mapping with phaseresolved functional lung (PREFUL) MRI in healthy volunteers and COPD, CTEPH, and CF patients. *Magn Reson Med.* 2018

[2]: Olaf Ronneberger et al. U-net: Convolutional networks for biomedical image segmentation. *International Conference on Medical image computing and computer-assisted intervention.* 2015

[3]: Nobuyuki Otsu. A threshold selection method from gray-level histograms. *IEEE transactions on systems, man, and cybernetics* 9.1. 1979

[4]: Jens Hohlfeld et al. Effect of lung deflation with indacaterol plus glycopyrronium on ventricular filling in patients with hyperinflation and COPD (CLAIM). *Lancet Respir Med.* 2018



	CNN		Otsu		None	
	Median	0.25; 0.75	Median	0.25; 0.75	Median	0.25; 0.75
RV	0.117	0.083; 0.138	0.114	0.082; 0.134	0.107	0.075; 0.125
VDP_{RV}	0.321	0.223; 0.387	0.338	0.262; 0.388	0.355	0.298; 0.482
FVL-CM	0.925	0.884; 0.943	0.909	0.869; 0.934	0.898	0.838; 0.929
VDP_{FVL-CM}	0.482	0.426; 0.61	0.516	0.459; 0.623	0.553	0.486; 0.666
QDP	0.454	0.339; 0.557	0.402	0.291; 0.501	0.413	0.285; 0.516

Abstract No. 814

IMPACT OF DEEP LEARNING BASED MR-RECONSTRUCTION ON VENTILATION ASSESSMENT OF POST-COVID-19 PATIENTS

Maximilian Zubke^{1,2,*}, Filip Klimes^{1,2}, Andreas Voskrebenezv^{1,2}, Till Kaireit^{1,2}, Agilo L. Kern^{1,2}, Marcel Gutberlet^{1,2}, Robin Müller^{1,2}, Frank Wacker^{1,2}, and Jens Vogel-Claussen^{1,2}

¹Institute for Diagnostic and Interventional Radiology

²Biomedical Research in Endstage and Obstructive Lung Disease Hannover (BREATH)

*Presenting author

Introduction

3D phase-resolved functional lung (3D-PREFUL) proton MRI¹ enables ventilation assessment of human lungs without contrast agents and breathing commands. However, acquisition of high-quality MR-images usually requires a long scanning time from the patient. Acceleration can be achieved by k-space undersampling, but such techniques cause image artifacts, which hamper the ability to perform accurate ventilation assessment with the resulting image data. Recent literature has shown, that Deep learning (DL) - based approaches can outperform conventional methods such as compressed sensing in the reconstruction of undersampled and especially dynamic MR-data.^{2,3} Hence, it can be hypothesized that DL-based reconstruction methods enable 3D-PREFUL with undersampled MR-data (see Figure 1), which would result in a significant reduction in scanning time for patients.

Methods

3D-PREFUL-MR-data from 21 post-COVID-19 patients and 22 healthy volunteers consisting of 52-80 slices with 30-43 respiratory phases and matrix size of 128X128 have been organized as 3561 training and 1527 test image series containing 30 respiratory phases each. Since the original scans were acquired in fully sampled version only, they were undersampled artificially by removing random lines in cartesian k-space. Next, a convolutional recurrent neural network³ was trained to transform an aliased image sequence of 30 respiratory phases into the fully sampled reconstruction of 30 phases. Thereafter, 3D-PREFUL analysis was conducted with both versions per patient, the fully sampled version and the undersampled image data reconstructed by the deep neural network. Finally, the 3D-PREFUL parameters regional ventilation (RVent), which is calculated from inspiration and expiration phases, and cross correlation (CC), which value is derived from whole ventilation cycles, were compared using spearman correlation and tested for significant differences (paired t-test). The corresponding ventilation-defect-maps (VDP-maps) were compared using dice coefficient. To study the effect of different levels of undersampling, the aforementioned experiments were conducted with 2x, 4x and 8x undersampled data.

Results

Mean value of RVent was reproduced with a difference of 0.2% from 2x, 0.48% from 4x and 0.69% from 8x undersampled data in comparison to the fully sampled version. The mean value of CC was reproduced with a mean difference of 0.27%, 1.43% and 2.08%. Both parameters were calculated without a significant difference ($p > 0.9$) for the complete cohort on all three undersampling levels. For RVent, a significant correlation ($p < 0.001$) with $R_s = 0.99$ on all undersampling levels was measured. For CC, a decreasing correlation ($R_s = 0.99$ for 2x, $R_s = 0.93$ for 4x, $R_s = 0.85$ for 8x) with increasing undersampling level was observed. The subsequent calculation of VDP-values was reproduced with a mean difference of 0.6%, 4% and 7.2% for RVent and a difference of 0.6%, 3.5% and 5% for CC. The dice coefficient of both VDP-maps showed values of 0.9, 0.76 and 0.62.

Conclusions

In context of post-COVID-19 diagnostics, 3D-PREFUL ventilation assessment from

undersampled MR-data, reconstructed by a deep neural network, is feasible with non-significant differences in regional ventilation and cross correlation analysis. However, as shown in Figure 2a-b, correctness of VDP-maps decreases with increasing undersampling level. Hence, DL-based reconstruction of 2x undersampling is recommended to ensure precise ventilation measurement (see Figure 2c-d).

1. Klimeš, F., Voskrebenezv, A. et.al. 3D phaseresolved functional lung ventilation MR imaging in healthy volunteers and patients with chronic pulmonary disease. *Magnetic Resonance in Medicine*. 2021; 85(2), 912-925. doi: 10.1002/mrm.28482
2. Ramzi, Z., Ciuciu, P., & Starck, J. L. . Benchmarking MRI reconstruction neural networks on large public datasets. *Applied Sciences*. 2020; 10(5), 1816. doi: 10.3390/app10051816
3. Qin, C., Schlemper, J., Caballero, J., Price, A. N. et.al. Convolutional Recurrent Neural Networks for Dynamic MR Image Reconstruction. *IEEE Transactions on Medical Imaging*. 2018; 38(1), 280-290. doi: 10.1109/TMI.2018.2863670

Figures:

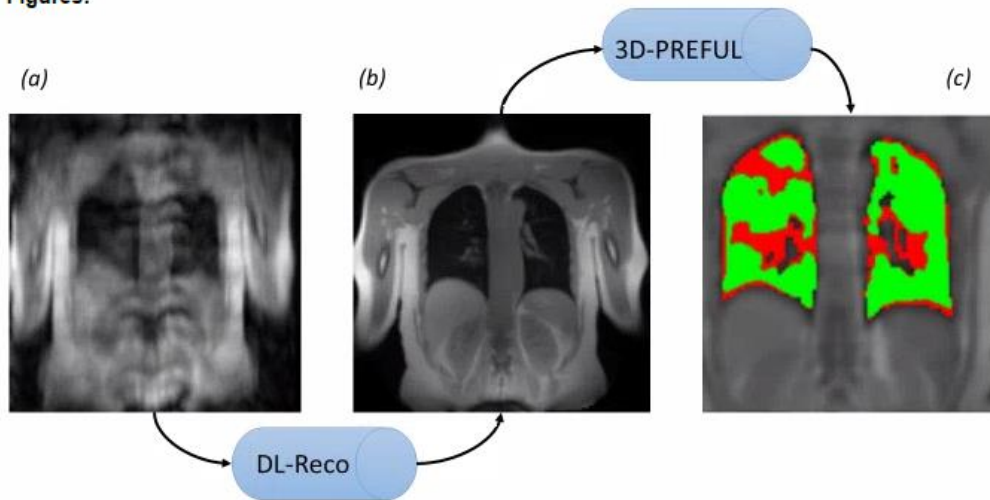


Figure 1: Deep Learning-based reconstruction (DL Reco) transforms zero-filled and thus aliased image (a) into improved image (b) which enables the identification of ventilation defects shown in (c).

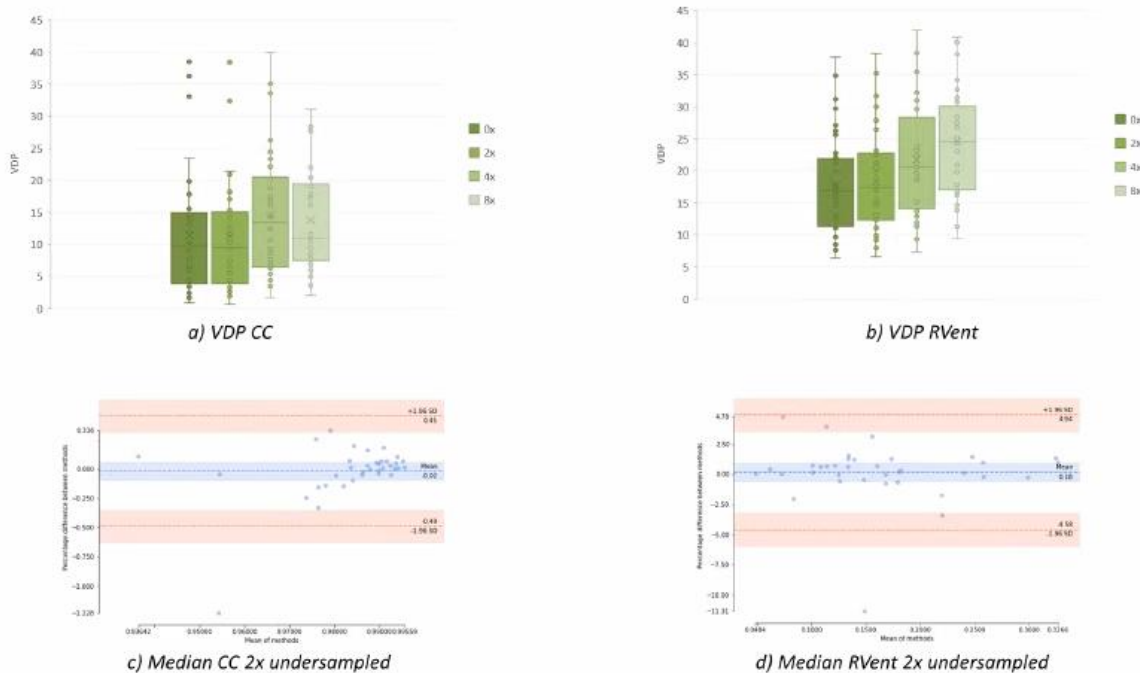


Figure 2: Effects of deep learning based reconstruction of undersampled data on CC and RVent. In (A) and (B) boxplots represent the VDP values derived by 3D PREFUL in all subjects from the original and three undersampled (2x, 4x, 8x) data. 2x undersampling recommended for acceleration of 3D-PREFUL. (C) and (D) show Bland-Altman analysis of CC and RVent ventilation parameters in comparison of ground truth and the recommended undersampling level. No significant bias was found in both comparisons (all $p > 0.9$).

Session: Other

Abstracts No. 900 – 903

Abstract No. 900

The potential of propagation based imaging for high resolution lung imaging in patients

Christian Dullin^{1, 2, *}, *Jonas Albers*³, *Angelika Svetlove*⁴, *Nicola Sodin*⁵, *Diego Dreossi*⁵, *Maria Cova*⁶, *Mario Confalonieri*⁶, *Frauke Alves*⁴, *Mascha Fiedler*¹, *Mark O. Wielpütz*¹, *Jürgen Biederer*¹, *Hans-Ulrich Kauczor*¹, *Giuliana Tromba*⁵, and *Willi Wagner*^{1, 2}

¹Heidelberg University Hospital, Heidelberg, Germany

²German Center for Lung Research (DZL), University Heidelberg

³European Molecular Biology Laboratory, Hamburg, Unit c/o DESY, Hamburg, Germany

⁴Max-Planck-Institute for Multidisciplinary Sciences, Goettingen, Germany

⁵Elettra Synchrotron Trieste, Italy

⁶University Hospital Cattinara, Trieste, Italy

*Presenting author

Introduction:

To aid in an early diagnosis and better understand the underlying pathomechanism in lung disease, pathological alterations of the lung need to be studied in detail. Computed tomography (CT) is typically applied to study the lung in-vivo in 3D. However, CT cannot be used to its full potential due to the known side effects. Novel phase sensitive x-ray imaging techniques show improved soft-tissue contrast especially in lungs. Among them propagation based imaging (PBI) is most dose effective. The application of PBI for lung imaging in patients is hampered since the incident x-ray beam needs to have a certain degree of coherence and high resolution detectors are needed to record interference effects. Thus, PBI is typically limited to lung imaging in small animals at synchrotrons.

Here we present our PBI imaging results using a human chest phantom equipped with fresh porcine lungs at radiation dose below clinically CT.

Methods:

We used the ARTIChest phantom (PRO Design, Germany) equipped with fresh porcine lungs. PBI was performed at the Italian synchrotron using the XCounter (Direct Conversion, Sweden) detector with a pixel size of 100 μ m, a sample-to-detector distance of 10.7m and a monochromatic x-ray beam at 40keV, resulting in an effective pixel size of 67 μ m. Clinical CT was performed at the Cattinara Hospital Trieste using an iCT 256 (Philips, Germany) with a resolution of 0.45x0.45x0.9mm. PBI and iCT images were acquired with 10 and 13mGy respectively, measured with thermoluminescence dosimeters embedded in the phantom.

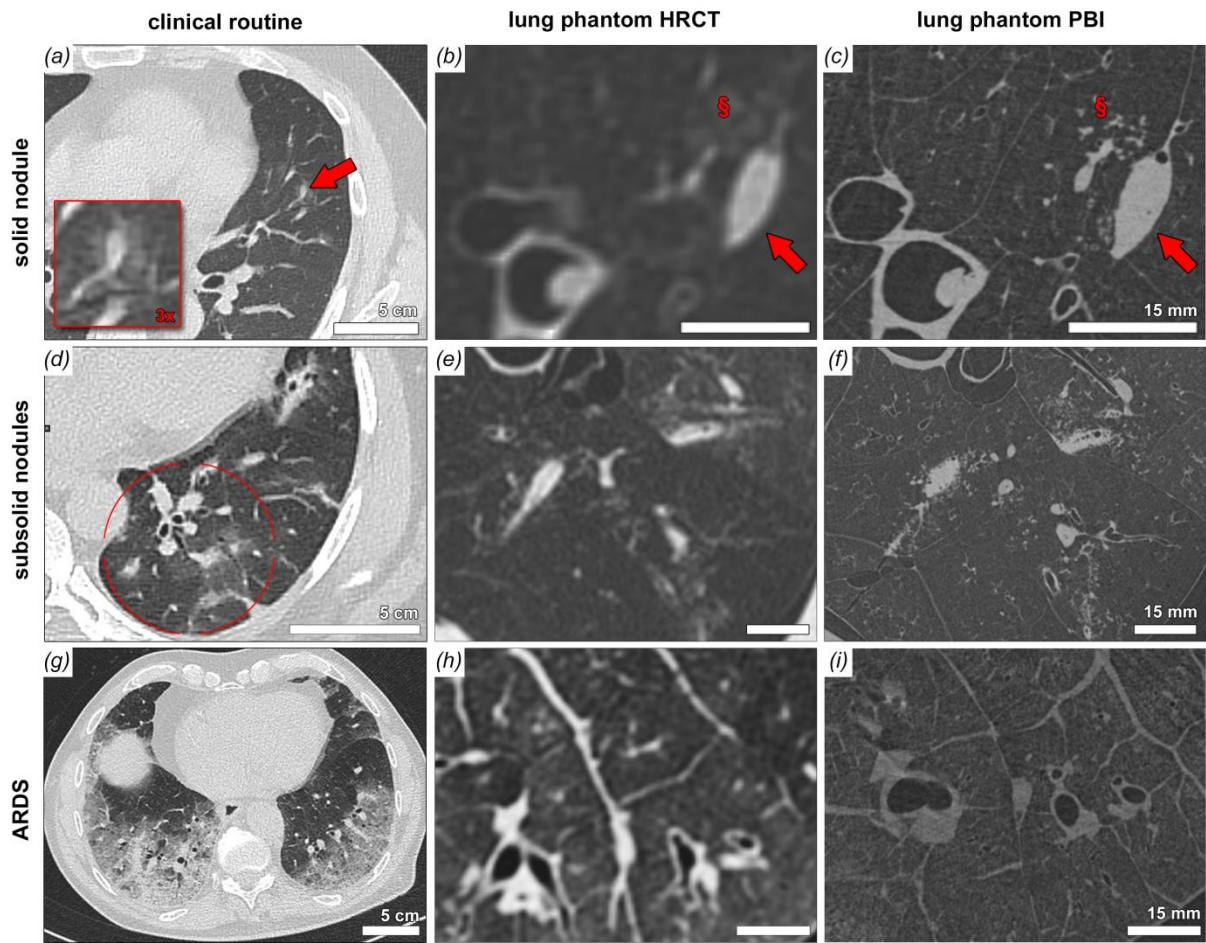
Results:

Figure 1 a), d) and g) show clinical CT data sets with a solid tumor nodule (red arrow), a region with subsolid nodules (red circle) and acute respiratory distress syndrome (ARDS). Figure 1 b), e) and h) depicts three different pig lungs in ARTIChest and scanned with clinical HRCT. In Figure 1 b) and e) an iodine agarose mix was injected to mimic lung nodules. Figure 1 h) shows a lung from an ARDS pig model. In comparison with Figure 1 a), d) and g) it can be seen that those artificial structures resemble clinical features. Figure 1 c), f) and i) shows the PBI results for the same lungs. Clearly higher spatial resolution allows a better diagnosis of pathologies. For instance “ground glass opacity” in Figure 1b) indicated by (§) can now be resolved as agarose filled alveoli.

Discussion:

We present PBI results for scanning a human chest phantom with porcine lungs and artificially induced lung pathologies. Scans were achieved with 10mGy at an effective pixel size of 67 μ m and therefore at only 0.2% of the voxel volume of the clinical HRCT using 13mGy. Currently the PBI acquisition takes 3mins due to limitations of the rotary unit. We are confident that acquisition can be realized in less than 10s in the future and therefore will allow breath-hold acquisitions in patients. The development of a lung imaging beamline for patients at the Italian synchrotron is foreseen and we hope that with this we can spare

patients transthoracic biopsies by providing images detailed enough for *in-vivo virtual biopsy* analysis.



Abstract No. 901



Value of functional lung MRI in long term patient care after lung transplantation

Till Kaireit^{1, 2, *}, *Jens Vogel-Claussen*^{1, 2}, *Andreas Voskrebenzev*^{1, 2}, *Filip Klimeš*^{1, 2}, *Lea Behrendt*^{1, 2}, *Marcel Gutberlet*^{1, 2}, *Christopher Korz*^{1, 2}, *Milan Speth*^{1, 2}, *Tobias Welte*^{1, 2}, and *Jens Gottlieb*^{1, 2}

¹Hannover Medical School, Hannover

²Biomedical Research in Endstage and Obstructive Lung Disease (BREATH), German Center for Lung Research

*Presenting author

Aim

To evaluate the prognostic utility of phase resolved functional lung (PREFUL)-MRI in predicting chronic lung allograft dysfunction (CLAD) related transplant loss or death in a prospective longitudinal single center study.

Methods

PREFUL MRI-derived regional flow-volume loop derived ventilated volume (RFVL-VV) of double lung transplant recipients were assessed 6-12 months (baseline) and 2.5 years post transplantation (follow-up). Spirometry was carried out at the same day. Clinical and MRI parameters were compared in regard to CLAD related graft loss (re-do transplant or death) as primary endpoint using ROC, Kaplan-Meier survival analysis and Cox proportional hazards model.

Results

At baseline MRI, 132 clinically stable patients were included, of which 24 patients had CLAD related graft loss. RFVL-VV [%] predicted poorer survival (cutoff=92.3, Log-Rank $P=.02$, hazard ratio for graft loss, 2.53; 95%CI 1.13 to 5.67, $P=.02$), while spirometry showed no significantly different survival ($P>.05$).

Evaluating the follow-up MRI (75 stable vs 19 CLAD related graft loss), %change of RFVLVV predicted poorer survival of patients (cutoff=97.1, Log-Rank $P<.0001$; hazard ratio for graft loss, 7.69, 95%CI 2.33 to 25.31) as well as %change of FEV1 (cutoff=60.8, Log-Rank $P=.0002$; hazard ratio for graft loss, 7.94; 95%CI 2.31 to 27.36, $P=.001$). A combined score of PREFUL-MRI with FEV1 showed a stronger prediction of graft loss than either parameter alone (cutoff=4357.1 [%Baseline * %Baseline]; Log-Rank $P<.0001$; hazard ratio for graft loss, 13.82; 95%CI 4.10 to 46.80, $P<.0001$).

Conclusion

PREFUL-MRI predicts CLAD related death or transplant loss in a large prospective post lung transplant cohort and may add clinical value in monitoring patients post lung transplantation.

Abstract No. 902



Hyperpolarized ^{129}Xe MRI of healthy subjects reveals age-related changes in gas

David Mummy^{1,*}, Aparna Swaminathan¹, Junlan Lu¹, Suphachart Leewiwatwong¹, Doreen Dai¹, Shuo Zhang¹, Jennifer Korzekwinski¹, and Bastiaan Driehuys¹

¹Duke University

*Presenting author

RATIONALE: A range of metrics derived from hyperpolarized ^{129}Xe gas exchange MRI and spectroscopy have been proposed as potential markers of disease progression and therapy response in diverse diseases such as asthma, COPD, interstitial lung disease, and radiation-induced lung injury. However, age-related changes in these measurements in healthy subjects are poorly understood. Characterizing these changes is necessary for differentiating between disease-driven abnormalities and the expected consequences of aging. To this end, we assess a set of commonly used ^{129}Xe imaging and spectroscopy measurements in a population of healthy subjects with a wide range of ages.

METHODS: Subjects (N=45, 16F/29M, age 43.5 ± 17.9 yrs, min-max 19-87 yrs) with no history of pulmonary disease and less than 5 pack-years smoking history and no smoking history within the last 5 years underwent hyperpolarized ^{129}Xe MRI. Quantitative imaging provided three-dimensional maps of ventilation, interstitial membrane uptake, and red blood cell (RBC) transfer; functional image voxels were binned according to thresholds derived from a young healthy reference cohort previously described. ^{129}Xe spectroscopy provided static and dynamic parameters, most prominently the RBC:membrane ratio (RBC:M) and also RBC chemical shift and cardiogenically-driven RBC amplitude oscillations. Subjects were stratified into 3 age groups (<30 yrs, 30-49 yrs, and 50+ yrs) and image-based metrics were compared across these age categories using the Wilcoxon rank-sum test with the Holm-Bonferroni correction for multiple comparisons. Spectroscopic parameters were assessed individually using multivariate linear models, with age, sex, and body mass index (BMI) as predictors.

RESULTS: Fifteen subjects (33.3%) were in the <30 yr category at imaging; 11 subjects (24.4%) were 30-49 yrs; and 19 subjects (42.2%) were 50+ yrs. As shown in Figure 1, RBC defect percent was significantly higher in the 50+ yr group vs. both the <30 yr group and the 30-50 yr group ($p=0.05$ and $p=0.04$, respectively). There were no differences in ventilation or membrane measurements across the three age groups, although ventilation defect percent showed a general trend towards increasing with age.

On spectroscopy, RBC:M was inversely correlated with age (Pearson's $r=-0.52$, $p<0.001$, see Figure 2). In a multivariate linear model with RBC:M as the outcome, age, sex, and BMI were all significant predictors ($p<0.001$, $p<0.001$, and $p<0.05$ respectively). In this model, each additional 10 years of age was associated with a 0.04 loss in RBC:M, each additional 10 points of BMI was associated with an RBC:M decrease of 0.06, and male sex was associated with an RBC:M increase of 0.15. In an analogous multivariate model of RBC oscillations, only age was significant, with each additional 10 years of age associated with a 0.6 percentage point increase in oscillations ($p<0.01$). In the model of RBC chemical shift, none of the three predictors were significant.

CONCLUSIONS: These results suggest that increased RBC transfer defects, decreased RBC:M, and increased RBC amplitude oscillations may be a common finding in older healthy patients with no diagnosed pulmonary abnormalities. By contrast, the membrane defect percent, high membrane percent, and RBC chemical shift were stable across age groups, suggesting that deviations in these metrics may be a marker of an underlying disease process.

Wang, Ziyi, et al. "Quantitative analysis of hyperpolarized ^{129}Xe gas transfer MRI." *Medical physics* 44.6 (2017): 2415-2428

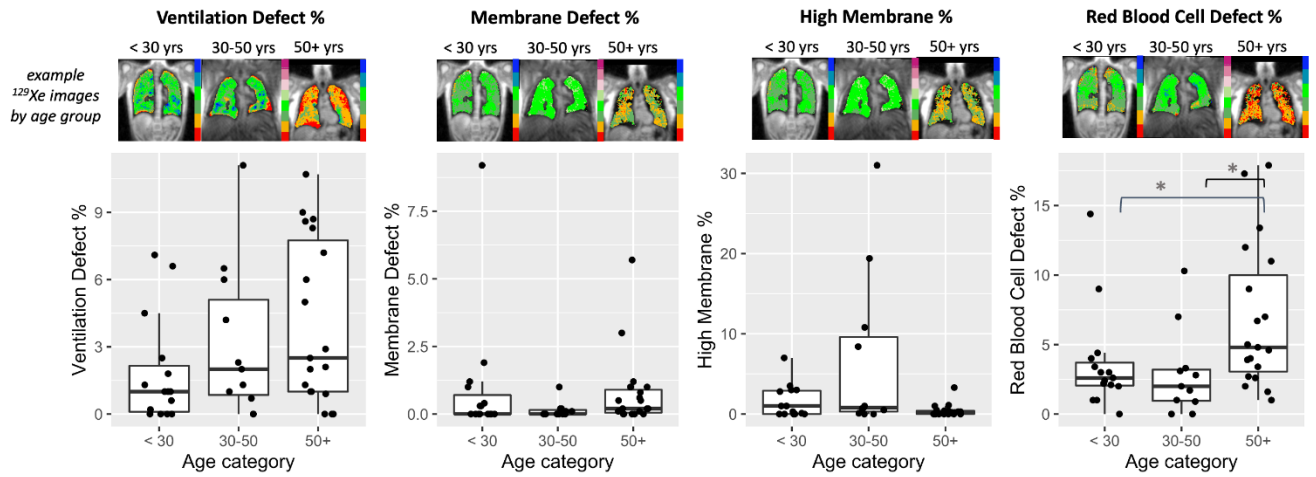
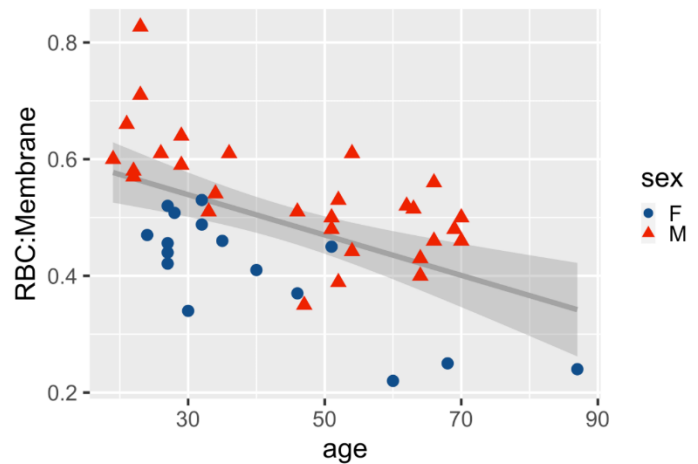


FIGURE 1. From L-R: ventilation defect percent, membrane defect percent, high membrane percent, and red blood cell defect percent in healthy subjects (N=45) in three age categories. Ventilation defect percent (far left) showed an increased trend with age but the difference was not significant. Red blood cell defect % (far right) was significantly increased in the 50+ group vs. the other two groups. There were no significant differences in membrane across age groups. * $p < 0.05$.

FIGURE 2 (right). RBC:M is inversely correlated with age (Pearson's $r = -0.52$, $p < 0.001$). In a multivariate linear regression model, age, sex, and BMI were all significant predictors of RBC:M ($p < 0.001$, $p < 0.001$, and $p < 0.05$ respectively). Each additional 10 years of age was associated with a 0.04 loss in RBC:M, each additional 10 points of BMI was associated with an RBC:M decrease of 0.06, and male sex was associated with an RBC:M increase of 0.15.



Abstract No. 903

MRI Detects Improvements of Pulmonary and Paranasal Sinus Abnormalities in Response under CFTRm

Lena Wucherpfennig^{1,2,*}, Simon M. F. Triphan^{3,2}, Sabine Wege^{4,2}, Hans-Ulrich Kauczors^{5,2}, Claus Peter Heußel^{4,6}, Niclas Schmitt³, Felix Wünnemann^{3,7}, Victoria L. Mayer³, Olaf Sommerburg^{5,2}, Marcus A. Mall^{8,2}, Monika Eichinger^{4,2}, and Mark O. Wielpütz^{5,2}

¹Diagnostic and Interventional Radiology

²German Center for Lung Research (DZL)

³University Hospital Heidelberg

⁴Thoraxklinik at University Hospital Heidelberg

⁵University of Heidelberg

⁶German Center for Lung Research (DZL), Translational Lung Research Center (TLRC)

⁷Helios Dr. Horst Schmidt Kliniken Wiesbaden

⁸Charité - Universitätsmedizin Berlin

*Presenting author

Background:

Therapy with Elexacaftor/Tezacaftor/Ivacaftor (ETI) was recently approved for adult cystic fibrosis (CF) patients with at least one F508del mutation. However, its effects on structural and functional lung abnormalities and chronic rhinosinusitis have not been studied by imaging.

Methods:

19 adults with CF (mean age 31±9y, range 19-55y) underwent standardized chest magnetic resonance imaging (MRI), and nine also same-session sinonasal MRI, before (MRI1) and after (MRI2) at least one month (mean duration 5±3mon) on ETI. 24 control CF patients (30±7y, range 20-44y) without ETI underwent longitudinal chest MRI, and eleven also sinonasal MRI, twice (mean interval 40±15mon). MRI was assessed using the validated chest MRI score and chronic rhinosinusitis (CRS)-MRI score. Forced expiratory volume in 1s percent predicted (FEV1%) was measured in all patients.

Results:

In controls, the chest MRI global score and CRS-MRI sum score were stable from MRI1 to MRI2. In patients under ETI, the chest MRI global score improved (-11.4±4.6, P<0.001), mainly due to reduction of bronchiectasis/wall thickening and mucus plugging subscores (-3.3±2.2 and -5.2±1.5, P<0.001, respectively). The improvement in chest MRI score correlated well with improved FEV1% (r=-0.703, P<0.001). The CRS-MRI sum score also improved in patients under ETI (-6.9±3.0, P<0.001), mainly due to a reduction of mucopyoceles in the maxillary and ethmoid sinus (-50% and -39%, P<0.05, respectively).

Conclusions:

MRI detects improvements of chest MRI and CRS-MRI scores in adult CF patients who first received ETI, demonstrating reversibility of structural lung and paranasal sinus abnormalities in patients with established disease.

We thank the following companies for their valuable support of the conference

Gold Sponsors

core:line
EUROPE



SIEMENS
Healthineers

Silver Sponsors

AstraZeneca 



Medtronic

Bronze Sponsors


aidence
human sense in artificial intelligence

PHILIPS

POLAREAN
BREATH TAKING IMAGES

 **MSD**